

Dynamics and Composition of Collapsar Disk Outflows

by

Coleman Dean

A thesis submitted in partial fulfillment of the requirements for the degree of

Doctor of Philosophy

Department of Physics
University of Alberta

© Coleman Dean, 2024

Abstract

We investigate mass ejection from accretion disks formed during the collapse of rapidly-rotating Wolf-Rayet stars, also known as *collapsars*. The neutrino-cooled, black hole (BH) accretion disk that forms at the center of the star — and the ensuing outflows — provides the conditions for these systems to be candidate r -process element production sites and potential progenitors of broad-lined Type Ic (Ic-BL) supernovae. Here we present global, long-term axisymmetric hydrodynamic simulations of collapsar disks that include angular momentum transport through shear viscosity, neutrino emission and absorption, a 19-isotope nuclear reaction network and nuclear statistical equilibrium solver, a pseudo-Newtonian BH with mass and spin modified by accreted matter, and self-gravity. Starting from a stellar profile collapsed in spherical symmetry, our models capture disk formation self-consistently, and are evolved until after the shock wave — driven by disk winds — reaches the surface of the star. None of our models achieve sufficient neutronization to eject significant amounts of r -process elements. Sufficient ^{56}Ni is produced to power a typical type Ic-BL supernova light curve, but the average asymptotic velocity is a factor $\sim 2 - 3$ times too slow to account for the typical line widths in type Ic-BL supernova spectra. The gap in neutrino emission between BH formation and shocked disk formation, and the magnitude of the subsequent peak in emission, would be observable diagnostics of the internal conditions of the progenitor in a galactic collapsar. Periodic oscillations of the shocked disk prior to its expansion are also a potential observable through their impact on the the neutrino and gravitational wave signals.

We also analyze passive tracer particles included in our simulations, used for post-

processing with a larger nuclear reaction network, and we evolve models in which we modify the rotation profile of the progenitor star to maximize neutrino reprocessing of circularized mass shells. All of our models produce several M_{\odot} of oxygen, followed by about a solar mass of carbon, neon, and nickel, with other alpha elements produced in smaller quantities. Only one of our models, with the lowest strength of viscous angular momentum transport, yields significant amounts of first r -process peak elements, with negligible yields at higher nuclear masses. The rest of the set produces very small or negligible quantities of elements beyond the iron group. Models that produce the heaviest elements (up to $A \sim 200$) do so along the proton-rich side of the valley of stability at high entropy ($s/k_B \sim 80$), pointing to the rapid proton capture process (rp -process) as a mechanism that operates in collapsars. The absence of neutron-rich ejecta proves to be insensitive to changes in the rotation profile of the star, suggesting that heavy r -process elements are difficult to produce in collapsars if no large-scale poloidal magnetic field is present in the disk to drive outflows during neutronization.

Preface

This thesis contains research completed by myself based on a simulation framework developed initially by Rodrigo Fernández. The work I completed includes modification of the simulation framework, bug fixing, running of the simulation, as well as post-processing of data from the simulation. Text from chapters 1, 4, and 5 was written by myself, with comments from Rodrigo Fernández. Chapter 1 includes a reproduction of Figure 1 of Burbidge et al. (1957) via license number RNP/24/JUL/081087. There was no use of generative Artificial Intelligence in the development of this thesis.

Chapter 2 includes the first published paper based on this research, with abstract stripped:

Dean, C. & Fernández, R. (2024). Collapsar disk outflows: Viscous hydrodynamic evolution in axisymmetry. *Physical Review D*, vol. 109, no. 8, APS.

doi:10.1103/PhysRevD.109.083010.

© 2024 American Physical Society

The first draft of the paper was written by myself, with edits by Rodrigo Fernández. Tables and figures were made by myself, with suggestions for changes made by Rodrigo Fernández.

Chapter 3 includes the second published paper based on this research, with abstract stripped:

Dean, C. & Fernández, R. (2024). Collapsar disk outflows: Heavy element production. *Physical Review D*, in press, arxiv:2408.15338

© 2024 American Physical Society

The first draft of the paper was written by myself, with edits by Rodrigo Fernández.

Tables and figures were made by myself, with suggestions for changes made by Rodrigo Fernández.

“Neither of us can afford to worry about relativity right now”

- “J. Cooper”, Interstellar

Acknowledgements

I would like to thank Rodrigo Fernández for his guidance and mentorship in conducting this research. I would like to thank Steven Fahlman, and Suhasini Rao for helpful discussions.

This research was supported by the Natural Sciences and Engineering Research Council of Canada (NSERC) through Discovery Grant RGPIN-2022-03463. Support was also provided by the Alberta Graduate Excellence Scholarship. Some of the software used in this work (**FLASH**) was in part developed by the U.S Department of Energy (DOE) NNSA-ASC OASCR Flash Center at the University of Chicago. Data visualization was done in part using **VisIt** (Childs et al., 2012), which is supported by DOE with funding from the Advanced Simulation and Computing Program and the Scientific Discovery through Advanced Computing Program. This research was enabled in part by computing and storage support provided by Prairies DRI, BC DRI Group, Compute Ontario (computeontario.ca), Calcul Québec (www.calculquebec.ca) and the Digital Research Alliance of Canada (alliancecan.ca). Computations were performed on the Niagara supercomputer at the SciNet HPC Consortium. SciNet is funded by Innovation, Science and Economic Development Canada; the Digital Research Alliance of Canada; the Ontario Research Fund: Research Excellence; and the University of Toronto (Ponce et al., 2019; Loken et al., 2010). Data visualization was done in part using **matplotlib** (Hunter, 2007).

Table of Contents

1	Introduction	1
1.1	Motivation	1
1.2	Nucleosynthesis in Collapsars	6
1.3	Thesis Objectives	8
1.4	Overall Approach	8
1.5	Thesis Outline	15
2	Collapsar disk outflows I: Viscous hydrodynamic evolution in axisymmetry	16
2.1	Introduction	16
2.2	Methods	19
2.2.1	Progenitors and Evolution to BH Formation	19
2.2.2	Evolution after BH formation	23
2.2.3	Models evolved	31
2.2.4	Outflow and shock analysis	31
2.3	Results	32
2.3.1	Overview of disk formation and evolution	32
2.3.2	Outflow properties	42
2.3.3	Dependence of Disk Evolution on EOS and Progenitor Model	45
2.3.4	Neutrino emission and neutronization	49
2.3.5	An engine for type Ic-BL supernovae?	50
2.3.6	Comparison to recent work	52
2.4	Summary and Discussion	55
2.5	Nuclear Burning and Equation of State	60
2.5.1	Internal Energy Update	60
2.5.2	Nuclear Statistical Equilibrium (NSE)	61
2.6	Variable Floors	62
2.6.1	Density, pressure and internal energy floors	62
2.6.2	Temperature floor	63

3	Collapsar disk outflows II: Heavy element production	65
3.1	Introduction	65
3.2	Methods	68
3.2.1	Summary of Computational Approach	69
3.2.2	Nucleosynthesis in Post-Processing	71
3.2.3	Modified Progenitor Rotation Profile	74
3.2.4	Models Evolved	76
3.3	Results	77
3.3.1	Summary of Models from Paper I	77
3.3.2	Models with Modified Angular Momentum Profile	79
3.3.3	Analysis of the 19-Isotope Network Output	88
3.3.4	Nucleosynthesis in Post-Processing	93
3.3.5	Optimal Initial Tracer Particle Placement	104
3.3.6	Comparison to previous work	105
3.4	Summary and Discussion	108
4	Additional Code development	113
4.1	Dynamic Computational Domain Boundaries	113
4.2	Numerical Stability of Neutrino Opacities	116
4.3	Robustness of Non-linear Root Finding For NSE Solver	119
4.4	Spatially-varying floors of thermodynamic quantities	121
4.4.1	Density, Pressure, and Specific Internal Energy Floors	122
4.4.2	Temperature Floor	126
4.5	Shock Tracking	129
4.6	Post-shock Heating	134
5	Conclusions and Future Work	136
5.1	Conclusions	136
5.2	Future Work	141
	Bibliography	142

List of Tables

2.1	List of evolved models, parameters used, and key simulation timescales. Columns from left to right show the model name, progenitor star from Woosley & Heger (2006), EOS used in GR1D evolution to BH formation, and viscosity parameter used in the 2D post-BH evolution. Subsequent columns show times relative to the bounce time in GR1D: BH formation time in GR1D, shocked disk formation time, mass of the BH at disk formation, shock breakout time (leading edge reaching the surface of the star), and the maximum simulation time.	26
2.2	Bulk outflow properties, obtained by integrating unbound material at the end of the simulation. Columns from left to right show model name, ejecta mass, ejecta kinetic energy at the end of the simulation, asymptotic ejecta kinetic energy (Equation 2.22), mass-weighted average expansion velocity at infinity (Equations 2.21, 2.23), minimum electron fraction of outflowing material, ^{56}Ni mass ejected, and SN light curve peak time (Equation 2.24, (Arnett, 1982)).	40
3.1	List of models studied in this paper, and key quantities. The first five models were introduced in Paper I, and the last three (16TI_SFHo- $k_{\text{rad}}6$, 16TI_SFHo- $k_{\text{rad}}10$, and 350C_SFHo- $k_{\text{rad}}10$) are new. Columns from left to right show the model name, progenitor star from Woosley & Heger (2006), EOS used in GR1D evolution to BH formation, viscosity parameter used in the 2D post-BH evolution in FLASH, and angular momentum profile factor k_{rad} (Equation 3.3). Subsequent columns show times relative to core bounce time in GR1D (BH formation time in GR1D t_{bh} , shocked disk formation time in FLASH t_{df} , shock breakout time t_{sb} , and the maximum simulation time t_{max}), and BH masses at various points in time (BH mass at disk formation, BH mass at the transition to the ADAF phase [Sec. 3.3.1], and final BH mass). . . .	75

3.2	Bulk outflow properties, obtained by integrating unbound material at the end of the simulation, in models with modified angular momentum profile and their corresponding base models (c.f. Table 3.1). Columns from left to right show model name, ejecta mass, ejecta kinetic energy at the end of the simulation, asymptotic ejecta kinetic energy, mass-weighted average expansion velocity at infinity (Eq. 3.5), and minimum electron fraction of outflowing material (c.f. Fig. 3.4).	82
3.3	Ejecta masses and mass-weighted average asymptotic velocities of selected isotopes from the 19-isotope nuclear network, for all models. Ejecta masses are given in units of M_{\odot} , and asymptotic velocities in units of 10^3 km s^{-1} . ^1H ejecta mass and asymptotic velocity include a combination of p^+ and ^1H from the nuclear network.	95
3.4	Continuation of Table 3.3.	96
3.5	Continuation of Table 3.3-3.4	97
3.6	Continuation of Table 3.3-3.5	98
3.7	Summary of tracer particle sampling of the ejecta. Columns from left to right show the number of unbound particles at the end of the simulation with $T_{\text{max}} > 1 \text{ GK}$ (all models are initialized with 10^4 particles), total mass in unbound particles at the end of the simulation, total ejecta mass integrated from the grid, ratio of the mass in unbound particles to total ejecta mass (sampling percentage), mass-weighted average asymptotic velocity obtained from the particles and from the grid, mass-weighted average electron fraction from the particles and from the grid, and mass-weighted average entropy per baryon from the particles and grid, respectively.	99

List of Figures

1.1	Figure 1 of Burbidge et al. (1957) reproduced via licence number RNP/24/JUL/081087. Schematic curve of atomic abundances as a function of atomic weight based on the data of Suess & Urey (1956).	3
2.1	Characteristic radii as a function of enclosed gravitational mass at the last snapshot before BH formation in GR1D (Section 2.2.1) for the pre-supernova progenitors 16TI (SFHo EOS left, DD2 EOS center) and 350C (SFHo EOS right), evolved in all cases with approximate rotation effects. Curves show the radial coordinate (purple), ISCO radius (light blue), event horizon radius (green), and circularization radii obtained with a Newtonian potential (dashed burgundy, eq. 2.2) and with the Artemova pseudo-Newtonian potential (solid burgundy, defined by Equation 2.5). All quantities account for the spinup of the BH with the enclosed angular momentum at each mass (eq. 2.1). The gray shaded area shows the region excised initially from the computational domain for subsequent evolution in 2D with FLASH (Section 2.2.2). The black circle marks the predicted BH mass at disk formation, and the vertical dashed black line shows the actual BH mass when the shocked accretion disk forms in the FLASH simulation.	20
2.2	Transition from <i>dwarf disk</i> to thermalized disk in model 16TI.SFHo, with time after core bounce in the preceding GR1D evolution labeled at the top of each panel. <i>Left:</i> The shocked interface (dwarf disk) between supersonic inflows along the equator near the central BH. <i>Center:</i> Pileup of material and onset of the shock near the BH. <i>Right:</i> Thermalized disk surrounded by a shock. The black circle at the origin is the excised inner radial boundary of the domain.	30

2.3	Snapshot of the density distribution for model 16TI_SFHo at ~ 13.1 s post bounce. At this point in the simulation the shocked disk has formed (11.1 s post bounce, Figure 2.2), and a dominance of viscous heating drives turbulence and a disk wind which, combined with the increasing specific angular momentum of accreted material, propels the shock out through the star. A slight north-south asymmetry and large-scale corrugation due to oscillations (Figure 2.6) are already visible. These deviations from sphericity become more apparent as oscillations freeze out and the shock propagates through the star.	34
2.4	<i>Top:</i> Mass accretion rate across the inner radial boundary as a function of post-bounce time for selected models, as labelled. <i>Middle:</i> Mass outflow rate with positive Bernoulli parameter across an extraction radius $r_{\text{ej}} = 10^9$ cm, for the same set of models as the top panel. <i>Bottom:</i> Total viscous heating, nuclear heating, and net neutrino cooling rates inside the shock radius in model 16TI_SFHo, as labeled. The <i>19 isotope nuclear</i> curve shows the heating rate from the nuclear reaction network. Each curve has been smoothed with a moving average of width 0.5 s. The vertical dashed line shows the time of shocked disk formation.	35
2.5	Evolution of the average shock radius (a_0) as a function of time after disk formation (Table 2.1), for all models, until shock breakout from the stellar surface.	36
2.6	Evolution of the normalized dipole (top) and quadrupole (bottom) Legendre coefficients of the shock radius (Equation 2.20), for selected models. In most cases, the shock undergoes an initial oscillation phase before the geometry freezes, and continues to expand with little oscillation afterward. Each panel includes an inset which enlarges the time axis around the initial oscillation phase.	36
2.7	Frequency analysis of initial shock oscillations. Data extends from the time of disk formation until the spherical harmonic coefficient begins to asymptote and the shock shape freezes. Left and right columns show data from different models, as labeled. <i>Top:</i> Evolution of the Legendre coefficient a_1 normalized by the average shock radius a_0 . <i>Middle:</i> Amplitude (absolute value) of the Fourier transform $\mathcal{F}(a_1/a_0)$ of the normalized $\ell = 1$ time series. <i>Bottom:</i> Characteristic frequencies $f_i = v_i/a_0$ calculated using the average sound speed ($v_i = c_s$), poloidal speed ($v_i = v_p$), and radial speed from behind the shock front ($v_i = v_r$), as labeled.	38

2.8	Mass histograms of the outflow at the end of the simulation for model 16TI_SFHo, binned by poloidal velocity (left), electron fraction (center), and entropy per baryon (right). Different colours represent the gravitational binding criterion used, as labeled (<i>Total</i> represents both bound and unbound matter).	41
2.9	Unbound mass histograms at various post-bounce times in each simulation, as labeled. Only material with positive Bernoulli parameter (Equation 2.17) and $v_r > 0$ is considered. Columns from left to right show histograms binned by poloidal velocity (left), electron fraction (center), and entropy per baryon (right).	43
2.10	Neutrino luminosities of ν_e [blue], $\bar{\nu}_e$ [teal], and ν_x [all heavy lepton species, green] as a function of post bounce time for selected models, as labeled. The vertical lines indicate the time of BH formation t_{bh} (solid black), shocked disk formation t_{df} (dashed black), and shock breakout from the star t_{sb} (dotted black). The shaded grey and white regions correspond to the GR1D and FLASH portion of the evolution, respectively.	44
2.11	Snapshots of the electron fraction within the inner disk in model 16TI_SFHo around the time of maximum neutrino emission (c.f. Fig. 2.10), with overlaid density contours, as labeled.	48
3.1	Snapshots of the density in model 16TI_SFHo at three points in the simulation, as labelled, corresponding to initial particle placement (left), shortly after the start of rapid shock expansion (middle), and end of the simulation (right). Tracer particle positions are overlaid, with white dots corresponding to particles that end up accreted onto the BH, and ejected particles marked in black. The number of particles remaining in the computational domain is listed in each panel, including the small number that never exceed 1 GK and are discarded from the analysis. The black region visible in the third panel marks the outermost edge of the spherical grid.	70

- 3.2 Characteristic radial distances as a function of enclosed gravitational mass for stellar progenitors 16TI and 350C from Woosley & Heger (2006) at the last snapshot in GR1D prior to BH formation. The radial coordinate is $r(m)$ (black solid), with the the PNS surface corresponding to the vertical segment at $M \simeq 2M_{\odot}$. Colored lines without label show circularization radii obtained with the pseudo-Newtonian potential employed by the code (solid) and a Newtonian potential with the same enclosed mass (dashed, c.f. Eq. 3.2), with colors corresponding to different models, as labeled above. Models 16TI_SFHo and 350C_SFHo were presented in Paper I, while remaining models have the modified rotation profile discussed in Section 3.2.3 (Equation 3.3), with the value of $k_{\text{rad}} = \{6, 10\}$ indicated in the model name. Finally, each panel shows the event horizon radius r_{h} and radius of the innermost stable circular orbit r_{isco} for a BH with the same enclosed mass and angular momentum as in the progenitor with unmodified $j(M)$. The gray shaded region is excised from the computational domain when mapping to FLASH. The BH mass when disk formation is predicted to occur is marked with a circle, while the BH mass at actual disk formation in each simulation is marked with a thin vertical dashed line. 73
- 3.3 Evolution of models with modified angular momentum profile and the unmodified control set, as labelled (c.f. Table 3.1). *Top*: Evolution of the average shock radius as a function of post-disk formation time. The vertical dotted lines in each panel represent the transition from the NDAF to ADAF phase, as defined by Eq. (3.4). *Second from top*: Mass accretion rate \dot{M}_{in} across the inner radial boundary, and mass outflow rate \dot{M}_{out} across a spherical surface at $R_{\text{ej}} = 10^9$ cm as a function of time after disk formation. *Third from top*: Absolute value of viscous heating, net neutrino cooling, and nuclear energy injection as function of post-disk formation time. *Bottom*: Ratio of postshock-integrated net neutrino cooling to viscous heating as a function of post-disk formation time, capped at unity. The early NDAF phase (Eq. 3.4) is shaded, while the later ADAF phase extends beyond the vertical dotted line. Curves in Rows 2 and 3 are smoothed with a moving average of width 0.5 s, for visibility. 78

3.4	Minimum electron fraction in the simulation domain as a function of time, for different models, as labelled. Disk formation times are marked with a dashed line, and the transition from NDAF to ADAF phase (Eq. 3.4) is marked with a dotted line. The shaded region shows $Y_e < 0.25$, which is an approximate measure of the value below which lanthanides can be produced (e.g., Lippuner & Roberts (2015)). . . .	79
3.5	Unbound mass histograms at the end of the simulation, for models with modified rotation profile and their corresponding unmodified counterparts, as labelled (c.f. Table 3.1). Only matter with positive Bernoulli parameter and $v_r > 0$ is considered. Histograms are binned by poloidal velocity $v_p = (v_r^2 + v_\theta^2)^{1/2}$ (left), electron fraction Y_e (center), and entropy per baryon s/k_B (right).	81
3.6	Angle-averaged mass fractions in unbound material of selected isotopes from the 19-isotope network, as a function of angle-averaged enclosed mass, for models 16TI_SFHo (left) and 350C_SFHo (right). The black dashed line shows the angle-averaged radial velocity of the ejecta as a function of enclosed mass (right y-axis). The mass fraction of ^1H represents a combination of p^+ and ^1H	84
3.7	Unbound mass histograms of selected isotopes from the 19-isotope network, binned by asymptotic velocity (Equation 3.5) for models 16TI_SFHo (left) and 350C_SFHo (right). The ^1H ejecta mass represents a combination of the p^+ and ^1H ejecta masses.	85
3.8	Mass fractions of ^{16}O , ^{44}Ti , and ^{56}Ni at the last simulated time in model 16TI_SFHo, with density contours overlaid. Data is not shown when the atmospheric mass fraction $X_{\text{atm}} > 0.01$ (as in, e.g., the white patch in the northern hemisphere of the rightmost panel). The outer domain edge is marked with a dashed line in the right panel, with the middle and left panels representing subsequent zoom-ins towards the inner radial edge of the domain.	86
3.9	Evolution of the unbound mass in ^{44}Ti (top) and ^{56}Ni (middle), as well as their ratio $M_{44\text{Ti}}/M_{56\text{Ni}}$ (bottom), for all of our models. Also shown is the solar mass ratio of $^{44}\text{Ca}/^{56}\text{Fe}$ (dashed line), corresponding to the endpoints of the ^{44}Ti and ^{56}Ni decay chains, respectively, for reference. The bottom panel shows data for $t - t_{\text{bounce}} > 16$ s, to improve visibility.	91

3.10	Unbound mass histograms binned by poloidal velocity (left), electron fraction (middle), and entropy per baryon (right), for selected models. Light colors show results calculated by integrating unbound matter over the grid at the end of the simulation, and dark colors show values obtained from unbound tracer particles which reach $T_{\max} > 1$ GK, remaining in the domain at the end of the simulation, illustrating the level of sampling of the ejecta by the particles.	92
3.11	Isotopic abundances at 30 years from tracer particles evolved with SkyNet , for all models, as labelled. Abundances are obtained by dividing the isotopic mass fraction $X(A)$ by the mass number A , with the mass fractions adding up to unity. Open circles show the solar r -process abundance distribution from Goriely (1999), scaled to the first r -process peak ($A = 82$) from model 16TI.SFHo_α001, for reference.	94
3.12	Average abundance $\langle Y \rangle$ of isotopes on the (N, Z) -plane, 30 years post-bounce, as evolved in SkyNet for model 350C.SFHo_ $k_{\text{rad}}10$. The final abundance of each simulation is an average over the particle abundances, weighted by the number of baryons. Isotopes evolved in SkyNet are marked with grey boxes, stable isotopes (IAE, 2023) are marked with black squares. Closed proton shells (corresponding to magic numbers 2, 8, 20, 28, 50, 82, and 126) are marked with horizontal black lines, and closed neutron shells are marked with vertical black lines. The diagonal black line marks equal number of protons and neutrons in an isotope.	102
3.13	Time evolution of abundances on the (N, Z) -plane for the particle that produces the heaviest isotopes in model 16TI.DD2 (Fig. 3.11). The temperature, electron fraction (from SkyNet) and entropy per baryon of the tracer particle at each time are shown in each panel.	103
4.1	Snapshots of the density at the inner radial boundary (top row) and outer radial boundary (bottom row) before a domain shift (left column) and after the domain restart (right column) for the 350C.SFHo model. Every second radial and angular bin edge is marked with a black line to facilitate visibility near the inner radial edge. Twelve radial cells are removed from the inner edge by this domain restart, adding twelve radial cells to the outside domain thus keeping the total number of radial cells constant.	115

4.2	Fermi integral approximations for $\mathcal{F}_1, \mathcal{F}_2, \mathcal{F}_3, \mathcal{F}_4, \mathcal{F}_5$, and $\mathcal{F}_5/\mathcal{F}_4$ as labelled. Curves are included showing inclusion of up to the first term, second term, third term, and fourth term in the approximation from equation 4.9, and fractional difference between the full approximation and inclusion of only the leading order term. The grey shaded region shows the limit where this approximation is used.	118
4.3	Schematic view of the NSE test performed in the NR solver in the case that the initial temperature guess $T_i > T_{\text{NSE}}$, but the solution $T_{\text{solution}} < T_{\text{NSE}}$	121
4.4	Schematic view of the NSE test performed in the NR solver in the case that the initial temperature guess $T_i > T_{\text{NSE}}$, and at some point the NR solver overshoots to a value $T_{i+1} < T_{\text{NSE}}$ despite the solution $T_{\text{solution}} > T_{\text{NSE}}$	121
4.5	Evolution of radial rays along the equator of density (top left), temperature (top right), pressure (bottom left), and specific internal energy (bottom right) over the first ~ 30 s post bounce from model 16TI_SFHo. Time evolution is marked by evolution from white to full color (blue for density, purple for temperature, green for pressure, and orange for internal energy), with the shading indicated by the colour bar. The original two piece piece-wise power-law floor (density, pressure, and internal energy) is marked with a solid black line (flat floor at 10^4 K for temperature). The final five piece piece-wise power-law floor (density, pressure, and internal energy) is marked with a dotted black line (two piece power-law to flat floor for temperature).	124
4.6	Snapshot of the specific internal energy at three points in time shortly after disk formation as labelled in the fiducial model 16TI_SFHo. Limits are selected to highlight specific internal energy differences between the low density polar funnels, and the accretion flow at the inner edge of the disk.	125
4.7	Variation of the theta factor f_θ across all polar angles. f_θ varies from 1 at the poles to a value $\tilde{\theta}_{\text{eq}}$ at the equator. The drop off rate is controlled by $\tilde{\theta}_w$, with higher values dropping off more quickly as the polar angle moves away from either pole, with five examples plotted as labelled.	127
4.8	Same as Figure 4.5, except variables represent an average of the $+\hat{z}$ and $-\hat{z}$ polar slices. Note that floors have a different scale factor here due to the theta factor f_θ described in section 4.4.	128

4.9	Dimensionless pressure gradient and poloidal velocity gradient along the equator of the <code>16TI_SFHo</code> model at the start of the <code>FLASH</code> simulation. At this point, the shock has not yet formed, so the scale heights are representative of the progenitor profile alone. The threshold values used to mark the shock front is marked with a dashed black line. . . .	131
4.10	Snapshot of the three shock tracking variables (dimensionless pressure gradient, dimensionless poloidal velocity gradient, and ^{56}Ni mass fraction) from model <code>16TI_SFHo</code> . Radial shock positions $r_s(\theta)$ found by the shock tracking algorithm are marked with red dots. The shock front is fit by a 10th order Legendre polynomial which is marked by the grey line.	132
4.11	Schematic of the three condition shock tracking algorithm used within the collapsar for a generic shock geometry. The shock front is marked with a thick black line, arrows show the inward radial search performed by the shock tracking algorithm. The condition used to mark the shock front position is one of three conditions as labelled corresponding to Equation 4.20.	135

List of Symbols

Constants

\hbar	Planck constant.	$1.05457266 \times 10^{-27}$ erg s
π	Pi.	3.14159265359
a	Radiation density constant.	7.5646×10^{-15} erg cm ⁻³ K ⁻⁴
c	Speed of light in a vacuum.	$2.99792458 \times 10^{10}$ cm s ⁻¹
G	Gravitational Constant.	6.67259×10^{-8} cm ³ g ⁻¹ s ⁻²
k_B	Boltzmann Constant.	1.380658×10^{-16} erg K ⁻¹
M_\odot	Solar Mass.	1.98847×10^{33} g

Latin

\dot{J}_{bh}	Rate of change of the black hole angular momentum
\dot{M}_{acc}	Mass accretion rate
\dot{M}_{bh}	Rate of change of the black hole mass
\dot{M}_{in}	Mass inflow rate across the inner radial boundary
\dot{M}_{out}	Mass outflow rate across a threshold
ℓ	Spherical harmonic index
$\mathcal{F}()$	Fourier transform
\mathcal{F}_k	k th Fermi integral
\mathbf{T}	Viscous Stress Tensor
\mathbf{v}_p	Poloidal velocity
\mathbf{X}	Mass fraction vector
A	Nucleon Number
a_ℓ	Legendre coefficients
a_{bh}	Dimensionless black hole spin parameter

B	Nuclear binding energy per unit mass
Be	Bernoulli parameter
c_s	Sound speed
dV	Spherical volume element
E_{tot}	Total energy
f	Frequency
f_θ	Polar angle floor factor
f_r	Radial floor factor
f_{floor}	Floor function
H	Scale Height
H_P	Pressure scale height
i	Iteration index
J	Angular Momentum
j	Specific Angular Momentum
J_{bh}	Black hole angular momentum
j_K	Keplerian specific angular momentum
K_∞	Asymptotic kinetic energy
K_{ej}	Kinetic energy of ejected material
k_{rad}	Angular momentum radial constant
L	Luminosity
M	Mass
M_{bh}	Black hole mass
M_{df}	Black hole mass at disk formation
$M_{\text{ej,part}}$	Total ejecta mass sampled by the ejected tracer particles
M_{ej}	Mass Ejected
m_{enc}	Enclosed mass / Lagrangian mass coordinate
M_g	Gravitational mass
$M_{^{56}\text{Ni}}$	Ejected ^{56}Ni mass
n_n	Neutron number density

$N_{\text{part,ej}}$	Number of tracer particles unbound at the end of the simulation
n_{part}	Number of tracer particles remaining in the domain
n_{p}	Proton number density
n_{Q}	Quantum concentration
P	Pressure
P_{ℓ}	ℓ th Legendre polynomial
P_{rad}	Radiation pressure
Q	Heating
q	Specific heating
Q_{ν}	Post-shock integrated net neutrino cooling rate
q_{ν}	Specific net neutrino heating/cooling
q_{cool}	Specific cooling including net neutrino cooling and nuclear dissociation
q_{nuc}	Specific nuclear heating rate
Q_{visc}	Post-shock integrated viscous heating rate
q_{visc}	Specific viscous heating rate
r	Radial coordinate
$r_{\text{circ,A}}$	Artemova circularization radius
$r_{\text{circ,N}}$	Newtonian circularization radius
r_{circ}	Circularization radius
r_{circ}^*	Modified circularization radius
r_{ej}	Mass ejection tracking radius
R_{ff}	Characteristic free-fall distance
r_{g}	Gravitational radius
r_{h}	Black hole event horizon radius
$r_{\text{in,new}}$	Updated inner radial bound
r_{in}	Inner radial bound
r_{isco}	Innermost stable circular orbit radius
R_{i}	Transition radii
r_{s}	Shock radius

s	Entropy per baryon
s_i	Powerlaw slope
T	Temperature
t	Time
t_{ADAF}	NDAF to ADAF transition time
t_{bh}	Black hole formation time
t_{bounce}	Core bounce time
t_{CCSN}	Core Collapse Supernova timescale
t_{df}	Disk formation time
T_{floor}	Temperature floor
T_{guess}	Newton-Rhapson temperature guess
t_{GW}	Gravitational Wave inspiral timescale
t_{max}	Maximum simulation time
T_{NSE}	Nuclear Statistical Equilibrium Temperature
t_{peak}	Supernova light curve peak time
T_{rad}	Radiation temperature
t_{sb}	Shock breakout time
T_{solution}	Newton-Rhapson solution temperature
v	Speed/Velocity (scalar/vector)
v_{∞}	Asymptotic velocity
v_{esc}	Escape speed
v_{p}	Poloidal velocity
v_{r}	Radial speed
W_0	Floor normalization
W_{floor}	Total floor function
X	Mass Fraction
x	Cartesian x coordinate
x'	Fermi integral integration variable
X_{atm}	Atmospheric mass fraction

$X_{^{56}\text{Ni}}$	^{56}Ni mass fraction
Y	Abundance
y	Cartesian y coordinate
$Y_{\text{e,min}}$	Minimum electron fraction
Y_{e}	Electron Fraction
Z	Proton Number
z	Cartesian z coordinate

Greek

α	Viscous Parameter
$\bar{\nu}_{\text{e}}$	Electron Anti-Neutrino
β	Spin parameter
χ	Nuclear binding energy
δT	Small temperature increment
ϵ	Specific Internal Energy
η	Degeneracy
Γ_{ν}	Charged-current rates
κ	Opacity
μ	Chemical potential
μ_{n}	Neutron chemical potential
μ_{p}	Proton chemical potential
ν	Viscosity
ν_{e}	Electron Neutrino
ν_{x}	“Heavy” Neutrinos
Ω	Angular Velocity
ω	Partition function
Ω_{K}	Keplerian angular velocity
Φ	Gravitational potential
ϕ	Azimuthal Angle
Φ_{bh}	Pseudo-Newtonian black hole potential

ρ	Density
τ_{NDAF}	NDAF phase duration
Θ	Nuclear network rates
θ	Polar Angle
$\tilde{\theta}_{\text{eq}}$	Equatorial floor factor parameter
$\tilde{\theta}_{\text{w}}$	Polar angle floor width parameter

Abbreviations

***p*-nuclei** Proton rich nuclei.

***r*-process** Rapid Neutron Capture Process.

***rp*-process** Rapid Proton Capture Process.

***s*-process** Slow Neutron Capture Process.

1D One dimensional.

2D Two dimensional.

3D Three dimensional.

ADAF Advection Dominated Accretion Flow.

BH Black Hole.

BHNS Black Hole-Neutron Star.

BL Broad lined.

BNS Binary Neutron Star.

CCSNe Core Collapse Supernovae.

EM Electromagnetic.

EOS Equation of State.

FRDM Finite-Range Droplet Macroscopic.

GR General Relativistic.

GRB Gamma Ray Burst.

GRMHD General Relativistic Magneto-hydrodynamics.

GW Gravitational Wave.

HD Hydrodynamics.

HSE Hydrostatic Equilibrium.

ISCO Innermost Stable Circular Orbit.

IGRB Long Gamma Ray Burst.

LIGO Laser Interferometer Gravitational-wave Observatory.

MHD Magneto-hydrodynamics.

MRI Magneto-rotational Instability.

NDAF Neutrino Dominated Accretion Flow.

NR Newton-Rhapson.

NS Neutron Star.

NSE Nuclear Statistical Equilibrium.

PNS Proto Neutron Star.

SASI Spherical Accretion Shock Instability.

SN Supernova.

SNe Supernovae (plural).

WR Wolf-Rayet.

ZAMS Zero Age Main Sequence.

Chapter 1

Introduction

1.1 Motivation

The question of how the elements we see around us and in our solar system were formed is fundamental to many questions in astrophysics. Big Bang nucleosynthesis set the chemical composition of the early universe, with the production of hydrogen and helium (and a small amount of lithium and deuterium) in a roughly 3:1 ratio as the universe expanded and cooled shortly after the Big Bang (Kolb & Turner, 1990). To this day, the chemical composition of the universe is still dominated by this initial Big Bang nucleosynthesis, with only $\sim 2\%$ of this initial H and He having undergone various nucleosynthetic processes to create the variety of elements seen across the periodic table (Asplund et al., 2009).

Nucleosynthesis of elements beyond ${}^4\text{He}$ continued with stellar nucleosynthesis (Burbidge et al., 1957), starting with the formation of the first stars ~ 200 Myr after the Big Bang (Spergel et al., 2003). Stellar nucleosynthesis utilizes nuclear fusion in the cores of stars, building up heavier elements and injecting nuclear energy into the star to maintain hydrostatic equilibrium (HSE). The various stages of fusion require monotonically increasing temperatures to produce increasingly heavier elements. Massive stars ($> 8M_{\odot}$) are capable of fusing, through several stages, hydrogen to iron peak elements (Hoyle 1946 and Hoyle 1954) through exothermic reactions. Further fusion reactions are cut off due to ${}^{56}\text{Fe}$ being an isotope with nearly the high-

est binding energy per nucleon (Fewell, 1995), thus further fusion reactions would be endothermic, requiring energy, rather than providing energy, as would be required to maintain HSE. These elements can then be dispersed into the interstellar medium at the end of these stars' lifetimes, increasing the metallicity of the next generation of stars (Tinsley, 1980) via supernova explosions.

Explosive nucleosynthesis can occur in astrophysical transient events such as Type Ia supernovae. While the progenitor system (or systems) for these explosions is an open question, most models suggest a runaway nuclear explosion of either one or two white dwarf stars triggered either by accretion onto a white dwarf, or the merger of a binary white dwarf system (Liu et al., 2023). This thermonuclear explosion fuses nuclear fuels (H, He, C, O, or potentially Ne) to produce elements around iron (Hoyle & Fowler, 1960). The pileup of elements around iron in the solar abundance distribution (due to the stability implied by a maximum of the nuclear binding energy) results in these elements being called “iron peak” elements or “iron group elements” (Figure 1.1). The production of elements much beyond iron by type Ia supernovae is more difficult due to the endothermic nature of these reactions. Yet, measurements of chemical abundances in the solar system through observations of the solar atmosphere (early works by Russell 1929, Suess & Urey 1956, and Goldberg et al. 1960), and through the use of mass spectroscopy of meteorites, suggests the presence of heavy elements including the Lanthanides ($57 \leq Z \leq 70$) and Actinides ($89 \leq Z \leq 102$), raising questions about which nucleosynthetic process can explain the production of these heavy isotopes.

The slow neutron capture process (*s*-process) (Burbidge et al. 1957 and Cameron 1957) is one of the nucleosynthesis paths for producing elements heavier than the iron peak. This process takes advantage of free neutrons produced by nuclear fusion reactions, being captured on seed nuclei, building up their mass. Unlike fusion reactions which require much higher temperatures, neutron captures can occur at relatively low temperatures, as a neutral particle does not need to overcome the Coulomb barrier

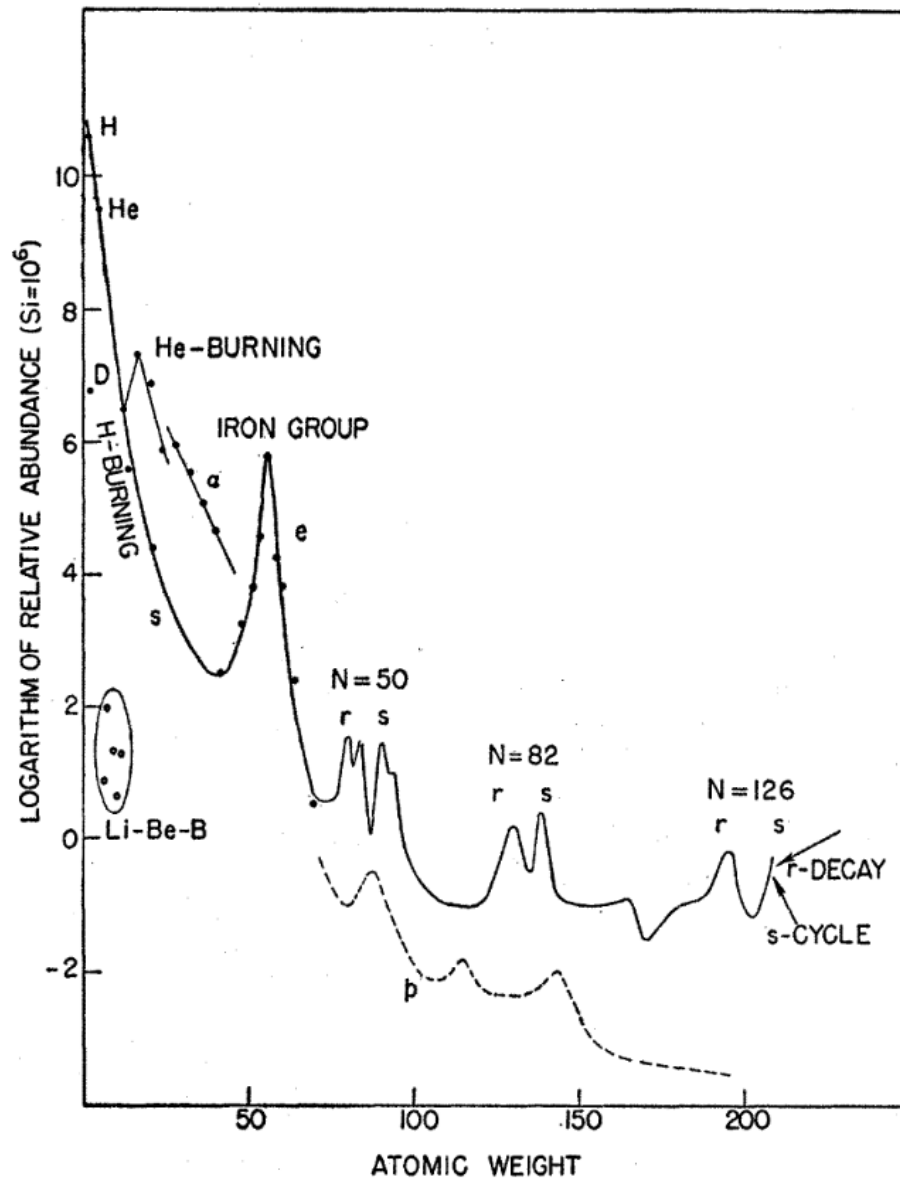


Figure 1.1: Figure 1 of Burbidge et al. (1957) reproduced via licence number RNP/24/JUL/081087. Schematic curve of atomic abundances as a function of atomic weight based on the data of Suess & Urey (1956).

in order to be captured onto a nucleus (Chadwick, 1932). The capture of neutrons is slow in comparison to the β^- decay timescale, thus as neutrons are captured onto a seed nuclei, the isotope produced will β^- decay before another neutron can be captured. The *s*-process is expected to produce about half of elements heavier than iron we see in the galaxy (Johnson, 2019), with low-mass stars confirmed as one of the production sites via observation of radioactive technetium (Merrill, 1952).

The remaining, roughly half of elements heavier than iron are produced by the rapid neutron capture process (*r*-process) (Burbidge et al., 1957). The *r*-process involves the capture of neutrons on seed nuclei rapidly compared to the β^- decay timescale, with seed nuclei capable of capturing several neutrons before a β^- decay occurs. Thus, the *r*-process requires an environment that is significantly neutron-enriched (see Cowan et al. 2021 for a recent review). Unlike the *s*-process, which produces free neutrons via certain nuclear fusion reactions, the neutron excess in the *r*-process material is generated by the neutronization of degenerate material via neutrino emission and absorption (with early works on equilibrium electron fraction in degenerate, nuclear statistical equilibrium conditions by Tsuruta & Cameron 1965). Traditionally, core collapse supernovae (CCSNe) had been considered candidates for the *r*-process, as well as black hole (BH) - neutron star (NS) mergers (BHNS) (Lattimer & Schramm, 1974), or binary neutron star (BNS) mergers. Recently, the binary neutron star merger event GW170817, first detected as a gravitational wave signal by Advanced LIGO and Virgo (Abbott et al., 2017), has since been shown to be consistent with the production of *r*-process elements by observations and modeling of its kilonova light-curve (compilation of the various followup observations of GW170817 by Villar et al. 2017), and the presence of specific *r*-process nuclei such as ^{254}Cf may be a distinguishable factor in the heating rate (Zhu et al., 2018). Currently, CCSNe models that explode have problems making heavy *r*-process elements due to insufficient neutronization of the ejecta (Janka & Bauswein, 2022). Based on GW170817 alone, the merger rate estimate and the yield per event point to BNS mergers being

a significant if not dominant source of r -process enrichment in the galaxy (Rosswog et al., 2018).

Finally, the solar abundance pattern suggests the presence of relatively small quantities of stable, slightly proton-rich (relative to the “valley of stability” in the nuclear chart) isotopes that cannot be explained by the r - or s -processes (and subsequent β^- decays) alone, known as p -nuclei (Burbidge et al., 1957). Several mechanisms for producing these elements have been proposed, including the γ -process, which is photodisintegration of s -process and r -process nuclei to produce proton-rich nuclei (Woosley & Howard, 1978). Also, the rapid proton capture process (rp -process), which is analogous to the r -process on the proton-rich side of the valley of stability, though with notable restrictions in temperature due to the need to overcome the Coulomb barrier for charged particle captures (Wallace & Woosley, 1981). As well, the νp -process, which acts in proton-rich environments with antineutrino absorptions producing neutrons which are immediately captured on proton-rich nuclei, potentially allowing for the production of heavier p -nuclei than the rp -process is capable of producing (Fröhlich et al., 2006).

Having identified nucleosynthetic processes capable of producing heavy isotopes present in the solar abundance distribution, the question of which astrophysical sites support the operation of these nucleosynthesis processes is still not settled, including whether the relative quantities of the heavy isotopes produced by any one of these events, and whether the frequency of these events, are sufficient to explain the heavy isotope abundances we observe in the solar system and in our galaxy. Focusing on r -process element enrichment, an open question that remains is whether BNS mergers alone can explain the galactic r -process enrichment. One of the main challenges to BNS mergers being the sole source of r -process elements is related to the timescale between star formation, and the enrichment event. BNS mergers occur after not only the timescale of a massive star lifetime culminating in a SN explosion and leaving a NS remnant, but also require time for the binary system to inspiral via the emission

of gravitational waves. Observations of BNSs in the Galaxy suggest a characteristic inspiral timescale of $t_{\text{GW}} \sim 10^8$ years (Weisberg & Huang, 2016).

Somewhat controversial evidence exists which suggests the need for an r -process element enrichment event on shorter timescales than that of BNS mergers (Mathews & Cowan, 1990). The argument is based on the observation of europium abundances in low metallicity stars in the galactic halo, with the stellar ages implying prompt r -process enrichment that cannot be explained by BNS mergers alone due to their delay time from the onset of star formation. However, McWilliam et al. (1995) argues, based on spectroscopic analysis of extremely metal-poor halo stars, that heavy element abundances have significant dispersion, which reflects scatter in the initial composition of the stars, which may compromise the predicted early europium abundances. Additionally, it has been argued by Ishimaru et al. (2015) that the europium enrichment of extremely low metallicity stars may be explained by a hierarchical galactic merger scenario (rather than uniform stellar evolution through the entire halo), which allows for lower star formation efficiency in lower mass sub halos. This would allow for a long timescale r -process enrichment events such as BNS mergers to explain the europium enrichment at low iron enrichment (early times in the Galaxy’s life). Ultimately, there may be a need for a short timescale r -process element enrichment event to explain the europium abundances we see in halo stars.

1.2 Nucleosynthesis in Collapsars

Collapsars (Woosley, 1993) are one alternative r -process enrichment event that occurs on CCSNe timescales after star formation ($t_{\text{CCSNe}} \lesssim 10^7$ years).

Massive stars with mass below the pair instability limit ($8M_{\odot} \lesssim M \lesssim 140M_{\odot}$) undergo core-collapse at the end of their lifetimes. This occurs after a series of stable nuclear burning stages during the lifetime of the star, producing successively heavier elements, culminating in an inert core (no nuclear burning) supported by electron degeneracy pressure, and surrounded by an onion shell-like structure undergoing var-

ious stages of fusion (Woosley et al. 2002 for a review). With ash from fusion in the shell burning layers of the star increasing the core mass, eventually the electron degeneracy pressure is insufficient to support the star, and the core collapses. The collapse is halted with the formation of a protoneutron star (PNS) supported by the strong interaction at high densities, which becomes repulsive. The collapse overshoots the hydrostatic equilibrium supported by nuclear forces, rebounding and launching a shock wave moving radially outward from the PNS surface. As the shock wave moves outwards, energy is lost to the photo-dissociation of nuclei, and the emission of electron neutrinos. Both of these processes lead to the stalling of the shock wave (Janka & Bauswein 2023 for a review).

The default explosion mechanism in CCSNe is the delayed neutrino mechanism (Wilson, 1985), in which neutrinos and antineutrinos produced by particle reactions in the core of the PNS radiate outward from the neutrinosphere of the PNS, injecting some fraction of their energy in the “gain layer” behind the shock wave (where neutrino heating exceeds neutrino cooling) (Bethe & Wilson, 1985). If there is sufficient energy injection, the shock wave will begin to expand again, eventually leading to a successful supernova explosion, leaving a NS remnant. If there is insufficient energy injection, the shock wave will collapse back, resulting in a “failed supernova”, leaving a BH remnant.

A subset of these massive stars strip their hydrogen- and a fraction or all of their helium- envelopes due to stellar winds throughout their lifetimes (observed as Wolf-Rayet stars) (Crowther 2007 for a review). These stars undergo what is referred to as a stripped-envelope supernova (Filippenko, 1997) at the end of their lives, exhibiting a lack of hydrogen and a lack of/weak helium absorption features in the spectrum of their explosion, referred to as Type Ic SN. Type Ic-BL SNe are a subclass, which exhibits broad lined spectral features owing to extreme expansion velocities of $15,000 - 30,000 \text{ km s}^{-1}$ (Modjaz et al., 2016). To date, more than 50 (Dainotti et al., 2022) Ic-BL SNe have been observed to coincide with observed long-duration

gamma-ray bursts (IGRBs). While a progenitor of this type of supernovae has not yet been directly observed, a proposed progenitor system for these SNe are collapsars (MacFadyen, 2003).

Collapsars (Woosley, 1993) are rapidly rotating stars that undergo core-collapse at the end of their life. These progenitors are unable to explode via the delayed neutrino mechanism. With the angular momentum profile increasing radially outward, after some time a centrifugally supported accretion disk forms around the central BH. This central BH-accretion disk system is theorized to be capable of driving a relativistic jet powering the IGRB, and a sub-relativistic disk outflow that can potentially support the operation of the r -process due to neutrino-induced neutronization (Pruet et al., 2003).

1.3 Thesis Objectives

The objectives of this thesis are to perform long-term, global simulations of collapsars, focusing on the disk outflow, in order to explore the questions of whether the disk wind alone is capable of producing a successful explosion of the star and to support the operation of the r -process. More generally, these simulations can also provide other observational predictions that would allow diagnosing the physics of these explosions, should they occur at observable distances.

1.4 Overall Approach

One of the main uncertainties in collapsar simulations that has important implications for nucleosynthesis calculations is how much, if any neutronized material can be carried by the disk outflow. The first simulations of the disk wind that include neutrino emission and absorption and employed GRMHD with a fixed metric (Siegel et al. 2019 and Miller et al. 2020) did not self-consistently create their accretion disk (using an equilibrium torus as initial condition instead), and only evolved the disk

for $\mathcal{O}(100 \text{ ms})$. We aimed to create a lower-cost computational model to allow for self-consistent disk formation, and expansion of the shock wave to the stellar surface ($t_{\text{sb}} \sim 100 \text{ s}$), thus requiring global simulations. Our global model was designed to produce estimates of ejecta masses, velocities, and tracer particle evolution to allow for detailed nucleosynthesis calculations in post-processing.

For our simulations, we employ finite volume hydrodynamic methods, which maximize conservation of mass, momentum and energy, thus capturing shocks well.

Prior to BH formation, the evolution of the collapsar is sensitive to general relativistic effects and the neutron star equation of state, thus we evolve our progenitor stars (rapidly-rotating Wolf-Rayet stars) with the open-source, spherically-symmetric neutrino radiation hydrodynamic code `GR1D` (O'Connor & Ott, 2010). This code solves the general relativistic hydrodynamics equations and makes use of a three flavour grey neutrino leakage scheme (a local, smooth interpolation between diffusive and free-streaming transport for emission, with a lightbulb-type approximation for absorption, thus computationally inexpensive). Additionally, `GR1D` accounts for rotational effects, approximately accounting for centrifugal acceleration, and conserving angular momentum. The duration of this step is $\sim 1 \text{ s}$ until BH formation, and determines the initial condition for our main simulation of the collapsar disk formation and evolution, which is based on the `FLASH` code (Fryxell et al., 2000; Dubey et al., 2009).

In order to achieve the desired simulation duration, and the range of physical scales necessary to resolve from the accretion disk out to beyond the surface of the star in our main simulation, we have to make a series of approximations, given our finite computational capabilities. First, we take advantage of the natural symmetry axis introduced by the rotation of the system. While the system can have non-axisymmetric perturbations when modelled in three dimensions, departures from hydrostatic equilibrium are not large, and thus we should expect the gravitational field to be close to axisymmetric. The behaviour of turbulence varies between two and three dimensions,

with energy flowing from small to large scales in two dimensions, while flowing from large to small scales in three dimensions (Benavides & Alexakis, 2017). However this behavior can change in the case of rapid rotation, charged fluids, or strong magnetic fields. While the exact behaviour of turbulence in the disk may vary in axisymmetry as compared to full three dimensions (i.e. varying the turbulent pressure), the approximation to the mass inflow and outflow rates on viscous timescales suggests the overall energetic differences will be small. Further, the use of axisymmetry is expected to accentuate axial flows, and neglect non-axisymmetric instabilities, suggesting the overall geometry of the shock-front may vary in three dimensions at late times. However, axisymmetry is a reasonable approximation for a low-cost computational model. Note that we also account for evolution of the angular momentum of the fluid, which effectively makes this a two and a half dimensional simulation.

General relativistic effects are only dynamically important near the central BH, where the gravitational potential differs from a Newtonian potential, and the disk outflow is produced at length scales much larger than the event horizon of the BH. This allows us to evolve the Newtonian hydrodynamics equations with the modified gravitational potential of Artemova et al. (1996) to reproduce the plunge of material inside the innermost stable circular orbit (ISCO) of the BH, rather than the full general relativistic hydrodynamic equations which are much more computationally expensive to model.

Collapsars are powered by a rotationally-supported disk, differing from magneto-rotational SNe, where the magnetic field is dynamically important and modifies the explosion mechanism. In collapsars, the main effect of the magnetic fields is to drive turbulence in the accretion disk via the magneto-rotational instability (MRI). This causes viscous heating of the accretion disk, drives the disk wind, and transports angular momentum within the disk. We use the α -viscosity prescription of Shakura & Sunyaev (1973), which models the viscous angular momentum transport and heating of the disk caused by the MRI via an imposed shear viscosity. This method has

a long history of use, and has been shown to approximate well the mass accretion rate and mass outflow rate of an equivalent black hole accretion disk system (in the context of BNS mergers) evolved in GRMHD by Fernández et al. (2018) on timescales comparable to the viscous timescale of the system (i.e., beyond prompt magnetically-dominated transients). While turbulent mixing is suppressed in two dimensional, fully viscous hydrodynamics (Boffetta & Ecke (2012) for a review), the α -viscosity prescription that we employ (Stone et al., 1999) does not preclude mixing in the disk, due to the imposition of shear viscosity only in the azimuthal direction. Thus, we do not expect the choice of axisymmetry to result in a significant change to mixing within the disk. These assumptions (pseudo-Newtonian gravity and shear viscosity in hydrodynamics) preclude the formation of a relativistic jet, which is powered by the winding of magnetic field lines by the accretion disk, creating a buildup of magnetic pressure near the poles and potentially driving a small amount of matter out at relativistic speeds towards the poles of the star (Blandford & Znajek, 1977). However, the quantity of r -process elements ejected by the jet are estimated to be too small to explain the solar abundance by several orders of magnitude, with the collapsar disk outflow predicted to be a larger source of r -process elements (Pruet et al., 2003). For this reason, we study a collapsar explosion powered solely by sub-relativistic disk outflow using the assumptions mentioned above.

Neutrino heating and cooling are important in collapsars, due to the densities and temperatures reached in the accretion disk. Neutrino and antineutrino emission and absorption modify the ratio of neutrons to protons in the disk and outflows (due to the charged-current weak interactions), quantified by the electron fraction (Y_e):

$$Y_e = \frac{n_p}{(n_n + n_p)}, \quad (1.1)$$

where n_p is the proton number density, and n_n is the neutron number density. Additionally, the energetics of the disk are modified by neutrinos, acting as the only cooling channel at characteristic disk densities. The details of neutrino emission and

absorption are important, but not crucial to the dynamics of the disk outflow, and for that reason we choose a simplified three species neutrino leakage scheme for emission and a light-bulb style absorption approximation that captures the dominant effects of cooling and Y_e evolution (Fernández & Metzger 2013; Metzger & Fernández 2014; Lippuner et al. 2017a; Fernández et al. 2022).

Additionally, while nuclear reactions are a subdominant energy source in our scenario, they are fundamental to the question of heavy element nucleosynthesis that we address in this thesis. However, nuclear reaction networks capable of modelling production of elements heavier than iron involve thousands of isotopes, and are too computationally costly to be run in every cell and at every time step of the simulation. Based on the assumption that the dominant contribution to nuclear energy injection is due to fusion reactions up to ^{56}Ni (Timmes et al., 2000), we choose to evolve the small 19-isotope nuclear network of Weaver et al. (1978) at every timestep of our simulation when below the nuclear statistical equilibrium (NSE) temperature $T_{\text{NSE}} = 5 \times 10^9$ K, and implement an NSE solver¹ for compositional and nuclear energy changes above the NSE temperature. Note that while the “ignition accretion rate”, where neutrino cooling becomes dynamically important, corresponds to temperatures $T \sim 10^{10}$ K, which is near the transition to nuclear statistical equilibrium T_{NSE} , these are physically distinct concepts, as the former involves the weak interaction and the latter the strong interaction. Nucleosynthesis calculations with a much larger number of isotopes are then performed in post-processing using `SkyNet` (Lippuner & Roberts, 2017) and passive tracer particles, which are placed in the computational domain at the point of disk formation, and evolved for the duration of the simulation, tracking the hydrodynamic variable values of each fluid parcel as it is ejected from the star.

We predominantly use the Bernoulli parameter to identify unbound ejected material in our simulations. While this parameter is an imperfect criterion due to additional changes to the energy imparted by source terms (neutrino heating/cooling,

¹We use the NSE solver written by F. Timmes, available at `cococubed.asu.edu`

nuclear energy injection, viscous heating, etc.) after ejection, the physics of the problem are such that cooling terms are unlikely to cause an unbound fluid element to become bound again at late times. For completeness, we explore the use of different unbinding criteria in Chapter 2.

The behaviour of the accretion disk is controlled by the mass accretion rate onto the BH, which sets the balance of various heating and cooling processes. Collapsar accretion disks are expected to have accretion rates in excess of $\sim 3 \times 10^{-3} - 10^{-1} M_{\odot} \text{ s}^{-1}$ (e.g. Siegel et al. (2019)). Thus the BH-accretion disk in collapsars may act as neutrino dominated accretion flows initially, when mass accretion rates are highest, and advection dominated accretion flows at later times, when accretion rates drop off. Advection dominated accretion flows are prone to outflows due to their positive Bernoulli parameter (Narayan & Yi, 1994), while Neutrino dominated accretion flows are more bound due to the addition of dynamically important neutrino cooling. Thus we expect stronger outflows during the Advection Dominated Accretion Flow phase relative to the Neutrino Dominated Accretion Flow phase.

Source terms to the Euler equations accounting for gravity, alpha viscosity, nuclear heating, and net neutrino heating/cooling, are solved in `FLASH` using an operator split method (Strang, 1968). Each timestep of evolution in the simulation variables are updated in two half-timesteps, with hydrodynamic variables updated first conservatively using fluxes from the Riemann solver, then source terms are updated depending on their implementation, this stepping method is then repeated for the second half-timestep.

Current computational models of collapsars are separated into simulations that focus on collapsar jets (focusing on the relativistic (M)HD aspects) or simulations that focus on collapsar disk outflows (focusing on the microphysics and neutrino transport). Nucleosynthesis in collapsar jets has been modelled in axisymmetry with tracer particles (Pruet et al. 2003, Fujimoto et al. 2007, Ono et al. 2012, Nakamura et al. 2013, and Leung & Nomoto 2023) with elements up to the third r -process peak

being produced. Global, relativistic collapsar jet simulations in full 3D GRMHD have been performed by Gottlieb et al. (2022), illustrating the capability of the collapsar jet to make its way to the surface of the star, ejecting material. However, as mentioned above, the quantity of r -process elements ejected by the jet are estimated to be too small to explain the solar abundance by several orders of magnitude, with the collapsar disk wind outflow predicted to be a larger source of r -process elements (Pruet et al., 2003).

There is a significant history of multi-dimensional global collapsar simulations (Bodenheimer & Woosley, 1983; MacFadyen & Woosley, 1999; Proga et al., 2003; Mizuno et al., 2004a,b; Fujimoto et al., 2006; Nagataki et al., 2007; Sekiguchi & Shibata, 2007; Harikae et al., 2009, 2010; Lopez-Camara et al., 2009; López-Cámara et al., 2010; Ott et al., 2011; Sekiguchi et al., 2011; Batta & Lee, 2016; Obergaulinger & Aloy, 2017; Nagataki, 2018; Aloy & Obergaulinger, 2021; Gottlieb et al., 2022; Janiuk et al., 2023; Shibata et al., 2023; Crosato Menegazzi et al., 2023), however, these studies did not all include the required ingredients to model neutronization of the accretion disk, and outflows through the infalling star at the same time. These ingredients being a global simulation covering the entirety of the star, self-consistent disk formation, accretion and outflow, and neutronization of the accretion disk through neutrino emission and absorption with appropriate microphysics and the evolution of Y_e . Recent, relevant papers that performed nucleosynthesis, have simulated collapsar disk outflows by evolving equilibrium tori in 3D GRMHD for short periods of time (Siegel et al. 2019 and Miller et al. 2020). However, these papers started from an equilibrium torus rather than one self-consistently produced by the rotating stellar collapse, and only evolved the torus for a short time ~ 100 ms. Additionally a crucial assumption was made that the (absent) ram pressure from the infalling stellar mantle was unimportant, thus embedding the torus in a low density uniform density medium. Nucleosynthetic predictions in these papers were strongly dependent on the assumed mass accretion rate, which sets the disk density and thus neutrino interactions and

degeneracy. Additionally, with the implementation of two different neutrino transport schemes, the ability of the disk outflow to produce third r -process peak elements was not conclusive. With these assumptions, determining whether any r -process elements produced in the disk wind were truly capable of making their way out of the star, and whether they were produced in meaningful quantities, would require longer term, self-consistent simulations. During the time of this thesis work, two other research groups have presented similar approaches to modeling global disk outflow simulations in hydrodynamics, including the relevant microphysics and neutrino interactions (Just et al., 2022a; Fujibayashi et al., 2023a,b). These models have some differences with our approach, which we discuss in Chapters 2 and 3.

1.5 Thesis Outline

The thesis follows the following structure: Chapter 2 is the first paper published based on this project, outlining the simulations themselves as well as discussion of the neutrino signal, shock oscillations, and early discussion of the prospect as an r -process element source. Chapter 3 is the second paper based on this project, which discusses additional models run in an attempt to provide an upper limit on the production of r -process elements, as well as detailing nucleosynthesis calculations performed on each model. Chapter 4 discusses additional code development I performed that was necessary for the completion of the project, and which was not detailed in either of the papers. Finally, Chapter 5 concludes the thesis.

Chapter 2

Collapsar disk outflows I: Viscous hydrodynamic evolution in axisymmetry

2.1 Introduction

The detection of numerous black hole (BH) binary mergers by the LIGO-Virgo Collaboration (Abbott et al. (2019, 2021); The LIGO Scientific Collaboration et al. (2021b,a)) has increased interest in the origin of stellar-mass BHs. With transient surveys expanding the known parameter space of time-domain astronomy, explosive stellar events such as supernovae (SNe) have been found to show diversity beyond established classes (e.g., Milisavljevic & Margutti (2018); Graham et al. (2019); Modjaz et al. (2019)). Progress in our understanding of the formation of stellar mass BHs thus requires theoretical characterization of the associated electromagnetic (EM) signatures of these events, to maximize the insight gained from observations.

The core-collapse of massive stars is thought to be the dominant formation path for stellar-mass BHs. When the progenitor mass is below the limit for the onset of pair instability, collapse always leads to the formation of a protoneutron star (O'Connor & Ott, 2011), with subsequent failure of the SN (e.g., Nadezhin (1980)), or fallback accretion in an otherwise successful SN (e.g. Colgate (1971)), leading to BH formation. Very massive stars ($M \gtrsim 250 M_{\odot}$) can also lead directly to BH formation (Fryer

et al., 2001).

The *collapsar* model (Woosley, 1993) describes a massive progenitor star with significant rotation at the time of core collapse, which fails to explode as a standard SN and forms a central BH. Collapsing material circularizes outside the innermost stable circular orbit (ISCO), forming an accretion disk. The location of disk formation depends crucially on the angular momentum profile of the progenitor, which generally is not well-known for massive stars. If the disk forms close enough to the BH for neutrino cooling to become important, a relativistic jet can be launched, resulting in a long gamma-ray burst (GRB) (e.g., MacFadyen & Woosley (1999)). An associated SN explosion could be powered by accretion disk winds (MacFadyen, 2003), or via a relativistic jet cocoon that shocks and unbinds the star (e.g. MacFadyen et al. (2001); Gottlieb et al. (2022)). If the circularization radius is too large for neutrino cooling to be important, an explosion that ejects the outer stellar layers can still be produced, but likely with a lower energy than standard SNe (e.g., Bodenheimer & Woosley (1983); Antoni & Quataert (2023)).

Collapsars have been proposed as a site of rapid neutron capture (*r*-process) element production (MacFadyen & Woosley (1999); Kohri et al. (2005)), having a shorter delay timescale after star formation than neutron star (NS) mergers (e.g., Siegel et al. (2019)), which need to experience orbital decay by gravitational wave emission before merging (Peters & Mathews, 1963). The neutron-rich conditions for the *r*-process occur when the collapsar disk achieves high enough densities that electrons are degenerate, and neutrino interactions are important (e.g., Beloborodov (2003); Chen & Beloborodov (2007)).

Production of *r*-process elements with short delay timescales may be needed to explain the europium abundances in low metallicity stars in dwarf galaxies within the local group, (Ji et al., 2016) as well as the evolution of the ratio of europium to iron in our own galaxy (e.g., Côté et al. (2017); Hotokezaka et al. (2018); Zevin et al. (2019); Kobayashi et al. (2023)). Whether collapsars have indeed the ability to contribute

with significant amounts of r -process elements remains an open question, however, as the neutron-rich matter must be ejected from the system. Recent evidence in favor of this hypothesis is the claimed detection of a kilonova from a long GRB (Rastinejad et al., 2022).

Here we study the long-term evolution of collapsar disks and their outflows using two dimensional (2D) viscous hydrodynamic simulations that include neutrino emission and absorption, as well as nuclear energy release. While our simulations are Newtonian, the BH is treated using a spinning pseudo-Newtonian potential, which allows for a good estimate of sub-relativistic, accretion-powered mass ejection at large radii (we cannot obtain a jet and investigate the production of a long GRB and/or a cocoon-driven explosion, however). The initial condition is obtained by evolving a rotating progenitor with a spherically-symmetric, general relativistic neutrino radiation-hydrodynamic code until BH formation. Our disk simulations explore variations in the strength of viscous angular momentum transport, as well as in progenitor stars, and in equation of state (EOS) used prior to BH formation. This paper focuses on the disk evolution and mass ejection, a companion paper will investigate the detailed nucleosynthesis signatures of the disk outflow.

The structure of the paper is the following. Section 2.2 describes our choice of progenitor stars, evolution up to the point of BH formation, physical assumptions and numerical setup for axisymmetric simulations, choice of model parameters, and analysis methods. The results are discussed in Section 2.3, including an overview of disk evolution, properties of the disk outflow, neutronization and neutrino emission, potential to power broad-line type Ic (Ic-BL) SNe, and a comparison of our results to similar work by other groups. A summary and discussion follow in Section 2.4. The appendices describe our implementation of nuclear burning and nuclear statistical equilibrium, and the floors used in axisymmetric simulations.

2.2 Methods

2.2.1 Progenitors and Evolution to BH Formation

We employ two stellar progenitors from (Woosley & Heger, 2006) which undergo chemically homogeneous evolution and reach the presupernova state as Wolf-Rayet stars. Model **16TI** is a $16 M_{\odot}$ zero age main sequence (ZAMS) star with metallicity 1% solar and presupernova mass $14 M_{\odot}$, and model **350C** is a $35 M_{\odot}$ ZAMS star with metallicity 10% solar and presupernova mass $28 M_{\odot}$. Both are evolved including a prescription for magnetic torques and reduced mass loss rates, and have previously been used in global collapsar simulations (e.g., Harikae et al. (2009); Lopez-Camara et al. (2009); Lindner et al. (2010); Obergaulinger & Aloy (2017); Just et al. (2022a)).

Progenitors are evolved until BH formation with the spherically-symmetric, neutrino radiation-hydrodynamic code **GR1D** version 1 (O’Connor & Ott, 2010). The code solves the equations of general-relativistic hydrodynamics with a finite-volume method, and employs a three-flavor gray leakage scheme to treat neutrino emission and absorption. Our default evolution mode employs the SFHo EOS (Steiner et al., 2013), with one model using the DD2 EOS (Hempel et al., 2012) to quantify sensitivity to BH formation time. The computational grid is uniform inside 20 km, and expands logarithmically outside until a radius $\sim 10^9$ cm at which the density is $2 \times 10^3 \text{ g cm}^{-3}$, with a total resolution of 1000 – 1200 cells depending on progenitor. BH formation is deemed to have occurred when the central density increases rapidly with time toward $\gtrsim 10^{15} \text{ g cm}^{-3}$, accompanied by a rapid decrease of the central value of the lapse function toward zero, at which point the code crashes. See (Ivanov & Fernández, 2021) for more details about simulation parameters and verification tests.

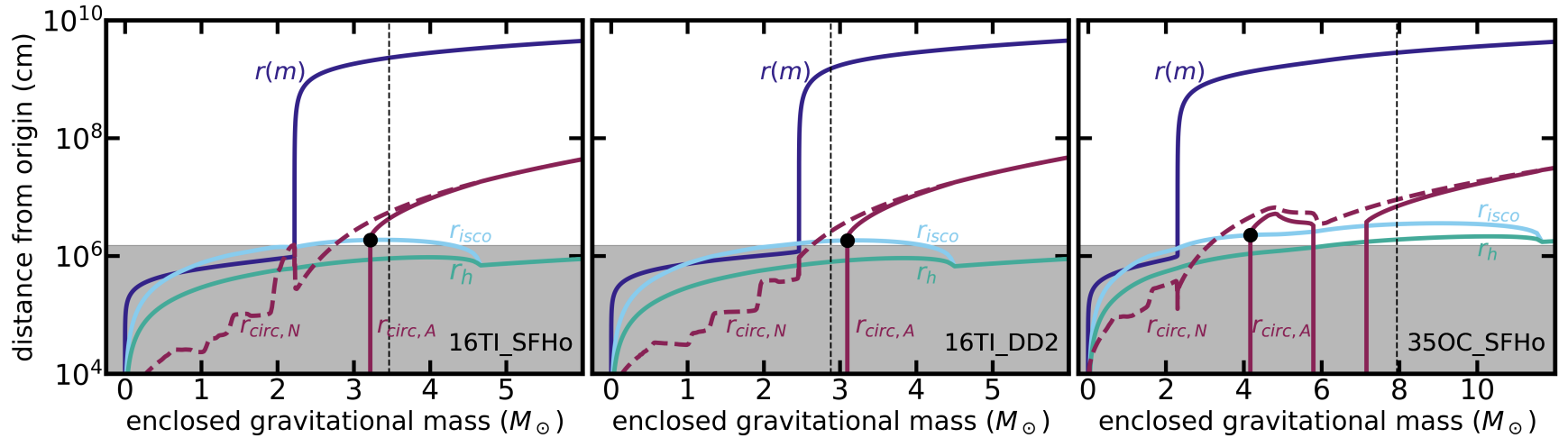


Figure 2.1: Characteristic radii as a function of enclosed gravitational mass at the last snapshot before BH formation in GR1D (Section 2.2.1) for the presupernova progenitors 16TI (SFHo EOS left, DD2 EOS center) and 350C (SFHo EOS right), evolved in all cases with approximate rotation effects. Curves show the radial coordinate (purple), ISCO radius (light blue), event horizon radius (green), and circularization radii obtained with a Newtonian potential (dashed burgundy, eq. 2.2) and with the Artemova pseudo-Newtonian potential (solid burgundy, defined by Equation 2.5). All quantities account for the spinup of the BH with the enclosed angular momentum at each mass (eq. 2.1). The gray shaded area shows the region excised initially from the computational domain for subsequent evolution in 2D with FLASH (Section 2.2.2). The black circle marks the predicted BH mass at disk formation, and the vertical dashed black line shows the actual BH mass when the shocked accretion disk forms in the FLASH simulation.

All cases are evolved accounting for rotation in **GR1D**, starting from the initial angular momentum distribution of the star. **GR1D** includes an approximate prescription for angle-averaged rotation that accounts for centrifugal effects and conservation of angular momentum (O’Connor & Ott, 2010). While this approximation provides a reasonable estimate to the delay until BH formation due to rotation effects, it cannot capture multi-dimensional phenomena such as the formation of transient accretion disks during the protoneutron star phase (e.g., the **16TI** progenitor evolution in (Obergaullinger & Aloy, 2022)).

Figure 2.1 shows spatial profiles at the last snapshot before BH formation in **GR1D**. The sharp increase in the radial coordinate with enclosed mass occurs at the surface of the protoneutron star. Also shown are the ISCO and horizon radii of a BH of mass equal to the enclosed gravitational mass and dimensionless spin a_{bh} implied by the enclosed angular momentum

$$a_{\text{bh}} = \frac{J_{\text{bh}}/M_{\text{bh}}}{r_{\text{g}} c} = \frac{c J_{\text{bh}}}{GM_{\text{bh}}^2}, \quad (2.1)$$

where J_{bh} is the total angular momentum and M_{bh} the gravitational mass of a BH that would form at that mass coordinate (as usual, $r_{\text{g}} \equiv GM_{\text{bh}}/c^2$). The ISCO and horizon radii are computed using the analytic formulae for the Kerr metric (e.g., Bardeen et al. (1972)), while the total angular momentum enclosed at each mass coordinate is computed consistently with the coordinate system in **GR1D** (equation 16 of O’Connor & Ott (2010)).

As the star continues to collapse, the BH grows in mass and changes its spin by accreting matter, sweeping through the Lagrangian mass coordinate in Figure 2.1. The subsequent evolution of collapsars is normally characterized by the Newtonian circularization radius

$$r_{\text{circ,N}} = \frac{j^2}{GM_{\text{g}}}, \quad (2.2)$$

where $j(M_{\text{g}})$ is the specific angular momentum and M_{g} is the enclosed gravitational mass. At this location, the centrifugal acceleration balances the Newtonian accelera-

tion of gravity at the equator. The circularization radius increases outward because the specific angular momentum in these progenitors increases faster than the square root of the enclosed gravitational mass (c.f., Figure 2 of Woosley & Heger (2006)).

Our post-BH evolution (Section 2.2.2) employs a pseudo-Newtonian potential Φ_{bh} to model the gravity of the BH, which yields a circularization radius $r_{\text{circ,A}}$ that differs from the Newtonian value in Equation (2.2). We use the potential of Artemova et al. (1996), which provides an ISCO for a spinning BH (Fernández et al., 2015):

$$\Phi_{\text{bh}}(r) = \begin{cases} \frac{GM_{\text{bh}}}{(\beta-1)r_{\text{h}}} \left[1 - \left(\frac{r}{r-r_{\text{h}}} \right)^{\beta-1} \right] & (\beta \neq 1) \\ \frac{GM_{\text{bh}}}{r_{\text{h}}} \ln \left(1 - \frac{r_{\text{h}}}{r} \right) & (\beta = 1) \end{cases} \quad (2.3)$$

where r_{h} is the horizon radius, and

$$\beta = \frac{r_{\text{isco}}}{r_{\text{h}}} - 1 \quad (2.4)$$

with r_{isco} the ISCO radius. In the absence of spin, $\beta = 2$ and the potential is identical to that of Paczyński & Wiita (1980). For arbitrary spins, r_{isco} and r_{h} are computed analytically as in the Kerr metric (Bardeen et al., 1972). The Keplerian specific angular momentum in the potential of Equation (2.3) can be obtained by balancing the gravitational and centrifugal accelerations at the equator

$$j_{\text{K}}^2 = GM_{\text{bh}} r (1 - r_{\text{h}}/r)^{-\beta}. \quad (2.5)$$

For a given specific angular momentum j and enclosed gravitational mass M_{g} in the progenitor, inverting equation (2.5) for r , setting $j_{\text{K}} = j$ and $M_{\text{bh}} = M_{\text{g}}$, yields the circularization radius $r_{\text{circ,A}}$ shown in Figure 2.1 for the progenitors we consider in this study. The resulting value is equal or smaller than the Newtonian circularization radius, and at small specific angular momenta there is no solution.

When $r_{\text{circ,A}} \gtrsim r_{\text{isco}}$, a shocked accretion disk is expected to form. Thereafter, accretion of matter with higher angular momentum should be halted, and the characteristic radii in Figure 2.1 are no longer predictive for higher enclosed masses. This

includes the point where r_{isco} and r_{h} merge at high enclosed mass, which would occur if the BH achieved maximal rotation, but does not occur in practice due to the existence of the accretion disk.

2.2.2 Evolution after BH formation

Once a BH forms in **GR1D**, we use the spatial distribution of thermodynamic and kinematic quantities as initial conditions for subsequent evolution, which we carry out in two-dimensional (2D) axisymmetry using **FLASH**. The mapping procedure is similar to that reported in Ivanov & Fernández (2021), using pressure, density, and composition as inputs to the EOS in order to minimize transients. The specific angular momentum profile from **GR1D** is mapped assuming cylindrical symmetry, i.e. $j(r, \theta) \propto \sin^2(\theta)$.

We use **FLASH** version 3.2 (Fryxell et al. (2000); Dubey et al. (2009)) to solve the equations of mass, momentum, energy, and baryon/lepton/charge conservation in 2D axisymmetric spherical coordinates (r, θ) , with source terms due to gravity, shear viscosity, neutrino emission/absorption, and nuclear reactions

$$\frac{\partial \rho}{\partial t} + \nabla \cdot (\rho \mathbf{v}_p) = 0 \quad (2.6)$$

$$\frac{D\mathbf{v}_p}{Dt} = -\frac{\nabla P}{\rho} - \nabla \Phi \quad (2.7)$$

$$\rho \frac{Dj}{Dt} = r \sin \theta (\nabla \cdot T)_\phi \quad (2.8)$$

$$\rho \frac{D\epsilon}{Dt} + P \nabla \cdot \mathbf{v}_p = \frac{1}{\rho \nu} \mathbf{T} : \mathbf{T} + \rho (q_{\text{nuc}} + q_\nu) \quad (2.9)$$

$$\nabla^2 \Phi = 4\pi G \rho + \nabla^2 \Phi_{\text{bh}} \quad (2.10)$$

$$\frac{\partial \mathbf{X}}{\partial t} = \Theta(\rho, T, \mathbf{X}) + \Gamma_\nu \quad (2.11)$$

where $D/Dt \equiv \partial/\partial t + \mathbf{v}_p \cdot \nabla$, $\mathbf{v}_p = v_r \hat{r} + v_\theta \hat{\theta}$ is the two dimensional (poloidal) velocity, ρ is the density, P is the pressure, ϵ is the specific internal energy, j is the specific angular momentum scalar, Φ is the gravitational potential, \mathbf{T} is the viscous stress tensor, and \mathbf{X} are the mass fractions of species considered. The rate of change of

the mass fractions caused by the nuclear network is denoted by Θ , and the specific nuclear heating from the network is denoted by q_{nuc} . The rate of change of mass fractions caused by charged-current weak interactions mediated by neutrino emission and absorption is denoted by Γ_ν , and the specific net neutrino heating rate is denoted by q_ν .

We employ the (Helmholtz) equation of state of Timmes & Swesty (2000), and extend the tabulated electron-positron quantities for $\rho > 10^{11} \text{ g cm}^{-3}$ and $T > 10^{11} \text{ K}$ with analytic expressions for a relativistic electron-positron gas of arbitrary degeneracy (Bethe et al., 1980). At densities below the minimum of the table ($\rho < 10^{-10} \text{ g cm}^{-3}$) we use an ideal gas law for electrons. For $T < 5 \times 10^9 \text{ K}$, we use the 19-isotope nuclear reaction network of Weaver et al. (1978) with the MA28 sparse matrix solver and Bader-Deuffhard variable time stepping method (e.g., Timmes (1999)). For $T \geq 5 \times 10^9 \text{ K}$, we set the abundances of these isotopes to their values in nuclear statistical equilibrium (NSE, Appendix 2.5.2).

The internal energy update (described in Appendix 2.5.1) accounts for viscous heating, neutrino heating, and nuclear heating in two separate half-timesteps. The NSE transition temperature is set initially at $1.4 \times 10^{10} \text{ K}$ for numerical reasons, up until the point of shock formation, where infalling material begins to form an accretion disk. Prior to this time, material with sufficiently high temperatures is plunging into the black hole supersonically. From disk formation onward, the NSE transition temperature is set to its default value at $5 \times 10^9 \text{ K}$. For numerical reasons, NSE is not imposed on fluid within a factor 10 of the density floor, or for atmospheric material.

Angular momentum transport is included via a shear stress tensor T with non-zero components $r\phi$ and $\theta\phi$, thus modeling conversion of shear kinetic energy into heat and turbulence (e.g., Stone et al. (1999)). The viscosity coefficient is parameterized

as in Shakura & Sunyaev (1973)

$$\nu = \alpha \frac{P/\rho}{\Omega_K} \quad (2.12)$$

with the local Keplerian angular frequency defined as

$$\Omega_K^2 = \frac{1}{r} \frac{d\Phi}{dr} \quad (2.13)$$

(see Fernández & Metzger (2013) for details). The tensor \mathbf{T} modifies j (equation 2.8) and contributes with a heating term in the energy equation (2.9). Results of axisymmetric hydrodynamic simulations using this prescription compare favorably with general relativistic magnetohydrodynamic (MHD) simulations in the advective state (Fernández et al., 2019b). To avoid numerical problems in regions of mostly radial infall, viscous heating and angular momentum transport are suppressed as $e^{-|\mathbf{v}|/v_\phi}$ for $|\mathbf{v}| > v_\phi \equiv j/(r \sin \theta)$, following a similar prescription from MacFadyen & Woosley (1999). We also cap the viscous heating at 10^6 times the internal energy per timestep, to eliminate numerical issues near the low density polar funnel. This effectively sets a minimum value for the cooling timestep limiter.

Table 2.1: List of evolved models, parameters used, and key simulation timescales. Columns from left to right show the model name, progenitor star from Woosley & Heger (2006), EOS used in **GR1D** evolution to BH formation, and viscosity parameter used in the 2D post-BH evolution. Subsequent columns show times relative to the bounce time in **GR1D**: BH formation time in **GR1D**, shocked disk formation time, mass of the BH at disk formation, shock breakout time (leading edge reaching the surface of the star), and the maximum simulation time.

Model	Progenitor	EOS	α	t_{bh} (s)	t_{df} (s)	$M_{\text{bh}}(t_{\text{df}})$ (M_{\odot})	t_{sb} (s)	t_{max} (s)
16TI_SFHo	16TI	SFHo	0.03	2.72	11.1	3.5	116	219.8
16TI_SFHo_ α 01			0.1	2.72	11.0	3.5	236	427.1
16TI_SFHo_ α 001			0.01	2.72	10.6	3.4	153	295.4
16TI_DD2		DD2	0.03	5.24	9.9	2.9	168	302.0
35OC_SFHo	35OC	SFHo		0.99	10.8	7.9	68	102.8

We include neutrino emission and absorption via a 3-species leakage scheme for emission and a lighbulb-type approximation for absorption (Fernández & Metzger (2013); Metzger & Fernández (2014); Lippuner et al. (2017a); Fernández et al. (2022)). Emission processes include electron/positron capture on nucleons, using the rates of Bruenn (1985), as well as electron-positron pair annihilation and plasmon decay using the rates of Ruffert et al. (1996). Opacities account for charged-current absorption and neutral-current scattering on nucleons. Emissivities and opacities match those used in the leakage scheme of GR1D for evolution prior to BH formation (O’Connor & Ott, 2010), with the main differences between codes being the procedure to compute the optical depth and the prescription for absorption. These neutrino processes contribute with a heating/cooling source term q_ν in the energy equation (Equation 2.9), and a rate of change of the mass fractions of neutrons and protons Γ_ν in the evolution equation for mass fractions (Equation 2.11). The electron fraction is computed from the mass fractions of ions using charge conservation

$$Y_e = \frac{\bar{Z}}{\bar{A}}, \quad (2.14)$$

with $\bar{A} = (\sum_i X_i/A_i)^{-1}$ and $\bar{Z} = \bar{A} \sum_i (X_i Z_i/A_i)$. Changes in Y_e thus occur implicitly through equation (2.11). Additional energy loss channels that do not alter the composition are included in the nuclear reaction network using the analytic fits of Itoh et al. (1996), with an additional correction factor $e^{-\rho_{11}}$ ($\rho_{11} = \rho/[10^{11} \text{ g cm}^{-3}]$) to account for neutrino trapping in high-density regions.

The Poisson equation (2.10) for the gravitational potential generated by the fluid in the computational domain is solved with the multipole method of Müller & Steinmetz (1995), as implemented in Fernández et al. (2019a). The BH contribution Φ_{bh} (Equation 2.3) is added to the $\ell = 0$ moment.

The BH is assumed to be inside the inner radial boundary of the computational domain. The mass M_{bh} and angular momentum J_{bh} of this point mass are updated at every time step with the material accreted through the inner radial boundary at

$r = r_{\text{in}}$:

$$\dot{M}_{\text{bh}} = 2\pi r_{\text{in}}^2 \int d\Omega [\rho \max(0, -v_r)] \Big|_{r_{\text{in}}} \quad (2.15)$$

$$\dot{J}_{\text{bh}} = 2\pi r_{\text{in}}^2 \int d\Omega [\rho j \max(0, -v_r)] \Big|_{r_{\text{in}}}, \quad (2.16)$$

where the fluxes employed are those computed by the Riemann solver, which maximizes conservative properties (e.g., Fernández et al. (2018)). The initial values of M_{bh} and J_{bh} are obtained from the last GR1D profile and set to the baryonic mass and angular momentum enclosed by the radius of the inner radial boundary at the beginning of the FLASH evolution. For simplicity, we do not consider the difference between baryonic and gravitational masses. The instantaneous dimensionless BH spin parameter a_{bh} is then obtained from equation (2.1). The updated values of M_{bh} and a_{bh} are then used to update the gravitational potential of the BH (Equation 2.3).

The domain uses reflecting boundaries on the upper and lower θ edges, and outflow boundaries at the inner and outer radial edges. We use a logarithmically-spaced radial grid, and a polar grid equally spaced in $\cos \theta$, as in Fernández et al. (2019a). The inner radial boundary is set so it falls between the black hole event horizon and the ISCO radius. The domain extends across polar angles from 0 to π with 112 cells, and the radial domain extends to $\sim 2\times$ the progenitor radius, depending on the progenitor, with 800 cells in total.

As the BH accretes matter, its event horizon grows. When the inner radial boundary falls below 130% the event horizon radius, we excise an integer number of cells in the direction of increasing radius from the inner boundary, setting the new inner radial boundary to be $r_{\text{in,new}} \simeq r_{\text{h}} + 0.75(r_{\text{isco}} - r_{\text{h}})$. Material in the excised cells is assumed to be instantaneously accreted onto the BH, increasing its mass and total angular momentum. An equal number of radial cells are added on the outside of the domain and are filled with atmospheric material in order to keep the total number of radial grid cells constant. The initial density, pressure and internal energy of this ambient material outside the star decreases as a power-law in radius.

In the case of the 16TI models, the accretion onto the black hole is small enough over the timescale of the simulation that the inner boundary remains between the horizon and ISCO for the duration of the simulation. In the case of the 350C_SFHo model, the accretion rate is significant over this timescale, requiring the movement of the radial boundaries at multiple times throughout the simulation.

We use a floor of internal energy, pressure, and density with radial and angular dependence, as described in Appendix 2.6. Whenever the density floor is applied, the increase in matter is marked as atmospheric, and has an electron fraction consistent with material in the cell before the floor is applied. If the cell is in NSE, this is achieved by adding neutrons and protons consistent with the desired electron fraction. If the cell is not in NSE, ^{56}Ni and either neutrons or protons are added consistent with the desired electron fraction.

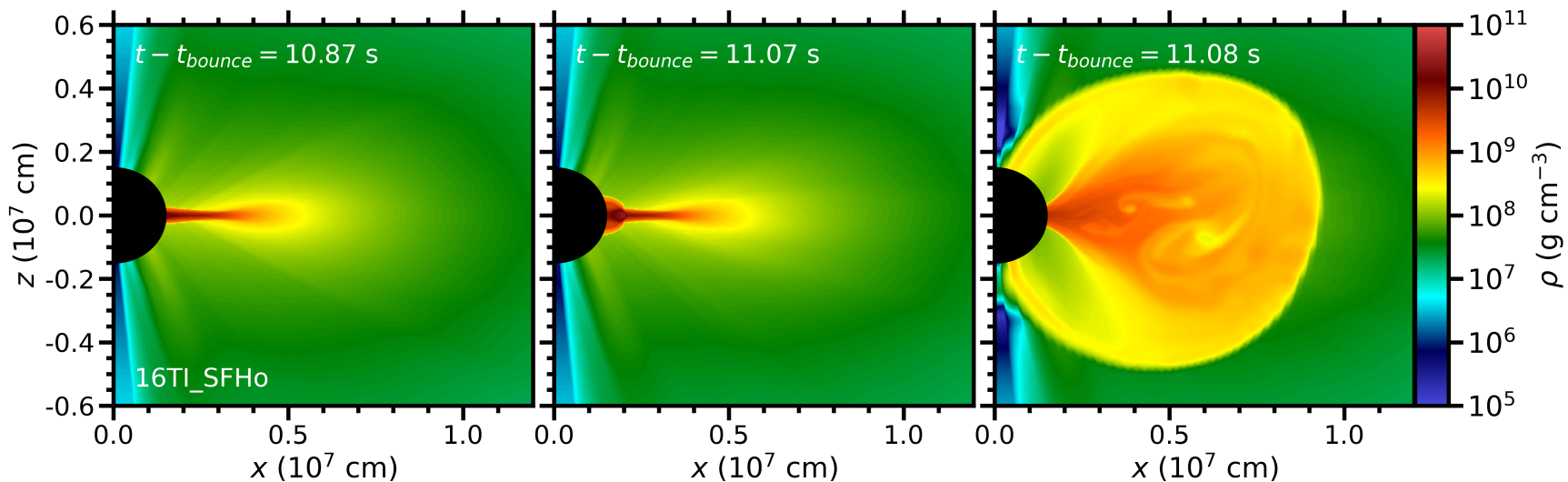


Figure 2.2: Transition from *dwarf disk* to thermalized disk in model 16TI_SFHo, with time after core bounce in the preceding GR1D evolution labeled at the top of each panel. *Left*: The shocked interface (dwarf disk) between supersonic inflows along the equator near the central BH. *Center*: Pileup of material and onset of the shock near the BH. *Right*: Thermalized disk surrounded by a shock. The black circle at the origin is the excised inner radial boundary of the domain.

2.2.3 Models evolved

Table 2.1 shows all of the models evolved and the key parameters being varied. Our baseline model 16TI_SFHo is the 16TI progenitor evolved with the SFHo EOS in GR1D, and thereafter evolved with FLASH using a viscosity parameter $\alpha = 0.03$.

The dependence on the viscosity parameter is explored with models 16TI_SFHo_α01 and 16TI_SFHo_α001, which use two additional values, $\alpha = \{0.1, 0.01\}$, respectively. The sensitivity of the outflow to the density structure at BH formation is studied with a model that uses the DD2 EOS in GR1D (16TI_DD2). Finally, we evolve the 350C progenitor with otherwise default parameters (model 350C_SFHo).

Simulations are evolved until a time t_{\max} after shock breakout from the surface of the star, and until the shock front pressure exceeds 150 dyn cm^{-2} at the edge of the domain. This timescale varies for each model, and is shown in in Table 2.1.

2.2.4 Outflow and shock analysis

Outflowing material is tallied by adding up unbound material over the computational domain at various times in the simulation. We use a positive Bernoulli parameter as a criterion to determine unbound status of a fluid element:

$$Be = \frac{1}{2}|\mathbf{v}|^2 + \epsilon + \frac{P}{\rho} + \Phi > 0, \quad (2.17)$$

where $\mathbf{v} = \mathbf{v}_p + v_\phi \hat{\phi}$ is the full three dimensional velocity. For reference, we assess the effect of using other unbinding criteria in Section 2.3.2.

We track the geometry of the shock that bounds the accretion disk as it evolves. Initially, the shock front is detected by looking for a relative jump in pressure in the interior of the star, which we quantify with a dimensionless pressure gradient parameter,

$$H_p = \frac{r}{P} \frac{\partial P}{\partial r}. \quad (2.18)$$

Further out radially, we use a velocity gradient parameter,

$$H_{|\mathbf{v}_p|} = \frac{r}{|\mathbf{v}_p|} \frac{\partial |\mathbf{v}_p|}{\partial r}. \quad (2.19)$$

Finally, towards the surface of the star, and in models where the post shock material is well mixed, we use a threshold in ^{56}Ni mass fraction ($X_{^{56}\text{Ni}} > 10^{-8}$). Otherwise, we use the dimensionless pressure gradient parameter. Each shock detection begins from a prescribed radius, searching radially inward and recording the first instance in which the appropriate criterion exceeds a prescribed threshold value.

We quantify the geometry of the shock front with a Legendre expansion (e.g., Fernández (2015))

$$r_s(\cos \theta, t) = \sum_{\ell} a_{\ell}(t) P_{\ell}(\cos \theta), \quad (2.20)$$

where r_s is the shock front radius at a given time for a given polar angle, P_{ℓ} are the Legendre polynomials, and $a_{\ell}(t)$ are the Legendre coefficients. We only consider the first three moments $\ell = \{0, 1, 2\}$, as they are the most informative regarding the evolution of the shock wave, with a_0 corresponding to the average shock radius, a_1 (dipole) describing the movement of the shock wave along the angular momentum (z -) axis, and a_2 (quadrupole) quantifying the relative extension in the polar versus equatorial direction.

2.3 Results

2.3.1 Overview of disk formation and evolution

Following BH formation, the stellar material accretes radially at supersonic speeds, with an increasing asymmetry between polar and equatorial regions due to centrifugal effects and the imposed angular dependence of j in the progenitor (Section 2.2.2). As the BH mass increases, the circularization radius approaches the point at which it crosses the ISCO radius (Figure 2.1), and a high density region forms along the equator of the star, perpendicular to the angular momentum vector (Figure 2.2, left panel). Supersonic inflows of material from above and below the equator collide and create a shocked interface called a *dwarf disk* (Beloborodov & Illarionov (2001); Lee & Ramirez-Ruiz (2006)), through which the flow still accretes supersonically into the

BH. In some cases, this structure persists beyond the point at which the circularization radius exceeds the ISCO radius (when the nuclear binding energy contributions to the EOS are included) as shown in Figure 2.1. Test simulations that ignore the nuclear binding energy and other source terms (i.e., adiabatic flow), skip an extended dwarf disk stage and form the shocked disk at the expected point.

Eventually, material piles up in the equatorial region at a sufficient rate to drive a shock out, inside which a thermalized accretion disk emerges on a timescale of ~ 10 ms (Figure 2.2, see also Mizuno et al. (2004a); Sekiguchi & Shibata (2007); Ott et al. (2011); Batta & Lee (2016)). The time at which this shocked bubble forms is marked in Figure 2.1 by a vertical line. Two low-density funnels remain initially along the rotation axis, as material with insufficient angular momentum plunges directly into the BH. Eventually, the shock expands to cover all latitudes, as shown in Figure 2.3.

Accretion to the BH decreases with time after shocked disk formation for the duration of the simulation, with large stochastic fluctuations in some models, as shown in Figure 2.4. Fluctuations are most clearly visible immediately after the formation of the shocked disk. Accretion is mediated by viscous angular momentum transport, with densities and temperatures high enough that neutrino emission and absorption become dynamically relevant. Over a timescale of ~ 1 s after disk formation in the `16TI_SFHo` model, viscous and nuclear energy injection in the disk are approximately balanced by neutrino cooling (Figure 2.4, bottom panel). This regime is referred to as Neutrino Dominated Accretion Flow (NDAF). As temperatures and densities drop in the disk as a result of the diminishing accretion rate, neutrino cooling drops off, and the energetics of the disk become dominated by viscous heating. This regime is referred to as Advection Dominated Accretion Flow (ADAF). The interior of the shocked cavity becomes highly turbulent, as shown in Figure 2.3.

Figure 2.5 shows the time evolution of the average shock radius after disk formation, for all models. Despite early oscillations, the size of the shocked disk increases monotonically with time over the duration of the simulation. The combination of

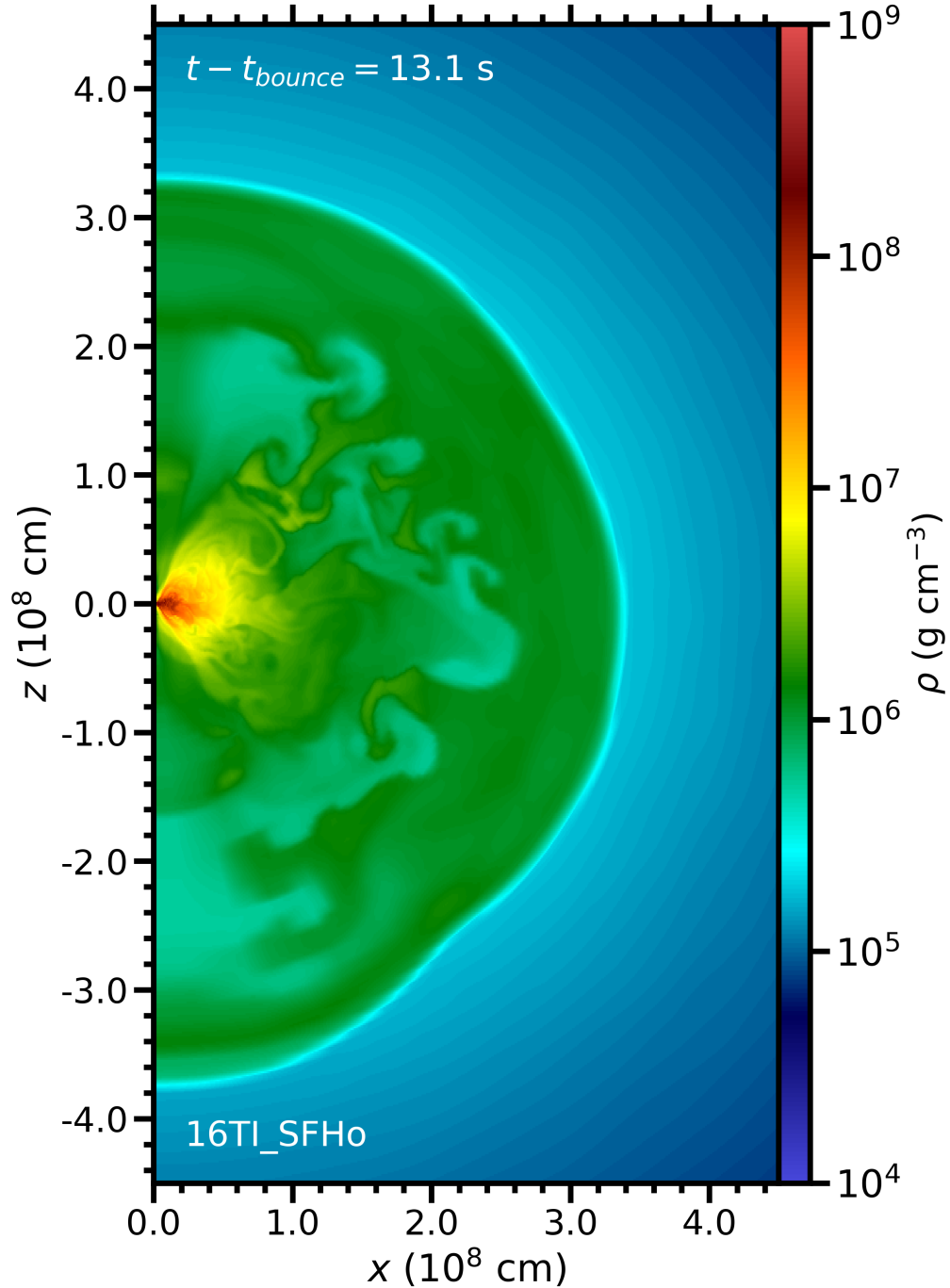


Figure 2.3: Snapshot of the density distribution for model 16TI_SFHo at ~ 13.1 s post bounce. At this point in the simulation the shocked disk has formed (11.1 s post bounce, Figure 2.2), and a dominance of viscous heating drives turbulence and a disk wind which, combined with the increasing specific angular momentum of accreted material, propels the shock out through the star. A slight north-south asymmetry and large-scale corrugation due to oscillations (Figure 2.6) are already visible. These deviations from sphericity become more apparent as oscillations freeze out and the shock propagates through the star.

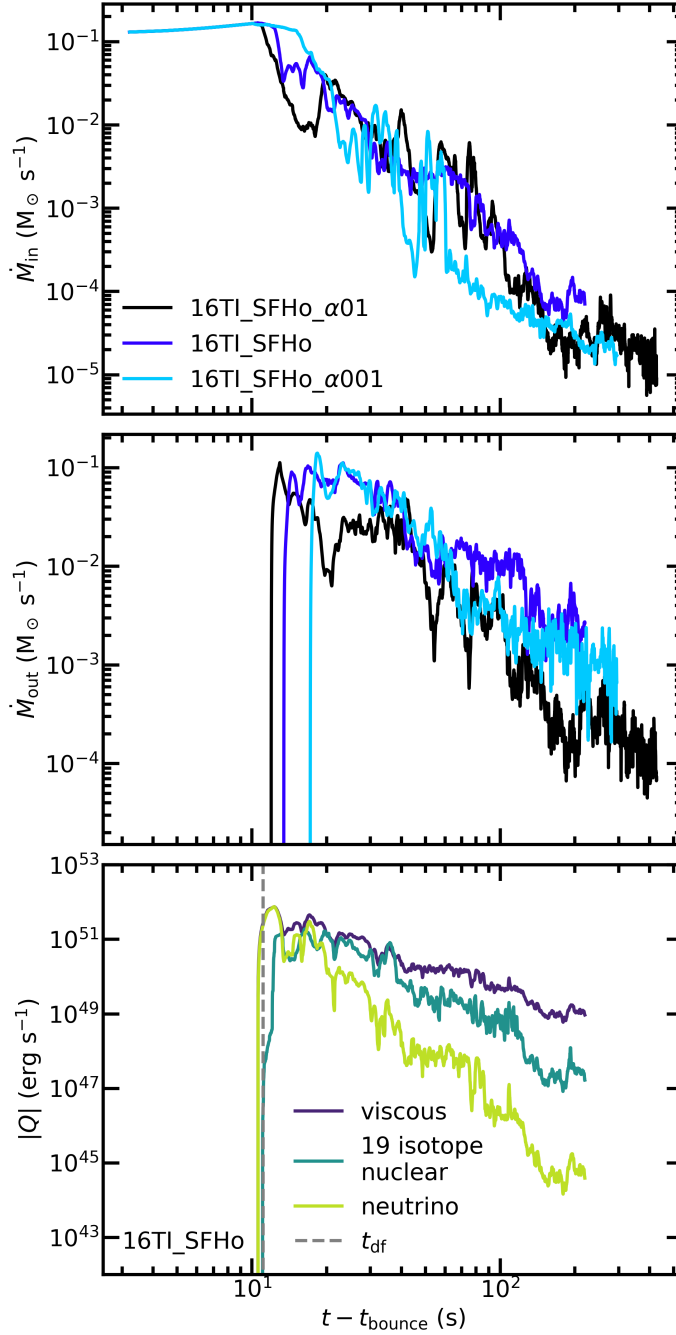


Figure 2.4: *Top:* Mass accretion rate across the inner radial boundary as a function of post-bounce time for selected models, as labelled. *Middle:* Mass outflow rate with positive Bernoulli parameter across an extraction radius $r_{\text{ej}} = 10^9$ cm, for the same set of models as the top panel. *Bottom:* Total viscous heating, nuclear heating, and net neutrino cooling rates inside the shock radius in model 16TI_SFHo, as labeled. The *19 isotope nuclear* curve shows the heating rate from the nuclear reaction network. Each curve has been smoothed with a moving average of width 0.5s. The vertical dashed line shows the time of shocked disk formation.

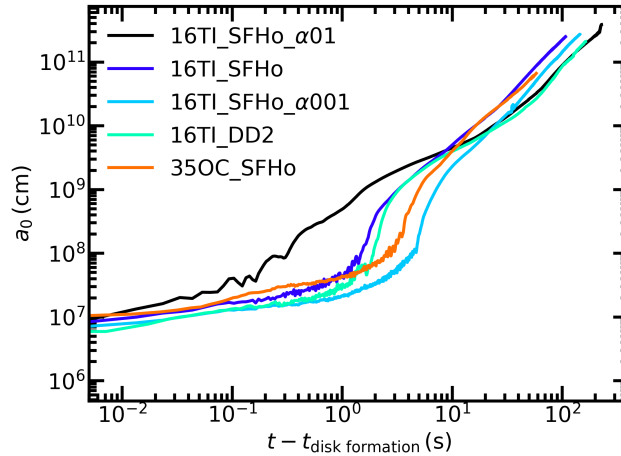


Figure 2.5: Evolution of the average shock radius (a_0) as a function of time after disk formation (Table 2.1), for all models, until shock breakout from the stellar surface.

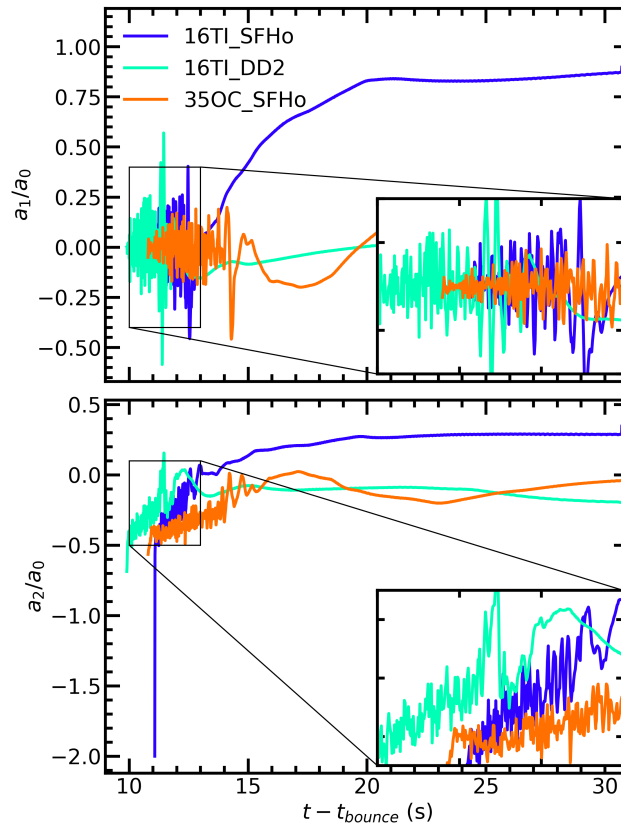


Figure 2.6: Evolution of the normalized dipole (top) and quadrupole (bottom) Legendre coefficients of the shock radius (Equation 2.20), for selected models. In most cases, the shock undergoes an initial oscillation phase before the geometry freezes, and continues to expand with little oscillation afterward. Each panel includes an inset which enlarges the time axis around the initial oscillation phase.

net heating and increasing specific angular momentum of accreted material cause the shock to accelerate its expansion outward through the star in the ADAF phase. While the diminishing accretion rate with time from the collapsing star facilitates shock expansion as time elapses, the dominance of viscous heating over neutrino cooling is the main driver of this rapid expansion once the ADAF phase sets in.¹ The evolution of the average shock radius is non-monotonic with the strength of viscous angular momentum transport. While the high-viscosity model `16TI_SFHo_α01` initially expands more rapidly than the baseline model, it eventually slows down its expansion rate and ends up having the longest breakout time (Table 2.1).

Most models exhibit large scale shock oscillations over a timescale of several seconds following disk formation, after which the shock starts to rapidly expand. The oscillations are quantified in Figure 2.6, which shows the time evolution (post-bounce) of the normalized dipole (a_1/a_0) and quadrupole (a_2/a_0) moments of the shock surface (Equation 2.20). Similar non-axisymmetric (spiral) shock oscillations were also reported by Gottlieb et al. (2022) in 3D GRMHD simulations without neutrino cooling or nuclear energy changes. Accretion shocks around BHs are known to be unstable to non-axisymmetric modes in both the isothermal and adiabatic limits (Molteni et al. (1999); Gu & Foglizzo (2003); Gu & Lu (2006); Nagakura & Yamada (2008, 2009)), although the stability properties with internal energy source terms are less well studied than in the NS case (e.g., Foglizzo et al. (2007)).

In our models, the axisymmetric oscillations are concurrent with the NDAF phase. After the transition to the ADAF phase, rapid expansion starts, and oscillations stop. The high viscosity model `16TI_SFHo_α01` skips the NDAF phase altogether, showing fewer early oscillations than the other models, with the shock expanding rapidly

¹The shock that encloses the collapsar accretion disk is qualitatively different from that in slowly-rotating core-collapse SNe, in which thermalization of accreting matter is offset by neutrino cooling and nuclear dissociation, leading to a stalled shock that responds sensitively to sudden changes in the accretion rate. In core-collapse SNe, the cooling layer is supported by the protoneutron star and can thus remain at high densities for a long time, while in collapsars, significant disk cooling occurs only as long as the disk remains dense and hot enough.

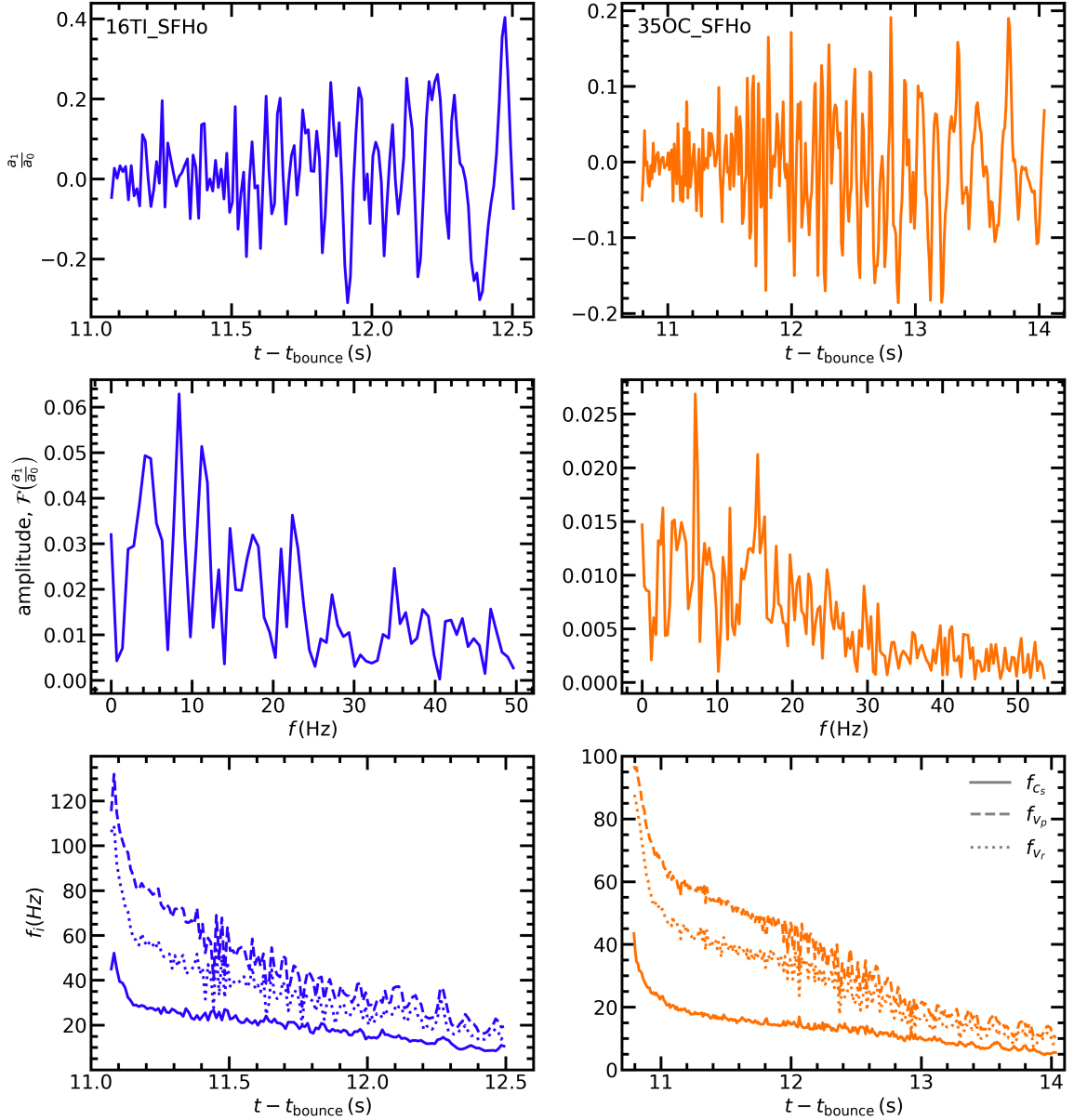


Figure 2.7: Frequency analysis of initial shock oscillations. Data extends from the time of disk formation until the spherical harmonic coefficient begins to asymptote and the shock shape freezes. Left and right columns show data from different models, as labeled. *Top*: Evolution of the Legendre coefficient a_1 normalized by the average shock radius a_0 . *Middle*: Amplitude (absolute value) of the Fourier transform $\mathcal{F}(a_1/a_0)$ of the normalized $\ell = 1$ time series. *Bottom*: Characteristic frequencies $f_i = v_i/a_0$ calculated using the average sound speed ($v_i = c_s$), poloidal speed ($v_i = v_p$), and radial speed from behind the shock front ($v_i = v_r$), as labeled.

immediately after disk formation.

In models such as `16TI_SFHo`, the shock bubble expands asymmetrically after a preferred polar direction is set once the disk oscillations freeze out (Figure 2.6). In other cases, such as the high-viscosity model `16TI_SFHo_α01`, the shock expands roughly isotropically, with a slight predominance of the equatorial direction, reaching the surface with a slight extension to one pole. We surmise that the asymptotic shock morphology arises as a combination of random oscillations frozen out as the disk becomes advective, the existence and strength of these oscillations given the balance of viscous heating versus neutrino cooling, and the imposed angular dependence of the rotation profile in the star ($j \propto \sin^2 \theta$), which results in an effective gravity that varies with angle and is weakest at the equator.

In Figure 2.7 we show initial $\ell = 1$ shock oscillations and its temporal Fourier spectrum for models `16TI_SFHo` and `350C_SFHo` over 1 – 3 s after shock formation, along with the characteristic frequencies $f_i = v_i/a_0$ associated with the shock crossing time at various speeds v_i (sound speed, average poloidal speed, and average radial speed). The Fourier amplitudes of model `16TI_SFHo` show a broad peak around 10 Hz, with power extending to 50 Hz. This range is consistent with that covered by the characteristic frequencies f_i , which decrease with time as the shock cavity expands. A qualitatively similar result is obtained for model `350C_SFHo`, but with shock oscillations occurring at overall higher frequencies than in model `16TI_SFHo`. We leave for future work a more thorough analysis of possible correlations between shock oscillations and temporal fluctuations in the neutrino luminosity, as well as with gravitational wave emission.

Once oscillations freeze out, the shock expands through the remainder of the star with approximately constant shape. The post-bounce timescales for black hole formation, thermalized disk formation, and shock breakout from the stellar surface are listed in Table 2.1.

Table 2.2: Bulk outflow properties, obtained by integrating unbound material at the end of the simulation. Columns from left to right show model name, ejecta mass, ejecta kinetic energy at the end of the simulation, asymptotic ejecta kinetic energy (Equation 2.22), mass-weighted average expansion velocity at infinity (Equations 2.21, 2.23), minimum electron fraction of outflowing material, ^{56}Ni mass ejected, and SN light curve peak time (Equation 2.24, (Arnett, 1982)).

Model	M_{ej} (M_{\odot})	K_{ej} (10^{51} ergs)	K_{∞} (10^{51} ergs)	$\langle v_{\infty} \rangle$ (10^3 km/s)	$Y_{\text{e,min}}(t_{\text{max}})$	$M^{56\text{Ni}}$ (M_{\odot})	t_{peak} (days)
16TI_SFHo	8.19	9.07	9.20	8.7	0.498	1.28	44.7
16TI_SFHo_α01	8.97	2.39	2.41	4.8	0.499	0.29	63.1
16TI_SFHo_α001	7.93	4.34	4.37	6.0	0.481	0.81	52.9
16TI_DD2	9.17	3.67	3.70	5.6	0.500	0.63	59.2
350C_SFHo	15.1	9.45	10.6	7.7	0.497	1.39	64.3

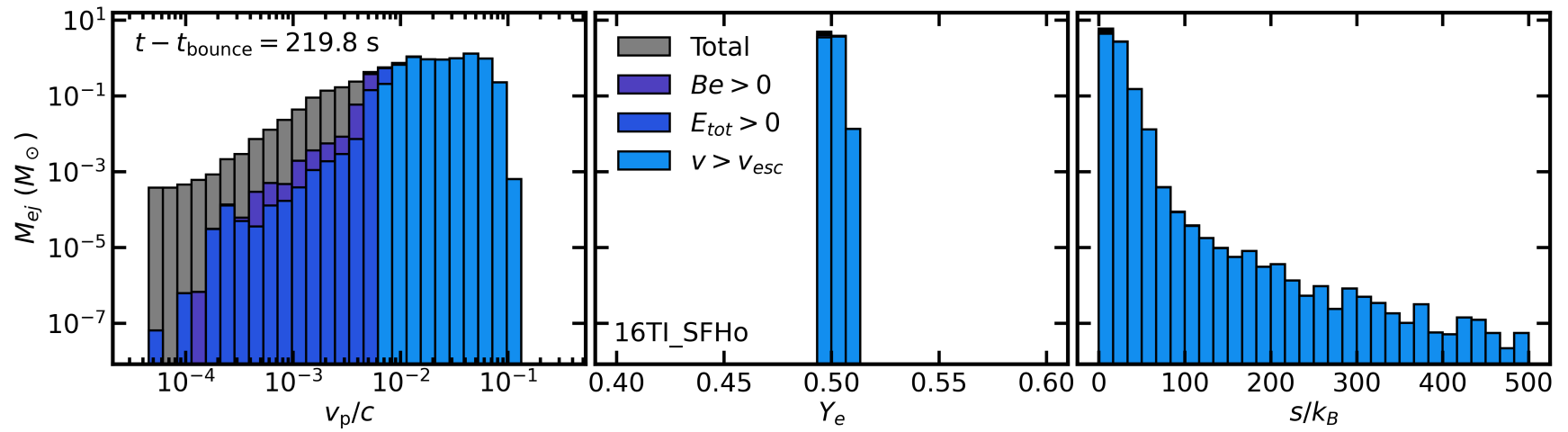


Figure 2.8: Mass histograms of the outflow at the end of the simulation for model 16TI_SFHo, binned by poloidal velocity (left), electron fraction (center), and entropy per baryon (right). Different colours represent the gravitational binding criterion used, as labeled (*Total* represents both bound and unbound matter).

2.3.2 Outflow properties

Bulk properties of the disk outflow, obtained by integrating over unbound material at the end of the simulation, are shown in Table 2.2 for all models. The total ejecta mass has a monotonic dependence on the strength of viscous angular momentum transport, with stronger viscosity leading to more ejected mass. The ejecta kinetic energy at the end of the simulation K_{ej} , on the other hand, shows non-monotonic behavior, with a maximum for the baseline model 16TI_SFHo and the lowest value for the high-viscosity case. Using the DD2 EOS before BH formation results in a slightly higher ejecta mass than the baseline model, but with kinetic energy lower by a factor ~ 2.5 . Changing the progenitor model to 350C results in a similar kinetic energy but almost double the ejecta mass than the baseline 16TI model.

Figure 2.8 shows the poloidal velocity, electron fraction, and entropy distributions of unbound material (section 2.2.4) at the end of the simulation for model 16TI_SFHo, using different binding criteria: total speed exceeding the escape speed v_{esc} , positive total specific energy E_{tot} , positive Bernoulli parameter (Eq. 2.17), and total ejecta (bound and unbound). The fastest ejecta ($v_p \gtrsim 0.006 c$) is unbound by kinetic energy alone, with a total mass of $7.2 M_{\odot}$. The remaining, slower ejecta has a significant internal energy component that contributes to its unbinding and which can be transformed into kinetic energy upon further expansion. The vast majority ($\sim 92\%$) of material ejected by the 16TI_SFHo model is unbound at the end of the simulation, according to the Bernoulli criterion. The ejecta velocity has a sharp cutoff at $\sim 0.2 c$, consistent with BH accretion disks evolved in viscous hydrodynamics around NS merger remnants (e.g., Fernández et al. (2023a)). The low velocity tail extends to $\sim 5 \times 10^{-5} c$.

The entropy distribution decays with increasing entropy, with a tail reaching several hundred k_B per baryon. The fastest material that satisfies the escape velocity criterion dominates the distribution above $20 - 30 k_B$, with slower ejecta contributing

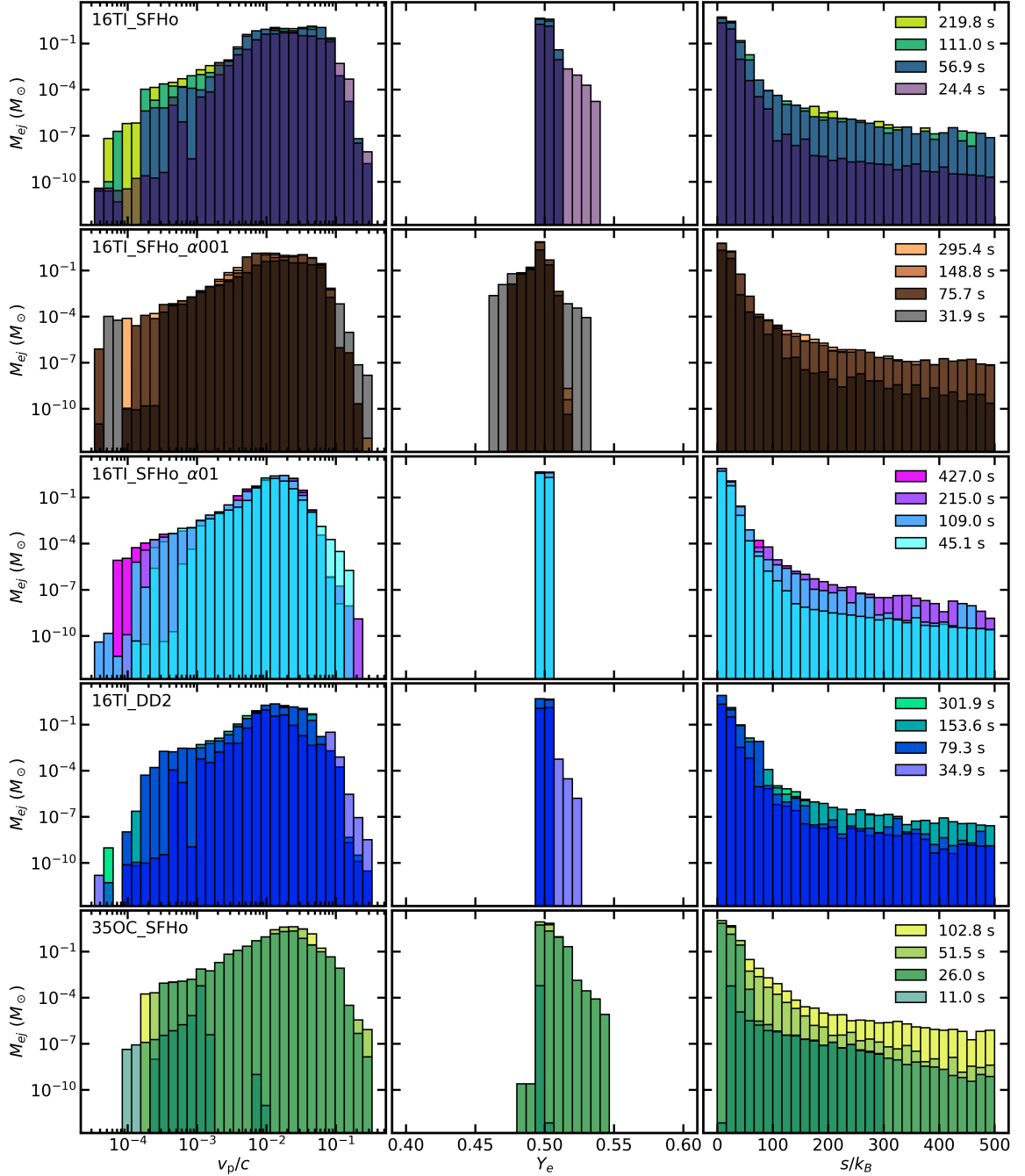


Figure 2.9: Unbound mass histograms at various post-bounce times in each simulation, as labeled. Only material with positive Bernoulli parameter (Equation 2.17) and $v_r > 0$ is considered. Columns from left to right show histograms binned by poloidal velocity (left), electron fraction (center), and entropy per baryon (right).

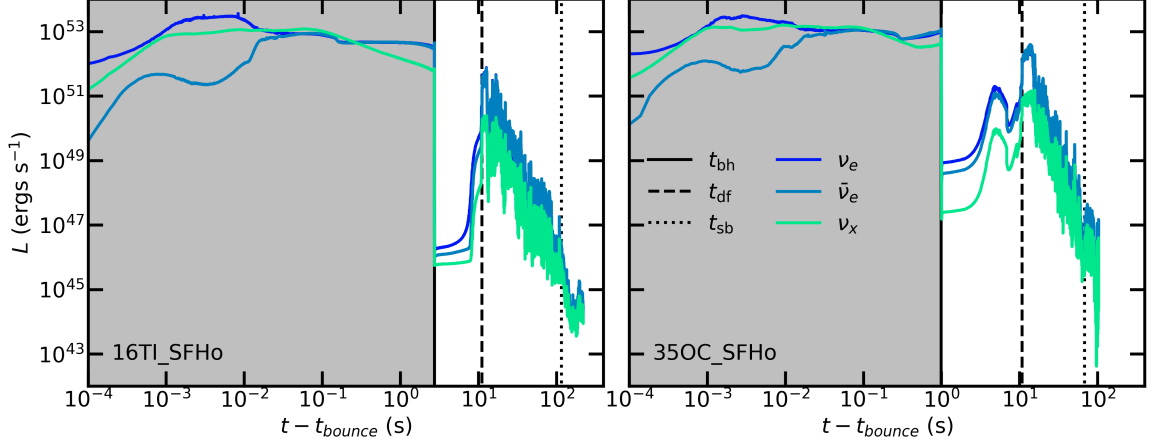


Figure 2.10: Neutrino luminosities of ν_e [blue], $\bar{\nu}_e$ [teal], and ν_x [all heavy lepton species, green] as a function of post bounce time for selected models, as labeled. The vertical lines indicate the time of BH formation t_{bh} (solid black), shocked disk formation t_{df} (dashed black), and shock breakout from the star t_{sb} (dotted black). The shaded grey and white regions correspond to the GR1D and FLASH portion of the evolution, respectively.

mostly to the lowest entropy bin. Similar entropy distributions are obtained in viscous hydrodynamic simulations of BH accretion disks formed in NS mergers, which produce most of their ejecta in the ADAF phase, driven by viscous heating and nuclear recombination (e.g., Fernández et al. (2023a)).

The electron fraction distribution of our collapsar outflows is much narrower than that obtained in NS merger disk outflows. It has a peak at $Y_e \sim 0.5$, extending from $Y_e \sim 0.49$ on the low end, up to $Y_e \sim 0.51$ on the upper edge by the end of the simulation, with deviations from this general shape reflecting the degree to which neutrino interactions can neutronize disk material and possibly drive the r -process. There is no significant difference in Y_e between ejecta components with a different degree of gravitational binding, with more bound material contributing primarily with $Y_e \sim 0.49$.

The mass outflow rate at $r = 10^9$ cm for selected models is shown in Figure 2.4. Curves follow a similar power-law decay structure with qualitatively similar peaks and dips as the mass accretion rate, shifted in time due to the interval needed for the

ejecta to reach $r = 10^9$ cm.

Unbound mass histograms are shown in Figure 2.9 for all models, considering only matter with positive Bernoulli parameter as well as $v_r > 0$, and at several post-bounce times in the simulation. Histograms have the same overall morphology as in Figure 2.8.

The electron fraction histograms are narrow in all cases, with variations between models limited to the interval $0.45 \lesssim Y_e \lesssim 0.55$. In models 16TI_SFHo, 16TI_SFHo- α 001, and 16TI_DD2, the electron fraction distribution becomes narrower with time as neutrino luminosities drop off. The minimum electron fraction in the ejecta at the end of the simulation for each model $Y_{e,\min}$ is shown in Table 2.2. While there is a monotonic increase in minimum Y_e with increasing viscosity, the variation in this quantity is less than 4% for the viscosities used.

In each model, late-time ejecta contributes significantly to the high entropy tail of the distribution. During this time, the viscous heating rate drops 2 orders of magnitude while the peak density drops 5 orders of magnitude, leading to higher entropy ejecta at late times.

The velocity distribution is broadly similar between models, with some variation at the low-velocity end.

2.3.3 Dependence of Disk Evolution on EOS and Progenitor Model

The BH formation time relative to the bounce time in model 16TI_DD2 is ~ 2.5 s longer than in model 16TI_SFHo, as expected for a stiffer EOS. The longer evolution time implies that the outer stellar layers at the same Lagrangian mass coordinate have collapsed to a deeper radius in model 16TI_DD2 than in 16TI_SFHo, with the disk forming at an earlier time post-bounce. Both 16TI_SFHo and 16TI_DD2 go through an NDAF phase and exhibit early shock oscillations, before viscous heating becomes dominant and shock expansion ensues. The average shock radius in model 16TI_DD2

starts out smaller than in the baseline model (Figure 2.5), but upon transition to the ADAF phase, the shock in model 16TI_DD2 accelerates to match the position of that from 16TI_SFHo, eventually falling behind, having a lower kinetic energy and longer breakout time (Table 2.1). This difference in evolution can be traced back to the longer post bounce time to BH formation in model 16TI_DD2. The presupernova star has two prominent discontinuities in the angular momentum profile, corresponding to the lower and upper edges of the silicon burning shell outside the iron core. During the GR1D evolution, the angular momentum profile is stretched radially as the star collapses, with the outermost discontinuity becoming a broad dip in the angular momentum profile at $\sim 10^8 - 10^9$ cm in the 16TI_SFHo model. Due to the longer collapse time of the 16TI_DD2 model, the dip in angular momentum is flattened out. This results in a lower mass accretion rate at late times ($\sim 70 - 130$ s) in model 16TI_DD2 due to the higher angular momentum of material being added to the disk, reducing the energy injection by the disk wind, and ultimately delaying shock breakout from the surface of the star.

In model 350C_SFHo the progenitor star is much more massive at the end of its life (for 350C, a mass: $28.1 M_{\odot}$, for 16TI: $13.9 M_{\odot}$) than the fiducial progenitor, while being smaller in size and thus much more compact (for 350C, a radius: 1.6×10^{11} cm, for 16TI: 7.3×10^{11} cm). The evolution of model 350C_SFHo is faster than the fiducial model, with BH formation, disk formation, and shock breakout occurring on shorter timescales. Due to the high accretion rate in model 350C_SFHo, we need to move the inner radial bound several times before thermalized disk formation slows down the BH accretion rate. This model exhibits similar early oscillations of the shock before the onset of rapid expansion to the fiducial model. Notably, in predicting the Lagrangian mass coordinate for accretion disk formation, the circularization radius $r_{\text{circ,A}}$ exceeds the ISCO of the BH at two points (Figure 2.1), with the disk formation point we obtain being consistent with the second crossing. This pattern appears in the neutrino luminosity (Figure 2.10) as a bump before thermalization of the dwarf

disk. Model 350C_SFHo produces significantly more ejecta than the fiducial model, but with comparable kinetic energy.

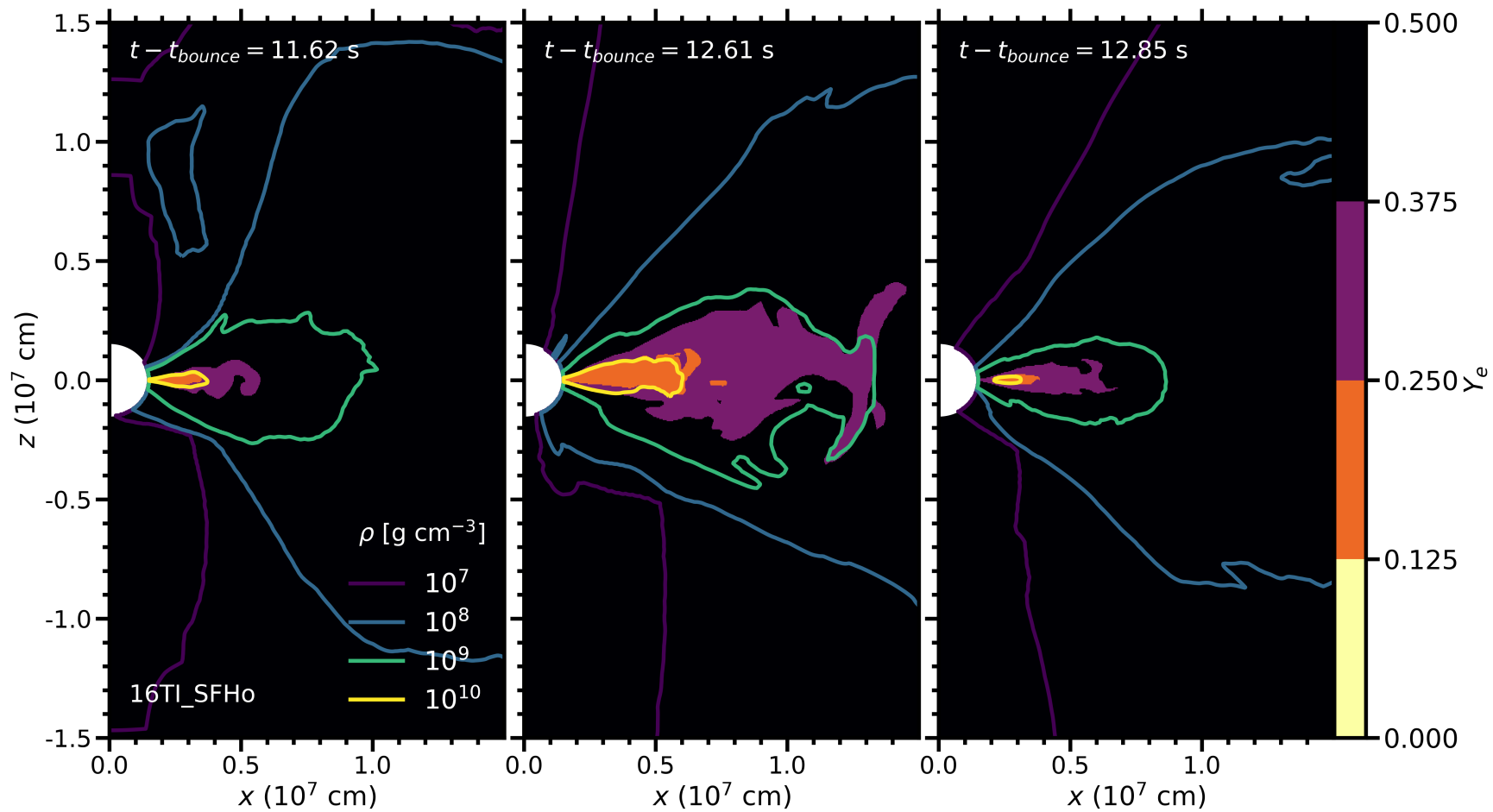


Figure 2.11: Snapshots of the electron fraction within the inner disk in model 16TI_SFHo around the time of maximum neutrino emission (c.f. Fig. 2.10), with overlaid density contours, as labeled.

2.3.4 Neutrino emission and neutronization

After the formation of the shocked disk, densities and temperatures are high enough for charged-current weak interactions to become important in cooling the disk and changing its composition. In particular, since material from the collapsing star has $Y_e \simeq 0.5$, any path to r -process nucleosynthesis requires a significant amount of electron-type neutrino/antineutrino emission and absorption, in order to increase the ratio of neutrons to protons toward its neutron-rich equilibrium value for a disk with partially-degenerate electrons.

Figure 2.10 shows total neutrino luminosities of ν_e , $\bar{\nu}_e$, and ν_x (which represents all heavy lepton species) for selected models. During the protoneutron star phase, luminosities rise steeply following shock breakout from the neutrinosphere, thereafter decreasing more gradually (factor of ~ 5), followed by a sharp drop as the NS collapses to a BH.

As material from the infalling star accretes onto the BH, densities and temperatures gradually increase toward the equatorial plane due to centrifugal effects, leading to a slow increase in luminosities. As the dwarf disk forms (Figure 2.2), luminosities of all flavors accelerate their rise. Formation of the thermalized disk marks a sharp increase in luminosities due to the higher densities and temperatures.

This delay time between the sharp drop in neutrino luminosities at BH formation (t_{bh} in Figure 2.10) and the spike shortly after shocked disk formation (t_{df}) depends on the angular momentum profile of the star, and can be a useful observational diagnostic of the rotational profile of collapsar progenitors. The luminosity maximum after thermalized disk formation depends on the thermodynamics of the disk when it forms, which in turn depends on the compactness of the star M/R and on the accretion rate \dot{M}_{acc} . After reaching a peak, luminosities decay as a power law in time. This decay is related to the difference between the accretion rate onto the BH (which depends on the angular momentum transport rate in the disk) and the rate

at which mass crosses the shock and feeds the disk, which ultimately depends on the radial dependence of density and angular momentum of the star.

Detecting these observational signatures in neutrinos would require a galactic collapsar, with current capabilities. This is unfortunately limited by the galactic collapsar rate of ~ 1 per 10^4 years (e.g., Graur et al. (2017)).

The lack of neutron-rich material in the outflow (Fig. 2.9) could be seen to be at odds with the substantial neutrino emission produced by all models (Figure 2.10). The answer is provided in Figure 2.11, which shows the electron fraction in the inner accretion disk for our baseline model, around the time of peak neutrino emission. Over a timescale of ~ 1 s around the maximum in neutrino emission, material in the densest regions of the accretion disk neutronizes to $Y_e < 0.25$. The vast majority of this material is fully accreted onto the BH, however, and does not contribute to the outflow except possibly through trace amounts mixed into the shock cavity. As accretion continues and the density in the disk drops, neutrino emission decreases from its maximum and so does the degree of neutronization, with the electron fraction remaining closer to $Y_e \sim 0.5$ as the accretion disk is continually fed by infalling stellar material. By the time shock expansion accelerates in the ADAF phase, giving rise to an outflow, there is negligible neutronization of post-shock material.

2.3.5 An engine for type Ic-BL supernovae?

In order to explain type Ic-BL SNe with the collapsar disk outflow alone, not only does the explosion need to be successful – shock breaking out of the stellar surface with enough energy – but also sufficient ^{56}Ni must be produced in order to power the light curve over a timescale of months (MacFadyen, 2003). The average ^{56}Ni mass for a sample of type Ic-BL was found to be $0.32M_\odot$ by Lyman et al. (2016) through bolometric light curve fits, although values can be as high as $0.7M_\odot$ (e.g., for SN 1998bw Iwamoto et al. (1998); Woosley et al. (1999)), and low- ^{56}Ni mass events could be missed due to selection effects (Ouchi et al., 2021). An analysis of a large

sample of type Ic-BL SN spectra by Modjaz et al. (2016) found mean line width velocities in the range $13,000 - 21,000 \text{ km s}^{-1}$ ($0.04 - 0.07 c$), depending on whether the SN was accompanied by a GRB, and the epoch at which it was measured.

To assess the plausibility of our collapsar disk outflows as engines of these SNe, we integrate unbound outflowing ^{56}Ni (obtained from the 19-isotope network and NSE solver) at the end of the simulation. Table 2.2 lists nickel masses as well as total ejecta masses. All models produce sufficient ^{56}Ni to power a generic type Ic-BL SN light curve, with variation in ^{56}Ni yield between models spanning a factor of ~ 4 .

We obtain the asymptotic expansion velocity v_∞ at infinity by equating the asymptotic kinetic energy per unit mass to the Bernoulli parameter, which implies full conversion of internal energy to kinetic energy through adiabatic expansion of unbound material, with no additional energy sources:

$$\frac{1}{2}v_\infty^2 = \max(Be, 0), \quad (2.21)$$

where Be is given by Equation (2.17). We then compute an asymptotic ejecta kinetic energy as

$$K_\infty = \int \frac{1}{2}v_\infty^2 dM_{\text{ej}}. \quad (2.22)$$

The ejecta-mass-weighted average velocity of unbound material is defined as

$$\langle v_\infty \rangle = \frac{\int v_\infty dM_{\text{ej}}}{\int dM_{\text{ej}}}, \quad (2.23)$$

where, as implied by Equation (2.21), the integral is carried out over all cells that satisfy $Be > 0$.

Table 2.2 shows that the average outflow velocity in the ejecta from our simulations is systematically lower, by a factor of at least ~ 2 , than what is inferred from the spectra of type Ic-BL supernovae. Note however that our asymptotic ejecta kinetic energies K_∞ are consistent with the range inferred for this SN subclass (Lyman et al., 2016), thus the lower average velocities can be a consequence of the larger ejecta masses we find (by a factor $2 - 3$) compared to the average value for type Ic-BL SNe.

For reference, we also estimate the peak time for a SN light curve using (Arnett, 1982)

$$t_{\text{peak}} = \left(\frac{3}{4\pi} \frac{\kappa M_{\text{ej}}}{\langle v_{\infty} \rangle c} \right)^{1/2}. \quad (2.24)$$

assuming an opacity of $\kappa = 0.1 \text{ cm}^2 \text{ g}^{-1}$. Table 2.2 shows the resulting rise times. The larger ejecta masses and lower asymptotic velocities drives the peak time toward higher values than what would be obtained with average values for the Ic-BL class.

2.3.6 Comparison to recent work

While multi-dimensional global collapsar simulations have a long history (Bodenheimer & Woosley (1983); MacFadyen & Woosley (1999); Proga et al. (2003); Mizuno et al. (2004a,b); Fujimoto et al. (2006); Nagataki et al. (2007); Sekiguchi & Shibata (2007); Harikae et al. (2009, 2010); Lopez-Camara et al. (2009); López-Cámara et al. (2010); Ott et al. (2011); Sekiguchi et al. (2011); Batta & Lee (2016); Obergaulinger & Aloy (2017); Nagataki (2018); Aloy & Obergaulinger (2021); Gottlieb et al. (2022); Janiuk et al. (2023); Shibata et al. (2023); Crosato Menegazzi et al. (2023)), only recently have models been developed which simultaneously include (1) global star collapse with self-consistent disk formation and subsequent accretion and outflow, (2) angular momentum transport, and (3) neutrino emission and absorption with appropriate microphysics and evolution of Y_e (Just et al. (2022a); Fujibayashi et al. (2023a,b)), thus we focus our comparative discussion on these recent studies.

Just et al. (2022a) use Newtonian hydrodynamics with a pseudo-Newtonian BH, the same components of the viscous stress tensor with similar viscosity strengths, and the 16TI progenitor. The two main qualitative differences with our models are their use of an energy dependent M1 neutrino transport (whereas we use a gray leakage scheme with lightbulb absorption), and the initial condition for the simulations, which are set up by placing a BH at the center of the star at the time of core bounce (whereas we evolve with GR1D until BH formation). In addition, they do not include the energy input from a nuclear reaction network.

Disk formation occurs $\sim 1 - 2$ s earlier in our simulations than in the corresponding models of Just et al. (2022a), likely stemming from the difference in initial condition. Figure 2.1 predicts disk formation at Lagrangian enclosed mass of $\sim 3.2M_{\odot}$ for the 16TI progenitor and the SFHo EOS, whereas Just et al. (2022a) predicts BH formation at $\sim 3.8M_{\odot}$. Similarly our BH masses at disk formation are $\sim 0.3M_{\odot}$ lower. We see the same dependence of $Y_{e,\min}$ in the ejecta with increasing viscosity, pushing the minimum electron fraction towards $Y_e = 0.5$. We also see the same monotonic decrease in final black hole masses with increasing viscosity, but with our values being $\sim 0.5 - 1M_{\odot}$ lower. Like Just et al. (2022a), we see the monotonic relationship of the NDAF phase duration with viscosity, before advection and viscous heating become dominant during the ADAF phase (the intermediate viscosity value resulting in the shortest NDAF phase, the low viscosity model having the longest NDAF phase, and the high viscosity model immediately starting in the ADAF phase). We find (non-monotonic) explosion energies consistent with those of Just et al. (2022a).

Notably, Just et al. (2022a) also finds a non-monotonicity in the shock breakout time with viscosity: their intermediate viscosity run is the fastest, followed by the high-, and finally low viscosity, whereas we find that the intermediate viscosity is fastest, followed by low- and finally high viscosity. Unlike Just et al. (2022a), however, the geometry of our shock waves at the time of shock breakout in the low- and intermediate viscosity models are extended to one pole, while the high viscosity model is more spherical. Instead, Just et al. (2022a) find that the low- and intermediate viscosity runs are nearly spherical, while the high viscosity model is equatorially extended.

A comparison study of viscous hydrodynamic evolution of NS merger accretion disks (Fernández et al., 2023b) has shown that M1 transport results in more efficient cooling than the leakage scheme used in our FLASH setup, which depends on the adopted local prescription for the optical depth. This inefficient cooling is also evident when comparing our scheme with time-independent Monte Carlo transport on simu-

lation snapshots (Fahlman & Fernández, 2022a). While this inefficient cooling can in principle affect neutronization of the disk, our overall agreement with the results of Just et al. (2022a) shows that for viscous hydrodynamic evolution, for which outflow occurs in the ADAF phase, neutrino transport differences are not consequential for the occurrence of the r -process in the outflow, and play a sub-dominant role in mass ejection.

Fujibayashi et al. (2023a) evolves the collapse of several rotating helium and Wolf-Rayet progenitor stars in axisymmetric numerical relativity, using M1 neutrino radiation transport, and a turbulent length scale to parameterize the strength of viscosity. While their progenitors are not directly comparable to ours, they start from a pre-collapse progenitor, and follow the evolution to bounce and BH formation before forming the disk. They also find insufficient neutronization to support the production of r -process elements in all their models. The entropy distribution of the ejecta extends to several hundred k_B , like in our models. Despite the differing progenitor models, we find similar disk outflow energies, while our ejecta masses are larger by a factor of several. This is likely due to the shorter duration of their models, and the use of an extraction surface instead of integrating over the entire domain at the end of the simulation (thus not accounting for mass outside the extraction threshold that may become unbound after crossing it). As a result of these smaller ejecta masses, the estimated supernova light curve rise time is shorter than those we estimate here, by a factor of a few.

Models from Fujibayashi et al. (2023a) are broken down into two qualitative groups, according to their evolution. First, those that have a higher infall rate at the time of disk formation, which undergo a NDAF phase before viscous heating becomes dominant over neutrino cooling, and evolve in a qualitatively similar way to our low- and intermediate viscosity models. Models with lower infall rate at the disk formation time are such that viscous heating dominates over neutrino cooling over the entire disk expansion. This is qualitatively similar to our high viscosity model.

Fujibayashi et al. (2023b) follows the disk outflow in three different progenitor stars with high core compactness, varying viscosity, rotation rate, and resolution, among other parameters, and using the same method as Fujibayashi et al. (2023a) but now placing a BH at the center of the star at the time of core bounce. Models are run for values of $\alpha = 0.03, 0.06, 0.10$. Like our high viscosity case, their high- α run proceeds with no NDAF phase, leading to the outflow starting a short time after disk formation. Their low viscosity run evolves in a qualitatively similar way to our low and intermediate viscosity models, where the explosion is initially delayed due to the presence of an NDAF phase. While the models they run are not directly comparable to ours, we find the same monotonic increase in ejecta mass with increasing viscosity. It is unclear if they see the same non-monotonicity in shock breakout time with viscosity, since their models are run for only $\lesssim 20$ s of simulation time.

2.4 Summary and Discussion

We have studied the long-term outflows from accretion disks formed in rotating Wolf-Rayet stars undergoing core collapse. We evolve the progenitor from core-collapse to BH formation in spherical symmetry using GR1D (Figure 2.1), and thereafter in axisymmetry using FLASH. A shocked, centrifugally-supported disk emerges self-consistently in our simulations (Figures 2.2-2.3), and is subject to angular momentum transport via shear viscosity, and heating/cooling due to viscosity, neutrino emission and absorption, and nuclear energy release (Figure 2.4). Unbound mass is ejected from the disk once it enters an ADAF stage with sub-dominant neutrino cooling. Our main results are the following:

1. – In all of our models, the disk outflow is capable of driving the shock to breakout from the surface of the star, resulting in an explosion (Figure 2.5). While this qualitative result is the same in all our models, the detailed properties of the disk evolution and ejecta depend on the strength of viscous angular momentum transport, on the

progenitor star, and on the nuclear EOS used in the evolution to BH formation with GR1D (Tables 2.1 and 2.2).

2. – We find that all models produce sufficient ^{56}Ni to power a type Ic-BL SN light curve. However, the average asymptotic velocity of the ejecta is too slow, by a factor of $\sim 2-3$ relative to what is needed to account for type Ic-BL SN spectra (Table 2.2). The total kinetic energies of our outflows are in the right range, but our ejecta masses are too high compared to what is inferred from Ic-BL light curves.

3. – We find insufficient neutronization of the ejected material to support the production of heavy r -process elements (Figure 2.9). While significant neutronization does occur in the disk (Figure 2.11), the neutron-rich material is accreted to the BH and not ejected.

4. – Neutrino luminosities exhibit a drop of many orders of magnitude at BH formation, followed by a subsequent rise and peak when the disk thermalizes (Figure 2.10). The duration of the gap in neutrino emission and the magnitude of the peak after disk formation, are dependent on the stellar compactness, accretion rate, and angular momentum profile of the progenitor. This is a diagnostic observable of massive star interiors, should a galactic collapsar occur.

5. – In some models the newly formed shocked disk exhibits oscillations during the NDAF phase (Figure 2.6). The oscillation frequencies are consistent with characteristic frequencies of the cavity (inverse of sound crossing time and advection time; Figure 2.7). After an oscillatory phase lasting a few seconds, the shock geometry freezes as it begins to expand more rapidly. Generally, the shock waves are extended in one of the polar directions at shock breakout, with the highest viscosity model having a more spherical shape than the others.

The degree of neutronization of the ejecta depends on the importance of neutrino emission and absorption, which in turn depends on the thermodynamics of the disk. How close to the BH the disk forms and how dense it gets depends on the circularization radius (equation 2.2), which in turn depends on the BH mass, the angular momentum profile of the star, and on the accretion rate, which depends on the density profile of the progenitor (or alternatively, the core compactness of the progenitor). A star with a high core compactness, as well as with density and rotation profiles that decrease slowly with radius would maximize neutronization in the disk. Here we have restricted ourselves to long GRB progenitors that have previously been used in collapsar studies, exploring other progenitors and rotation profiles is left for future work.

Progenitor variation aside, however, we find here that rapid expansion of the shock only begins once the disk has transitioned to an ADAF phase, due to the decreasing density in the disk, which implies that mass ejection is tied to the end of neutronization. Just et al. (2022a) evolves a collapsar disk with no viscosity, finding that while it remains in the NDAF phase for its entire evolution and it supports a neutrino-driven wind, it does not eject any significant amounts of neutron-rich material either. Thus, *ejection of matter that can support the r-process might not be possible if the mass ejection mechanism is thermal* (relying on viscous heating without neutrino cooling, in our case, or on neutrino heating in the inviscid model of Just et al. (2022a)). Inclusion of magnetohydrodynamics could overcome this hurdle, as material ejected mechanically via Lorentz force from the neutronized disk can bypass the requirement of reaching an ADAF phase for mass ejection (as is the case in NS merger disks evolved in MHD, which significantly increase the amount of neutron-rich ejecta relative to that obtained with viscous hydrodynamics; e.g. Siegel & Metzger (2018); Fernández et al. (2019c); Just et al. (2022b); Hayashi et al. (2022); Curtis et al. (2023b)). The question of neutrino absorption raising Y_e from its neutronized equi-

librium value would still remain, however (e.g., Miller et al. (2020)). Thus, global, long-term MHD simulations of collapsar disk outflows with good neutrino radiation transport are needed to definitively answer the question of whether collapsars can be a relevant r -process site.

The entropy per baryon of ejected material spans a broad distribution, with a high entropy tail arising at later times in the simulation reaching several hundred k_B per baryon or more. A small fraction of the ejecta could therefore (possibly) produce light r -process elements in the high-entropy regime, similar to the conditions in the neutrino-driven winds of some CCSNe models (e.g., Wanajo et al. (2018); Witt et al. (2021); Wang & Burrows (2023)).

The low asymptotic velocities of the ejecta from our models, relative to what is needed to account for the spectra of type Ic-BL SNe is, like the low degree of neutronization, a consequence of the thermal nature of mass ejection when using viscous hydrodynamics. In the context of neutron star mergers disk outflows, Fahlman & Fernández (2018) studied the ability of viscous hydrodynamic simulations to produce high-velocity ejecta, over a wide range of (plausible) parameter space, finding that there is a limit to the outflow speed. Subsequent post-merger disk simulations in MHD showed that this limit can easily be overcome by a combination of mechanical ejection by the Lorentz force and neutrino absorption (Combi & Siegel (2023); Curtis et al. (2023a); Kiuchi et al. (2023); Fahlman et al. (2023)). We surmise that a similar phenomenon is applicable to collapsar disk outflows, with inclusion of MHD in long-term disk simulations boosting wind speeds to values compatible with observed supernova spectra.

The usefulness of the gap in neutrino emission between BH formation and collapsar disk formation (Figure 2.10) as a diagnostic of supernova physics is contingent on an accurate evolution prior to BH formation. In this respect, phenomena such as transient accretion disk formation during the protoneutron star phase (e.g., Obergaulinger & Aloy (2022)) and magnetic effects would alter the evolution of the neutrino lumi-

nosities and cannot be captured by spherically symmetric core-collapse like we have used here.

The shock oscillations observed during the NDAF phase in some models resemble the standing shock oscillations seen in the post-bounce phase of core-collapse SNe (the ‘SASI’, Blondin et al. (2003); Foglizzo et al. (2007)). Keeping in mind the qualitative differences between the standing shock in core-collapse SNe and the shock that bounds the accretion disk in collapsars (c.f. Section 2.3.1), it is worth noting that in the former, the oscillation frequencies are tied to oscillations in the neutrino luminosity, which would be observable in a galactic SN (Lund et al. (2010); Tamborra et al. (2013)), as well as to detectable gravitational wave emission (e.g., Kotake et al. (2009); Murphy et al. (2009)). While our axisymmetric simulations only allow for poloidal oscillations, a three-dimensional model would allow for the existence of spiral modes. This could in principle result in qualitative differences in the flow dynamics: the ADAF phase, during which we find freezing of oscillations, can be unstable to non-axisymmetric perturbations (Gu & Lu (2006); Nagakura & Yamada (2009)), consistent with the results of Gottlieb et al. (2022). A more in-depth analysis of correlations between shock oscillations and temporal fluctuations in the neutrino luminosity will inform the potential for these oscillations to also be an observable of the shocked disk in collapsars.

An in-depth analysis of nucleosynthesis of the disk outflow, making full use of the 19-isotope network and post-processing of tracer particles, will be presented in a follow up paper.

2.5 Nuclear Burning and Equation of State

2.5.1 Internal Energy Update

After the hydrodynamic step is complete, the internal energy is first updated by viscous heating and neutrino heating/cooling from the leakage/absorption scheme

$$\epsilon^{n+1/2} = \epsilon^n + \left(\frac{1}{\rho\nu} T : T + q_\nu \right) \Delta t \quad (2.25)$$

where the superscript denotes time step (all other symbols follow the notation in Section 2.2.2). The subsequent update due to nuclear energy release depends on whether nuclear species are evolved by the nuclear reaction network or the NSE solver.

For $T < 5 \times 10^9$ K, we use the nuclear network to update abundances. The change in nuclear binding energy is then accounted for in the Newton-Raphson iteration to find the temperature, instead of its normal direct application as a source term.

$$X_i^{n+1} = \int_{t^n}^{t^{n+1}} \Theta_i dt + \Gamma_{\nu,i} \Delta t \quad (2.26)$$

$$\epsilon^{n+1}(T^{n+1}) \Big|_{\rho, \mathbf{X}} = \epsilon^{n+1/2} + \sum_i B_i (X_i^{n+1} - X_i^n) \quad (2.27)$$

where $B_i = \chi_i/m_i$ is the nuclear binding energy per unit mass of species i , and the charged-current abundance rate of change terms $\Gamma_{\nu,i}$ are all zero except for $i = \{\text{n, p}\}$. The right hand side of equation (2.27) is then used as the input internal energy to match with the N-R solver in the Helmholtz EOS.

For $T \geq 5 \times 10^9$ K abundances are determined by the NSE solver for a given $\{\rho, T, Y_e\}$ combination. Instead of equations (2.26)-(2.27), we have

$$X_{\{\text{n,p}\}}^{n+1/2} = \Gamma_{\nu, \{\text{n,p}\}} \Delta t \quad (2.28)$$

$$Y_e^{n+1/2} = \sum_i \frac{Z_i}{A_i} X_i^{n+1/2} \quad (2.29)$$

$$\left[\epsilon^{n+1}(T^{n+1}) - \sum_i B_i X_i^{n+1}(T^{n+1}) \right] \Big|_{\rho, Y_e^{n+1/2}} = \epsilon^{n+1/2} - \sum_i B_i X_i^n \quad (2.30)$$

Equation (2.30) defines the new Newton-Raphson function to obtain the temperature, internal energy, and abundances at step $n + 1$ (the NSE abundances must be updated during each iteration, i.e. it is a nested Newton-Raphson system). The derivative of this function requires $(\partial\epsilon/\partial T)_{\rho, Y_e}$, which is computed by the Helmholtz EOS, and $(\partial X_i/\partial T)_{\rho, Y_e}$, which can be obtained from the NSE solution at each iteration.

2.5.2 Nuclear Statistical Equilibrium (NSE)

To obtain the abundances in NSE, we start from the chemical potential for each nuclear species i assuming Maxwell-Boltzmann statistics:

$$\mu_i = k_B T \left[\ln \left(\frac{n_i}{n_{Q,i}} \right) - \ln \omega_i \right] - \chi_i \quad (2.31)$$

where n_i is the number density, ω_i is the partition function, χ_i is the nuclear binding energy, and

$$n_{Q,i} = \left(\frac{m_i k_B T}{2\pi \hbar^2} \right)^{3/2}. \quad (2.32)$$

is the quantum concentration (e.g., Kittel & Kroemer (1980)). Solving for the number density in equation (2.31) and expressing as a mass fraction yields

$$X_i = \frac{m_i}{\rho} \omega_i n_{Q,i}(T) \exp \left(\frac{\mu_i + \chi_i}{k_B T} \right). \quad (2.33)$$

Nuclear statistical equilibrium is obtained by imposing chemical equilibrium for each species

$$\mu_i = N_i \mu_n + Z_i \mu_p, \quad (2.34)$$

where $N_i = A_i - Z_i$ is the number of neutrons in each nucleus, as well as mass and charge conservation

$$\sum_i X_i = 1 \quad (2.35)$$

$$\sum_i \frac{Z_i}{A_i} X_i = Y_e. \quad (2.36)$$

In practice, calculation involves doing a non-linear root find² for $\{\mu_n, \mu_p\}$ by replacing equations (2.33)-(2.34) into (2.35)-(2.36), for given values of $\{\rho, T, Y_e\}$.

²We use the NSE solver written by F. Timmes, available at cococubed.asu.edu

The temperature derivatives of the abundances in NSE can be obtained by replacing equation (2.34) in equation (2.33) and differentiating

$$\left(\frac{\partial X_i}{\partial T}\right)_{\rho, Y_e} = \frac{X_i}{T} \left[\frac{3}{2} + \frac{N_i}{k_B} \left(\frac{\partial \mu_n}{\partial T}\right)_{\rho, Y_e} + \frac{Z_i}{k_B} \left(\frac{\partial \mu_p}{\partial T}\right)_{\rho, Y_e} - \frac{1}{k_B T} (N_i \mu_n + Z_i \mu_p + \chi_i) \right], \quad (2.37)$$

where we have assumed that the partition function ω_i is constant; inclusion of that term (if known) is straightforward. The derivatives of the chemical potentials can be obtained by differentiating equations (2.35)-(2.36) with respect to temperature, and substituting equation (2.37), which yields a 2×2 linear system that can be solved analytically once $\{\mu_n, \mu_p\}$ are known:

$$\left(\sum_i N_i X_i\right) \left(\frac{\partial \mu_n}{\partial T}\right)_{\rho, Y_e} + \left(\sum_i Z_i X_i\right) \left(\frac{\partial \mu_p}{\partial T}\right)_{\rho, Y_e} = \left[\frac{1}{T} \sum_i X_i (N_i \mu_n + Z_i \mu_p + \chi_i) - \frac{3}{2} k_B\right] \quad (2.38)$$

$$\left(\sum_i \frac{Z_i N_i}{A_i} X_i\right) \left(\frac{\partial \mu_n}{\partial T}\right)_{\rho, Y_e} + \left(\sum_i \frac{Z_i^2}{A_i} X_i\right) \left(\frac{\partial \mu_p}{\partial T}\right)_{\rho, Y_e} = \left[\frac{1}{T} \sum_i \frac{Z_i X_i}{A_i} (N_i \mu_n + Z_i \mu_p + \chi_i) - \frac{3}{2} k_B Y_e\right]. \quad (2.39)$$

2.6 Variable Floors

2.6.1 Density, pressure and internal energy floors

We use variable floors with radial and polar angle dependencies for density, pressure, and internal energy. The general functional form is

$$W_{\text{floor}}(r, \theta) = W_0 \cdot f_{\text{floor}}(r, \theta) \quad (2.40)$$

where W stands for any of $\{\rho, p, \varepsilon\}$, W_0 is a constant value, and f_{floor} is a dimensionless function with a maximum of 1 which contains the radial and polar angle dependencies.

The floor function is in turn a product of radial and angular factors:

$$f_{\text{floor}}(r, \theta) = f_r(r) \cdot f_\theta(\theta) \quad (2.41)$$

The radial factor is a 5-piece power-law function given by:

$$f_r(r) = \begin{cases} 1 & r < R_1 \\ \left(\frac{R_1}{r}\right)^{s_1} & R_1 < r < R_2 \\ \left(\frac{R_1}{R_2}\right)^{s_1} \left(\frac{R_2}{r}\right)^{s_2} & R_2 < r < R_3 \\ \left(\frac{R_1}{R_2}\right)^{s_1} \left(\frac{R_2}{R_3}\right)^{s_2} \left(\frac{R_3}{r}\right)^{s_3} & R_3 < r < R_4 \\ \left(\frac{R_1}{R_2}\right)^{s_1} \left(\frac{R_2}{R_3}\right)^{s_2} \left(\frac{R_3}{R_4}\right)^{s_3} \left(\frac{R_4}{r}\right)^{s_4} & r > R_4 \end{cases} \quad (2.42)$$

where R_i and s_i are constant transition radii and slopes, respectively. This functional form is chosen to approximately follow the radial stellar profile, with normalization values W_0 such that each floor stays a few orders of magnitude below the actual hydrodynamic variable throughout the simulation. Transition radii and slopes were determined through comparison to the initial stellar profile, as well as iterative analysis of initial model evolution, with slopes ranging from 0.5 – 50. The normalization coefficients are model-dependent, falling in the range $\rho_0 = 10^4 - 10^5 \text{ g cm}^{-3}$ for density, $P_0 = 10^{22} - 10^{23} \text{ dyn cm}^{-2}$ for pressure, and $\epsilon_0 = 10^{17} - 10^{18} \text{ erg g}^{-1}$ for internal energy.

The angular factor is:

$$f_\theta(\theta) = (1 - \tilde{\theta}_{\text{eq}}) \cos(\theta)^{2\tilde{\theta}_w} + \tilde{\theta}_{\text{eq}} \quad (2.43)$$

where $\tilde{\theta}_{\text{eq}}$ is the equatorial floor, and $\tilde{\theta}_w$ is a width factor that controls how quickly the floor drops off away from the poles toward the equator. This functional form is used to deal with the low density funnel near the poles, without interfering with the disk at the equator.

2.6.2 Temperature floor

Our temperature floor is given by:

$$T_{\text{floor}}(r) = \max \left[10^7 \text{ K} \cdot \left(\frac{50 \text{ km}}{r} \right)^2, 10^4 \text{ K} \right], \quad (2.44)$$

where the minimum value is associated with the bottom of the Helmholtz EOS table in FLASH. This functional form is necessary to deal with problematic cells at the shear

interface between the shocked disk and the low-density funnel near the inner radial boundary.

Chapter 3

Collapsar disk outflows II: Heavy element production

3.1 Introduction

The majority of chemical elements other than hydrogen and helium are made in stellar interiors, or in stellar explosions, through a variety of nuclear processes (e.g., Burbidge et al. (1957); Johnson (2019)). Massive stars are expected to produce mostly alpha chain elements during stellar evolution, and iron-group elements through explosive nucleosynthesis during the supernova (SN) (e.g., Janka & Bauswein (2023)). Whether and how the rapid-neutron capture process (*r*-process) occurs in these SNe is an area of active theoretical research (e.g., Wanajo et al. (2018); Witt et al. (2021); Wang & Burrows (2023)). Observationally, there may be a need for an *r*-process source that operates with a shorter time-delay after star formation than neutron star (NS) mergers, at least to explain the europium enrichment of some extremely metal-poor stars in the halo of our galaxy (Mathews & Cowan, 1990; Cavallo et al., 2023). A source that operates on the timescale of massive star evolution ($\sim 10^6$ yr) would bridge this gap.

Collapsars are a subset of massive stellar explosions, corresponding to a failed supernova of a rapidly-rotating progenitor that forms a black hole (BH) accretion disk Woosley (1993). If a relativistic jet is launched and successfully traverses the stellar envelope, a long-duration gamma-ray burst (LGRB) is produced (e.g., MacFadyen & Woosley (1999)). The accretion disk can, by itself, launch a sub-relativistic outflow

that can eject the stellar envelope, possibly accounting for the broad-line type Ic (Ic-BL) SNe associated with IGRBs MacFadyen (2003).

If the accretion disk in a collapsar reaches the neutrino-cooled (“NDAF”) regime, then significant neutronization can occur, providing the conditions for the r -process to operate MacFadyen & Woosley (1999); Kohri et al. (2005). However, one of the main remaining uncertainties is how much of the neutron-rich material from the disk makes its way into the outflow and is ejected.

In addition, not all solar heavy element abundances can be explained by the s - and r -processes. Particularly, proton-rich isotopes such as ^{96}Ru and ^{92}Mo , as well as ^{92}Nb , which are shielded on the (N, Z) -plane by other stable isotopes and cannot be produced by β -decays from the neutron rich side of the valley of stability. While some of these p -nuclei have been proposed to be produced by the photodisintegration of s - and r - process nuclei by gamma rays (the γ -process) in core-collapse (CC) SNe environments Woosley & Howard (1978); Howard et al. (1991), the γ -process alone cannot explain all p -nuclei in the solar abundance. Other p -nuclei production processes often require some explosive astrophysical environments with proton rich $Y_e > 0.5$ ejecta Wallace & Woosley (1981); Fröhlich et al. (2006). Recent viscous hydrodynamic simulations of collapsar disk outflows Just et al. (2022a); Fujibayashi et al. (2023a) produce at least some fraction of the ejecta with proton-rich conditions ($Y_e > 0.5$), suggesting nucleosynthesis may occur in these explosions on the proton-rich side of the “valley of stability” via the rapid proton capture process (rp -process).

Heavy element production has been investigated both in collapsar jets and in disk winds, on the assumption that neutronized material will make its way out of the star. One-dimensional, steady-state nucleosynthesis calculations including the production of ^{56}Ni and r -process elements have been performed for stellar mass BH-accretion disk outflows by Pruet et al. (2003), Fujimoto et al. (2004), and Surman et al. (2006). Nucleosynthesis calculations on magnetically-driven jets have found that a small amount r -process element production is possible when neutron-rich material from the disk is

ejected via the jet Fujimoto et al. (2007); Ono et al. (2012); Nakamura et al. (2013). More recently, general-relativistic magnetohydrodynamic (GRMHD) simulations of collapsar disks that start from equilibrium tori and neglect the infalling mantle of the star produce r -process elements in a mass accretion rate-dependent way Siegel et al. (2019); Miller et al. (2020). Additionally, the electron fraction of the ejecta in these simulations, and the extent of r -process element production, differs based on the neutrino transport schemes used.

From the observational perspective, the presence of r -process elements in collapsar ejecta have been predicted semi-analytically to produce a detectable near-infrared excess during the photospheric phase, relative to a non- r process enriched CCSN Barnes & Metzger (2022). A study of the late time light-curves of four SNe-GRB (attributed to collapsar sources) was inconclusive in determining the presence of r -process enrichment, with light-curves consistent with both no r -process enrichment or little ($0.01 - 0.15M_{\odot}$) r -process contribution Rastinejad et al. (2023).

In order to generate a complete description of the elements produced in collapsars, as well as to answer the question of whether r -process elements can be produced in these explosions, there is a need for global, long-term simulations of collapsar disk outflows that include the physics relevant for nucleosynthesis that is not present in existing work. Axisymmetric, viscous hydrodynamic models allow for longer term simulations than 3D GRMHD calculations, following disk formation from the collapsing progenitor, and evolving the disk wind driven shock through the stellar mantle of the star. Recent works (Just et al. (2022a), Fujibayashi et al. (2023a), Fujibayashi et al. (2023b), and Dean & Fernández (2024) [hereafter Paper I]) use this method, and find that there is insufficient neutronization in ejected material to produce significant quantities of r -process elements.

In Paper I, we introduced a numerical approach to conduct global simulations of collapsars, starting from pre-collapse, rotating Wolf-Rayet stars. Progenitors are evolved from core collapse to BH formation with a general relativistic, spherically-

symmetric, neutrino radiation-hydrodynamics code that accounts for approximate rotation effects. Results are then mapped into a axisymmetric hydrodynamics code for longer-term evolution ($\gtrsim 100$ s), including neutrino emission and absorption, viscous angular momentum transport, self-gravity, and a 19-isotope nuclear network, capturing BH accretion disk formation self-consistently, and outflow production until the shocked wind reaches the stellar surface. Results show that the disk wind is consistently capable of driving a successful stellar explosion. However, we found insufficient neutronization of the disk outflow to produce significant heavy r -process elements. The ejecta nevertheless contains sufficient ^{56}Ni to power a type Ic-BL light curve.

Here we perform detailed nucleosynthesis analysis of the models from Paper I, and present additional models that employ progenitors with a modified rotation profile, aimed at maximizing the chance of ejecting neutron-rich matter in the disk outflow.

The paper is structured as follows: Section 3.2 provides an overview of the numerical setup presented in Paper I, placement and post-processing of tracer particles, modification of stellar rotation profiles, and a list of models evolved. Section 3.3 compares the results of the simulations using progenitors with modified rotation relative to those from Paper I, as well as our nucleosynthesis results, and comparison with previous work. Section 3.4 contains a summary and discussion.

3.2 Methods

The numerical setup used for our simulations is discussed in detail in Paper I, here we provide a brief summary of the numerical hydrodynamic methods employed. We also describe the use of tracer particles and a nuclear reaction network for nucleosynthesis in post-processing, as well as modifications to the stellar rotation profile.

3.2.1 Summary of Computational Approach

We employ two rapidly rotating Wolf-Rayet progenitor stars (16TI and 350C) from Woosley & Heger (2006). The stars are evolved from the onset of core collapse until BH formation with the spherically-symmetric, general relativistic neutrino radiation-hydrodynamic code `GR1D` version 1 O’Connor & Ott (2010). Rotational effects are included in approximate form during this evolution stage. At the point of BH formation, the stellar progenitor is mapped into a two-dimensional (2D) axisymmetric viscous hydrodynamic setup based on the astrophysical hydrodynamics code `FLASH` version 3.2 Fryxell et al. (2000); Dubey et al. (2009).

The public version of `FLASH` has been modified to include viscous angular momentum transport, a customized implementation of multipole (Newtonian) self-gravity, and a neutrino leakage scheme that accounts for emission and absorption. The pseudo-Newtonian potential of Ref. Artemova et al. (1996) is included to account for the gravity of a spinning BH, with mass and angular momentum updated at every timestep by accreting matter. We employ the (Helmholtz) equation of state of Timmes & Swesty (2000), extended to higher and lower densities relative to the table in `FLASH`, as outlined in Paper I.

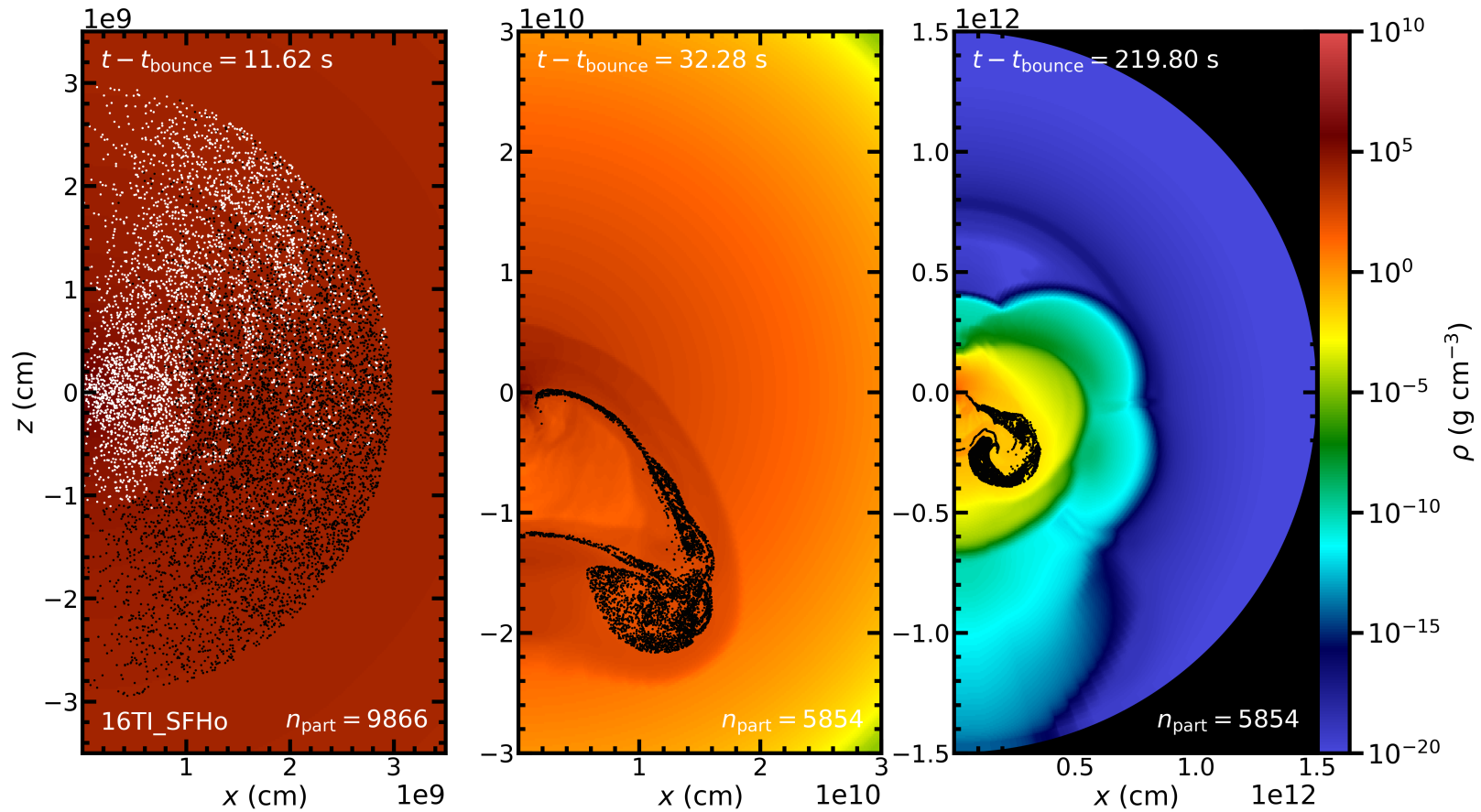


Figure 3.1: Snapshots of the density in model 16TI_SFHo at three points in the simulation, as labelled, corresponding to initial particle placement (left), shortly after the start of rapid shock expansion (middle), and end of the simulation (right). Tracer particle positions are overlaid, with white dots corresponding to particles that end up accreted onto the BH, and ejected particles marked in black. The number of particles remaining in the computational domain is listed in each panel, including the small number that never exceed 1 GK and are discarded from the analysis. The black region visible in the third panel marks the outermost edge of the spherical grid.

Finally, all simulations include the 19-isotope nuclear reaction network of Weaver et al. (1978), as implemented in FLASH, to track nuclear energy changes during the simulation. This also allows us to obtain detailed composition information for the set of 19 isotopes: n, p⁺, ³He, ⁴He, ¹²C, ¹⁴N, ¹⁶O, ²⁰Ne, ²⁴Mg, ²⁸Si, ³²S, ³⁶Ar, ⁴⁰Ca, ⁴⁴Ti, ⁴⁸Cr, ⁵²Fe, ⁵⁴Fe, ⁵⁶Fe, and ⁵⁶Ni. Above a temperature $T_{\text{NSE}} = 5$ GK, we supplement this network with a nuclear statistical equilibrium (NSE) solver, based on that reported in Seitenzahl et al. (2008)¹.

3.2.2 Nucleosynthesis in Post-Processing

To explore heavy element nucleosynthesis over a much wider range of isotopes than those in the embedded 19-isotope network, we use a standard post-processing approach with passive tracer particles and an external nuclear reaction network. Particles record thermodynamic and kinematic quantities, as well as other source terms such as energy or lepton number rates of change, which act on individual fluid parcels for the duration of the simulation.

For each model, $\sim 10^4$ particles are initialized at the time of disk formation. Particles are initialized at random locations, with tracers having equal mass and following the density distribution, constrained to the radial range 10^5 cm - 3×10^9 cm in all models except 350C_SFHo_ $k_{\text{rad}}10$, for which the radial range is 10^6 cm - 10^{10} cm. This radial range was chosen as a first attempt to obtain a reasonable sampling of the neutrino-reprocessed matter that is used consistently in all simulations. Particles do not sample all ejected material, however. In Sec. 3.3.5 we quantify sampling of the ejecta by the particles, and develop suggestions for initial particle placement in future collapsar simulations.

Figure 3.1 shows a density colour map of model 16TI_SFHo with overlaid particle positions, shortly after particle placement (left panel), midway through the simulation after the onset of rapid expansion (middle panel), and at the end of the simulation

¹Available at <https://cococubed.com/>.

(right panel). Black dots denote particles that eventually make their way into the outflow, and white dots show particles accreted onto the BH. The number of particles out of the initial 10^4 that remain within the computational domain are labelled in each snapshot. The middle and right panels illustrate that the shock wave in this model expands towards the $-\hat{z}$ pole due to the instability to axisymmetric perturbations described in Paper I. It is apparent that as a result of this asymmetric expansion, there is additional accretion from the $+\hat{z}$ pole direction, with the majority of particles initialized in that hemisphere not making their way into the outflow. Nucleosynthesis calculations are performed on particles that are unbound (positive Bernoulli parameter) at the end of the simulation. While the particles do not completely sample the ejecta, ejected particles mostly represent the peak of the mass ejection distribution (Section 3.3.5).

Tracer particles are post processed with the nuclear reaction network **SkyNet** Lippuner & Roberts (2017), using the same settings as in Refs. Lippuner et al. (2017b); Fernández et al. (2020, 2022). The network uses ~ 7800 isotopes and $> 10^5$ reactions, including strong forward reaction rates from the REACLIB database Cyburt et al. (2010), with inverse rates computed from detailed balance; spontaneous and neutron-induced fission rates from Frankel & Metropolis (1947), Mamdouh et al. (2001), Wahl (2002), and Panov et al. (2010); weak rates from Fuller et al. (1982), Oda et al. (1994), Langanke & Martínez-Pinedo (2000), and the REACLIB database; and nuclear masses from the REACLIB database, including experimental values where available, or otherwise theoretical masses from the Finite-Range Droplet Macroscopic model (FRDM) of Möller et al. (2016). Post-processing of tracer particles begins the last time the temperature exceeds 6×10^9 K. When the temperature exceeds 5×10^9 K the abundances are evolved in NSE. Trajectories that never exceed 5×10^9 K are evolved from the time they reach maximal temperature, assuming NSE. Particles that never exceed 10^9 K are discarded. Trajectories are evolved in **SkyNet** for 30 years, extrapolating from the end of the **FLASH** simulation ($\sim 100\text{--}400$ s) assuming homologous

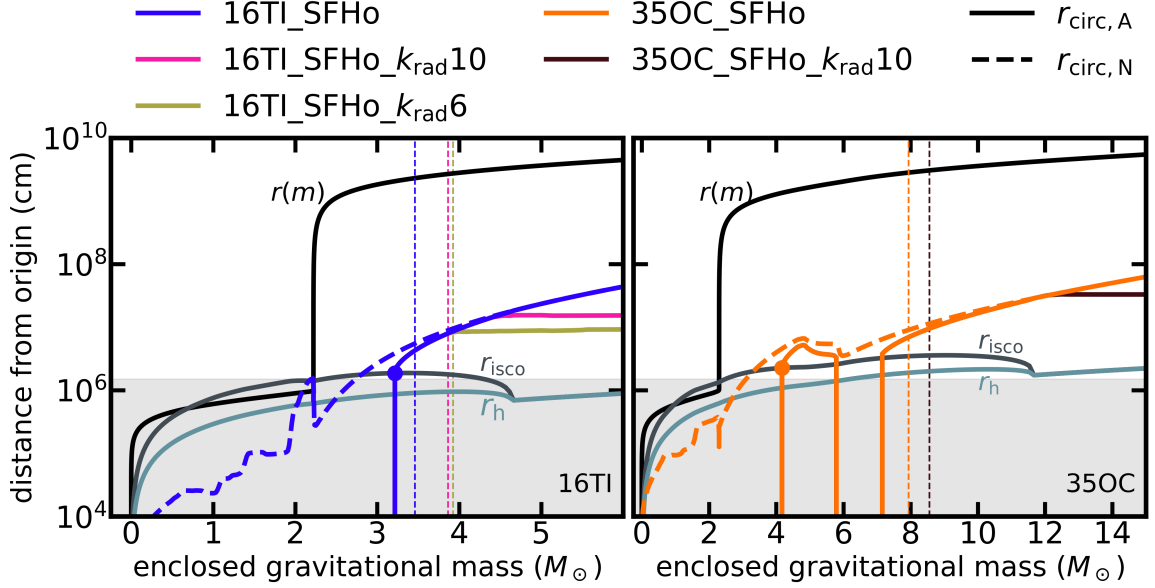


Figure 3.2: Characteristic radial distances as a function of enclosed gravitational mass for stellar progenitors 16TI and 350C from Woosley & Heger (2006) at the last snapshot in GR1D prior to BH formation. The radial coordinate is $r(m)$ (black solid), with the the PNS surface corresponding to the vertical segment at $M \simeq 2M_\odot$. Colored lines without label show circularization radii obtained with the pseudo-Newtonian potential employed by the code (solid) and a Newtonian potential with the same enclosed mass (dashed, c.f. Eq. 3.2), with colors corresponding to different models, as labeled above. Models 16TI_SFHo and 350C_SFHo were presented in Paper I, while remaining models have the modified rotation profile discussed in Section 3.2.3 (Equation 3.3), with the value of $k_{\text{rad}} = \{6, 10\}$ indicated in the model name. Finally, each panel shows the event horizon radius r_h and radius of the innermost stable circular orbit r_{isco} for a BH with the same enclosed mass and angular momentum as in the progenitor with unmodified $j(M)$. The gray shaded region is excised from the computational domain when mapping to FLASH. The BH mass when disk formation is predicted to occur is marked with a circle, while the BH mass at actual disk formation in each simulation is marked with a thin vertical dashed line.

evolution of density with time ($\rho \propto t^{-3}$).

3.2.3 Modified Progenitor Rotation Profile

The progenitor stars 16TI and 350C have specific angular momenta j such that the circularization radius²

$$r_{\text{circ}} = \frac{j^2}{GM} \quad (3.1)$$

increases monotonically with increasing distance from the center of the star outside the mass coordinate of disk formation. In Eq. (3.1), M is the enclosed gravitational mass. As a result, mass shells located further out circularize at larger distances from the BH upon collapse, thus reaching lower maximal temperatures. Given the sensitivity of neutrino emissivities to temperature, this configuration limits the range of stellar shells that are subject to significant neutronization when contributing to the shocked accretion disk, and hence limits the occurrence of neutron-rich nucleosynthesis.

²We neglect the difference between circularization radii obtained with Newtonian or pseudo-Newtonian potentials, as the difference matters only prior to disk formation (Figure 3.2).

Table 3.1: List of models studied in this paper, and key quantities. The first five models were introduced in Paper I, and the last three (16TI_SFHo_ $k_{\text{rad}}6$, 16TI_SFHo_ $k_{\text{rad}}10$, and 350C_SFHo_ $k_{\text{rad}}10$) are new. Columns from left to right show the model name, progenitor star from Woosley & Heger (2006), EOS used in GR1D evolution to BH formation, viscosity parameter used in the 2D post-BH evolution in FLASH, and angular momentum profile factor k_{rad} (Equation 3.3). Subsequent columns show times relative to core bounce time in GR1D (BH formation time in GR1D t_{bh} , shocked disk formation time in FLASH t_{df} , shock breakout time t_{sb} , and the maximum simulation time t_{max}), and BH masses at various points in time (BH mass at disk formation, BH mass at the transition to the ADAF phase [Sec. 3.3.1], and final BH mass).

Model	Progenitor	EOS	α	k_{rad}	t_{bh} (s)	t_{df} (s)	t_{sb} (s)	t_{max} (s)	$M_{\text{bh}}(t_{\text{df}})$ (M_{\odot})	$M_{\text{bh}}(t_{\text{ADAF}})$ (M_{\odot})	$M_{\text{bh}}(t_{\text{max}})$ (M_{\odot})
16TI_SFHo	16TI	SFHo	0.03	—	2.72	11.1	116	219.8	3.5	3.7	4.4
16TI_SFHo_ α 01			0.1	—	2.72	11.0	236	427.1	3.5	$-^3$	4.1
16TI_SFHo_ α 001			0.01	—	2.72	10.6	153	295.4	3.4	4.4	4.6
16TI_DD2		DD2	0.03	—	5.24	9.9	168	302.0	2.9	3.2	3.7
350C_SFHo	350C	SFHo		—	0.99	10.8	68	102.8	7.9	10.2	11.7
16TI_SFHo_ $k_{\text{rad}}6$	16TI			6	2.72	12.2	147	440.0	3.9	4.4	6.6
16TI_SFHo_ $k_{\text{rad}}10$				10	2.72	11.9	111	217.8	3.9	4.2	5.4
350C_SFHo_ $k_{\text{rad}}10$	350C				0.99	11.3	72	111.1	8.6	10.9	12.9

In an attempt to assess the sensitivity of the nucleosynthesis output to the angular momentum profile of the star, we evolve models with a modified $j(M)$ in the star, starting from core-collapse. In both progenitor models, the original rotation profile is sub-Keplerian over a significant fraction of the enclosed stellar mass, increasing outward to exceed Keplerian rotation in the outermost $\sim 0.3\%$ and $\sim 0.1\%$ of enclosed mass in models 16TI_SFHo and 350C_SFHo, respectively. The dynamical time at these locations is ~ 670 s and ~ 665 s, respectively. Effectively, the super-Keplerian layers are frozen over the timescale of the simulation.

The most optimistic case would be obtained if most of the stellar shells circularize close to the BH, so that matter is hot enough for strong neutrino reprocessing, while avoiding too short an accretion timescale, and keeping the disk formation process unaltered. We thus modify the angular momentum profile of the star so that a *constant circularization radius* is obtained outside a fixed mass shell, with the modified circularization radius satisfying

$$r_{\text{circ}}^* = \min(r_{\text{circ}}, k_{\text{rad}} \cdot r_{\text{in}}), \quad (3.2)$$

where r_{in} is the inner radial boundary of the computational domain and $k_{\text{rad}} = 6 - 10$ is a constant found by trial-and-error. The resulting functional form is shown in Figure 3.2.

The modified angular momentum profile j^* in the progenitor is then

$$j^*(M) = \begin{cases} j(M) & r_{\text{circ}} < k_{\text{rad}} r_{\text{in}} \\ (GM \cdot k_{\text{rad}} r_{\text{in}})^{1/2} & r_{\text{circ}} \geq k_{\text{rad}} r_{\text{in}}. \end{cases} \quad (3.3)$$

Note that the modified specific angular momentum still increases with enclosed mass ($\propto M^{1/2}$).

3.2.4 Models Evolved

Table 3.1 lists all the models studied in this paper. The first five were presented in Paper I. The baseline model is 16TI_SFHo, with 16TI_SFHo_α01 and 16TI_SFHo_-

³The 16TI_SFHo_α01 model does not exhibit an NDAF phase, starting in the ADAF phase at the time of disk formation.

$\alpha 001$ changing the magnitude of the viscosity parameter α , and 16TI_DD2 using a different EOS during the GR1D evolution. Model 350C_SFHo changes the progenitor star, keeping everything else constant.

Three new models are presented here: 16TI_SFHo_ $k_{\text{rad}}6$, 16TI_SFHo_ $k_{\text{rad}}10$, and 350C_SFHo_ $k_{\text{rad}}10$, which use the modified angular momentum profile of Equation (3.3), otherwise with the same settings as in models 16TI_SFHo and 350C_SFHo, respectively. The parameter k_{rad} is set such that the circularization radius plateaus with increasing enclosed mass at $\sim 2r_{\text{circ}}(M_{\text{df}})$ (Figure 3.2) in the corresponding un-modified model from Paper I (16TI_SFHo_ $k_{\text{rad}}6$ and 350C_SFHo_ $k_{\text{rad}}10$, c.f. Figure 3.2). Additionally, we explore a model with k_{rad} consistent with that of the other progenitor (16TI_SFHo_ $k_{\text{rad}}10$).

The BH mass at several times in the simulation is shown in Table 3.1. BH masses can increase by $\sim 5 - 50\%$ during the NDAF phase, depending on the model.

The maximum simulation time t_{max} for each model is also listed in Table 3.1, with the same criterion for stopping the simulation as in Paper I (the shock reaching the outermost radius of the computational domain, where $P \simeq 150 \text{ dyn cm}^{-2}$).

3.3 Results

3.3.1 Summary of Models from Paper I

After BH formation, the stellar mantle starts to accrete radially through the event horizon, adding to the mass (and modifying the spin) of the central BH. As the specific angular momentum j of infalling material increases, the circularization radius of infalling matter eventually exceeds the innermost stable circular orbit r_{isco} of the BH, forming an accretion disk. Figure 3.2 illustrates the variation of characteristic radii as a function of enclosed gravitational mass for each progenitor star, using a snapshot at the end of the GR1D evolution.

At this point, due to the angular momentum of accreted material, we see the

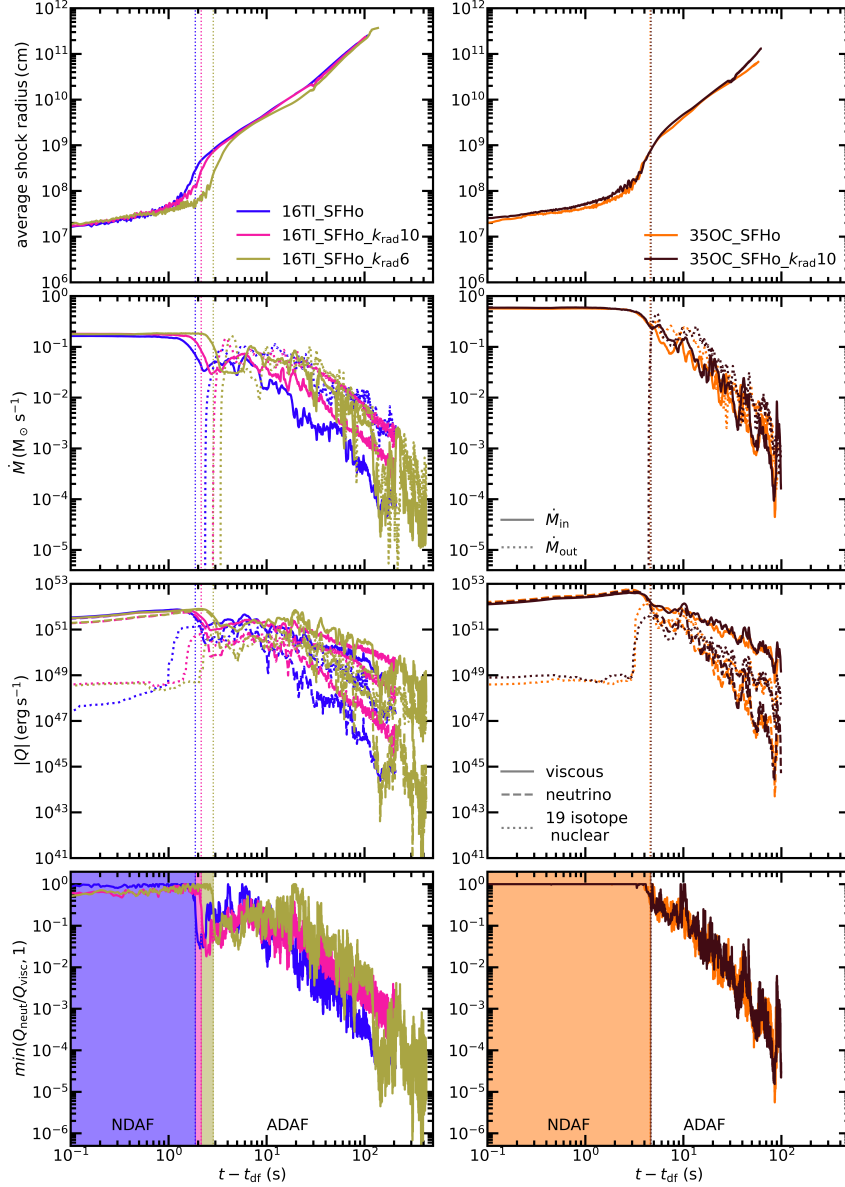


Figure 3.3: Evolution of models with modified angular momentum profile and the unmodified control set, as labelled (c.f. Table 3.1). *Top*: Evolution of the average shock radius as a function of post-disk formation time. The vertical dotted lines in each panel represent the transition from the NDAF to ADAF phase, as defined by Eq. (3.4). *Second from top*: Mass accretion rate \dot{M}_{in} across the inner radial boundary, and mass outflow rate \dot{M}_{out} across a spherical surface at $R_{\text{ej}} = 10^9$ cm as a function of time after disk formation. *Third from top*: Absolute value of viscous heating, net neutrino cooling, and nuclear energy injection as function of post-disk formation time. *Bottom*: Ratio of postshock-integrated net neutrino cooling to viscous heating as a function of post-disk formation time, capped at unity. The early NDAF phase (Eq. 3.4) is shaded, while the later ADAF phase extends beyond the vertical dotted line. Curves in Rows 2 and 3 are smoothed with a moving average of width 0.5 s, for visibility.

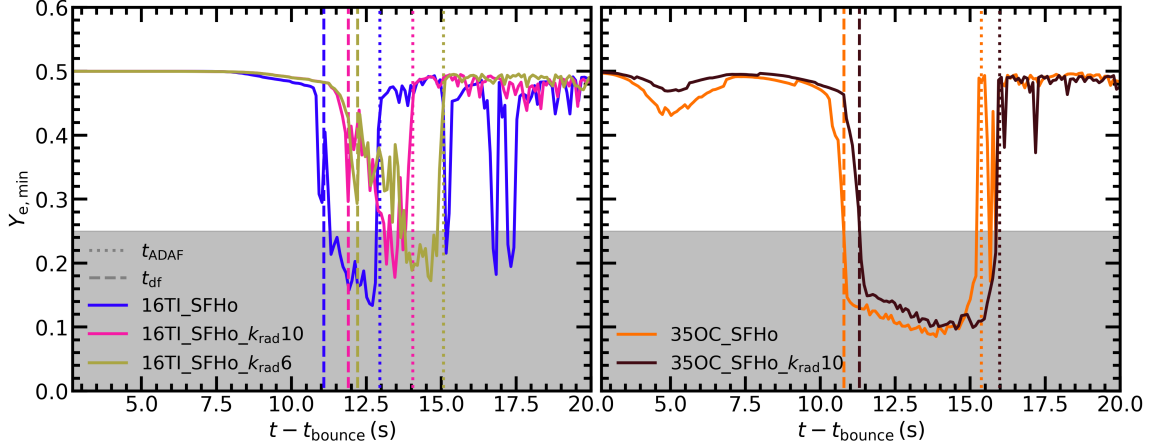


Figure 3.4: Minimum electron fraction in the simulation domain as a function of time, for different models, as labelled. Disk formation times are marked with a dashed line, and the transition from NDAF to ADAF phase (Eq. 3.4) is marked with a dotted line. The shaded region shows $Y_e < 0.25$, which is an approximate measure of the value below which lanthanides can be produced (e.g., Lippuner & Roberts (2015)).

buildup of matter at the equator (i.e. the formation of a “dwarf disk”), before transition to a thermalized disk and the emergence of a shock wave that separates the disk from the supersonically infalling star. Most models show poloidal oscillation of this shock wave during an initial NDAF phase, which occurs when viscous heating of the disk is balanced by neutrino cooling.

As the temperature and density of the disk drops, viscous heating becomes dominant over neutrino cooling, leading to a phase of rapid shockwave expansion during the Advection Dominated Accretion Flow (ADAF, Narayan & Yi (1994)) phase. On a timescale of $\sim 100 - 400$ s, the expanding shock wave in all cases reaches the stellar surface and the outer boundary of the computational domain. Paper I evolves five models varying the stellar progenitor, equation of state (EOS) used during GR1D evolution, and the strength of viscous angular momentum transport (α parameter).

3.3.2 Models with Modified Angular Momentum Profile

The three new models with modified angular momentum profile (16TI_SFHo_ $k_{\text{rad}6}$, 16TI_SFHo_ $k_{\text{rad}10}$, and 35OC_SFHo_ $k_{\text{rad}10}$) evolve in a qualitatively similar way to

their corresponding unmodified baseline model runs (16TI_SFHo and 350C_SFHo, respectively). Figure 3.3 illustrates differences in the evolution between these models.

The BH formation time in the GR1D evolution is unchanged, as the angular momentum profile remains unchanged in the core of the star. Disk formation in each of the models with modified angular momentum occurs $\sim 0.5 - 2$ s later than in their corresponding base model, owing to the increased accretion rate during this initial evolution phase (Figure 3.3). The BH masses at the time of disk formation also exceed those in the base models by $\sim 0.5M_{\odot}$ (Table 3.1).

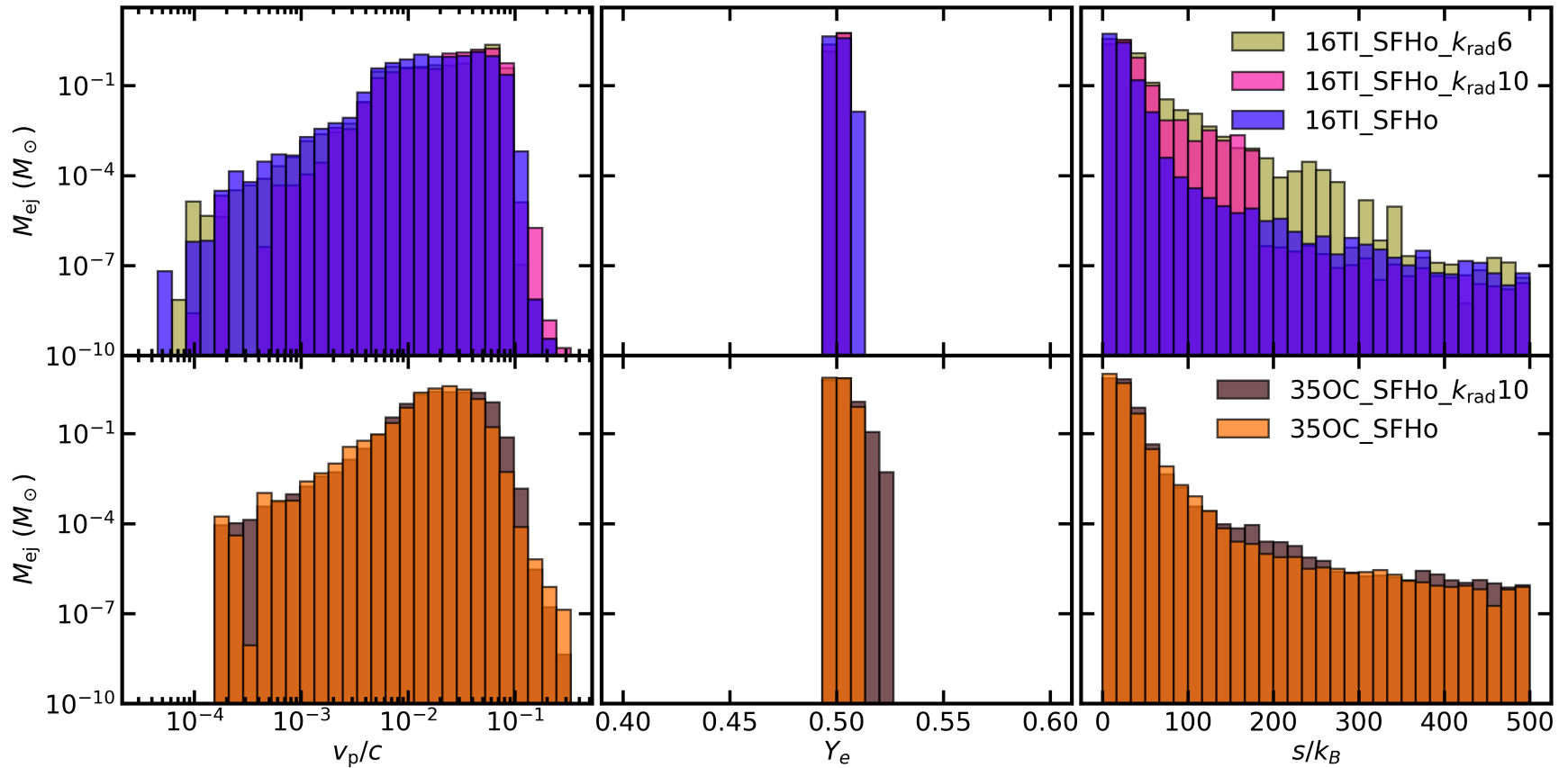


Figure 3.5: Unbound mass histograms at the end of the simulation, for models with modified rotation profile and their corresponding unmodified counterparts, as labelled (c.f. Table 3.1). Only matter with positive Bernoulli parameter and $v_r > 0$ is considered. Histograms are binned by poloidal velocity $v_p = (v_r^2 + v_\theta^2)^{1/2}$ (left), electron fraction Y_e (center), and entropy per baryon s/k_B (right).

Table 3.2: Bulk outflow properties, obtained by integrating unbound material at the end of the simulation, in models with modified angular momentum profile and their corresponding base models (c.f. Table 3.1). Columns from left to right show model name, ejecta mass, ejecta kinetic energy at the end of the simulation, asymptotic ejecta kinetic energy, mass-weighted average expansion velocity at infinity (Eq. 3.5), and minimum electron fraction of outflowing material (c.f. Fig. 3.4).

Model	M_{ej} (M_{\odot})	K_{ej} (10^{51} erg)	K_{∞} (10^{51} erg)	$\langle v_{\infty} \rangle$ (10^3 km s $^{-1}$)	$Y_{\text{e,min}}(t_{\text{max}})$
16TI_SFHo	8.19	9.07	9.2	8.7	0.498
16TI_SFHo_ $k_{\text{rad}}10$	7.93	14.1	14.4	12.0	0.498
16TI_SFHo_ $k_{\text{rad}}6$	7.01	13.8	14.0	12.3	0.495
350C_SFHo	15.1	9.45	10.6	7.7	0.497
350C_SFHo_ $k_{\text{rad}}10$	14.3	13.0	14.1	8.7	0.500

Like in most models from Paper I, and particularly in the baseline cases, the accretion disk begins in an NDAF stage and transitions to an ADAF phase at a time $\sim 1 - 5$ s after disk formation (with the exception of model `16TI_SFHo_α001`, for which the NDAF phase lasts ~ 12 s). For quantitative analysis, we define the transition between NDAF and ADAF phases in terms of the ratio of the absolute value of the (post-shock integrated) net neutrino cooling Q_ν to viscous heating Q_{visc} , according to:

$$\begin{cases} |Q_\nu/Q_{\text{visc}}| \geq 0.3 & \text{NDAF phase} \\ |Q_\nu/Q_{\text{visc}}| < 0.3 & \text{ADAF phase} \end{cases} \quad (3.4)$$

Figure 3.3 shows that this criterion consistently captures the sudden drop – and onset of large amplitude fluctuations – in the accretion rate onto the BH, which is a characteristic of the ADAF phase. Previous time-dependent studies of collapsar disks refer to the *ignition* accretion rate Chen & Beloborodov (2007); De & Siegel (2021) to mark the transition from NDAF to ADAF. This quantity is defined as the minimum accretion rate for which the condition between local (specific) energy source terms satisfies $q_{\text{visc}} - q_{\text{cool}} = q_{\text{visc}}/2$ somewhere in the disk, with q_{cool} including net neutrino cooling and nuclear dissociation. This condition is equivalent to $q_{\text{cool}}/q_{\text{visc}} = 0.5$, which is compatible with (but not identical to) our criterion.

Like in the base models, we see that after the transition to the ADAF phase, when rapid expansion of the shock begins, the shock front geometry freezes following the oscillatory instability to axisymmetric perturbations in the NDAF phase. This leads to the shock expanding to the stellar surface, often towards one of the poles ($+\hat{z}$ or $-\hat{z}$). We see very similar shock breakout times in models `16TI_SFHo` and `16TI_SFHo_–krad10`, while model `16TI_SFHo_–krad6` follows ~ 30 s later owing to the more significant change to the angular momentum profile. Similarly, models `350C_SFHo` and `350C_–SFHo_–krad10` evolve to shock breakout on very similar timescales (~ 5 s difference).

The minimum electron fraction in the computational domain occurs within the disk. This quantity drops to its lowest value shortly after disk formation, remaining low until the transition from the NDAF phase to the ADAF phase and the onset of

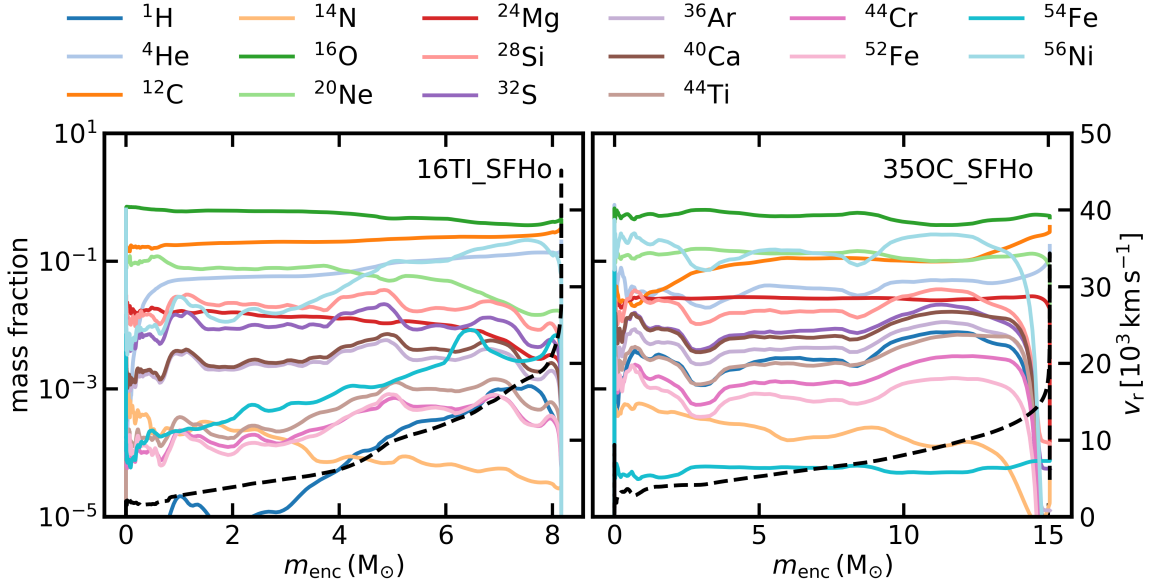


Figure 3.6: Angle-averaged mass fractions in unbound material of selected isotopes from the 19-isotope network, as a function of angle-averaged enclosed mass, for models 16TI_SFHo (left) and 350C_SFHo (right). The black dashed line shows the angle-averaged radial velocity of the ejecta as a function of enclosed mass (right y-axis). The mass fraction of ^1H represents a combination of p^+ and ^1H .

rapid expansion of the shock wave (Figure 3.4). The duration of the phase with significant neutronization is ~ 2 s for models 16TI_SFHo and 16TI_SFHo_ $k_{\text{rad}}10$, but extends slightly longer in model 16TI_SFHo_ $k_{\text{rad}}6$ (~ 3 s), which has a j profile that results in a smaller circularization radius (Eq. 3.3). The duration of neutronization in models 350C_SFHo and 350C_SFHo_ $k_{\text{rad}}10$ are also consistent with one another (~ 4.5 s), with the onset of neutronization delayed from the base 350C_SFHo model by ~ 0.5 s (Figure 3.3). Overall, modification of the angular momentum profile did not produce a significant lengthening of the neutronization phase relative to the base models, except for 16TI_SFHo_ $k_{\text{rad}}6$. Even in that case, however, this longer neutronization resulted in only a small effect on the electron fraction of the ejecta.

Figure 3.5 shows the velocity, electron fraction, and entropy distributions of unbound material in the computational domain (positive Bernoulli parameter) at the end of the simulation, for models with modified angular momentum profile, as well as for their corresponding base models. Histograms from models with modified rotation

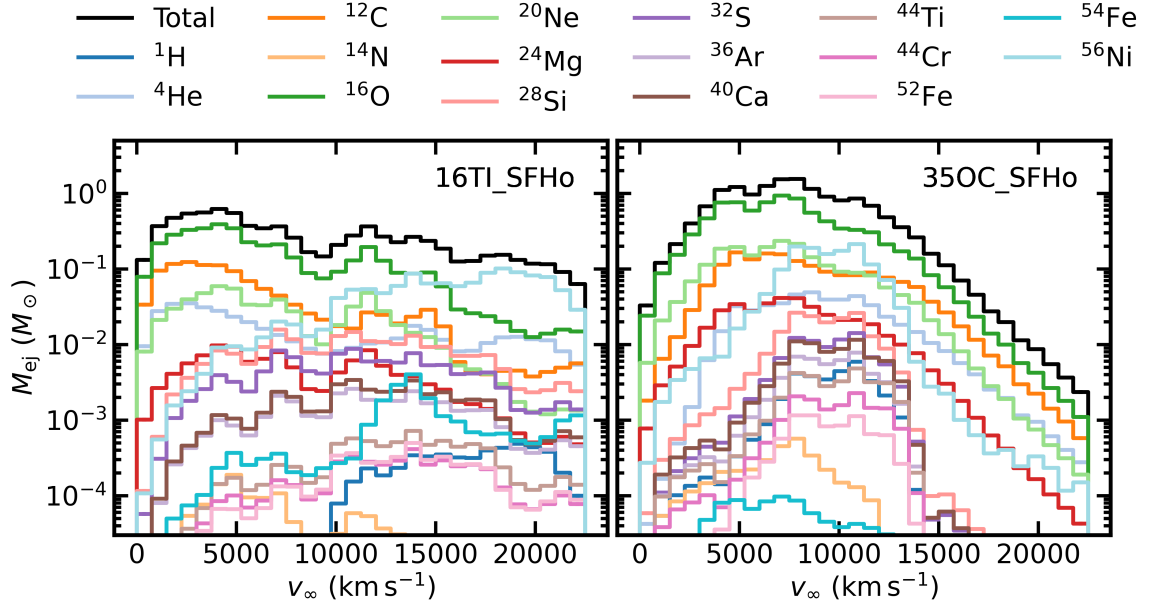


Figure 3.7: Unbound mass histograms of selected isotopes from the 19-isotope network, binned by asymptotic velocity (Equation 3.5) for models 16TI_SFHo (left) and 35OC_SFHo (right). The ^1H ejecta mass represents a combination of the p^+ and ^1H ejecta masses.

show the same overall features as their fiducial counterparts: broad velocity distribution peaking at $\sim 6 \times 10^{-2} c$, narrow electron fraction distribution, with most ejecta having $Y_e \sim 0.5$, and an entropy distribution that peaks at $\sim 10 k_B$ per baryon and has a long tail reaching several hundred k_B or more.

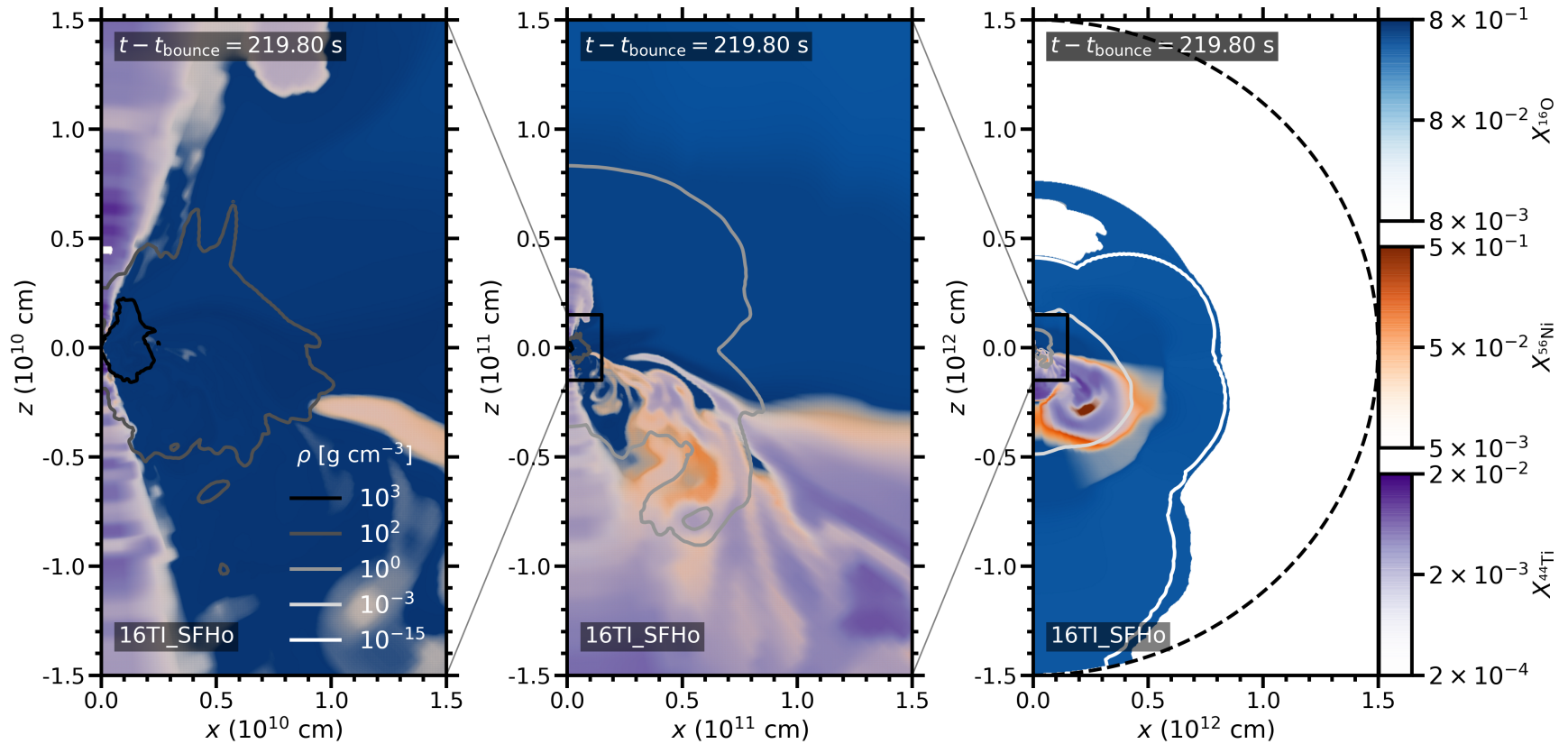


Figure 3.8: Mass fractions of ^{16}O , ^{44}Ti , and ^{56}Ni at the last simulated time in model 16TI_SFHo, with density contours overlaid. Data is not shown when the atmospheric mass fraction $X_{\text{atm}} > 0.01$ (as in, e.g., the white patch in the northern hemisphere of the rightmost panel). The outer domain edge is marked with a dashed line in the right panel, with the middle and left panels representing subsequent zoom-ins towards the inner radial edge of the domain.

As shown in Table 3.2, total mass ejection varies by $\sim 2-20\%$ between models with modified angular momentum and their fiducial models, with models with modified rotation profile always ejecting less unbound mass than the base models. This can be attributed in part to a loss of rotational support in the outermost layers of the progenitor star when modifying $j(M)$, which makes these layers more gravitationally bound and harder to eject.

In contrast to ejected mass, the kinetic energies of the ejecta from models with modified rotation are always larger than their unmodified counterparts. We can attribute this to the higher extraction of accretion energy per unit mass by material that sinks deeper into the gravitational potential of the BH when keeping r_{circ} constant instead of increasing with enclosed mass. This higher accretion efficiency in models with constant r_{circ} can be seen by the higher viscous heating relative to their baseline models in Figure 3.3.

As in Paper I, we define the asymptotic ejecta velocity using

$$\frac{1}{2}v_{\infty}^2 = \max(Be, 0), \quad (3.5)$$

with Be the Bernoulli parameter. The mass-averaged asymptotic velocities $\langle v_{\infty} \rangle$ from models with modified angular momentum profiles are higher than their base counterparts by $\sim 10-40\%$, leading to asymptotic kinetic energies higher by $\sim 30-60\%$. These increased asymptotic velocities of models with modified angular momentum still fall short of the velocities inferred from spectral line widths of Type Ic-BL SNe by a factor of $\sim 1.6-2$. Note that the disk outflow velocities may be further increased, relative to what we find here, through energy deposition by a relativistic jet, or through magnetic driving by large-scale magnetic fields. On the other hand, our ^{56}Ni masses are sufficient to power a typical type Ic-BL SN light curve. A detailed comparison with observational data requires proper radiative transfer calculations on ejecta from our models, which will be left for future work.

3.3.3 Analysis of the 19-Isotope Network Output

Inclusion of the 19-isotope network in the FLASH models (Sec. 3.2.1), supplemented by the NSE solver for $T > T_{\text{NSE}}$, provides mass fractions in every computational zone at each time step of the simulation, allowing for a detailed spatial and temporal nucleosynthesis analysis. Tables 3.3 to 3.6 show the mass ejected in various isotopes, along with their mass-weighted asymptotic velocities $\langle v_\infty \rangle$. All models produce several solar masses of ^{16}O ($3 - 8M_\odot$), the most abundant element in the ejecta, followed by ^{12}C ($1 - 2M_\odot$), ^{20}Ne ($0.4 - 2M_\odot$), and ^{56}Ni ($0.3 - 2M_\odot$). Other isotopes in the network have yields $< 1M_\odot$.

The ejected masses of ^{12}C , ^{16}O , and ^{20}Ne correspond to $\sim 50\%$ of their initial masses in the presupernova star, which proportionally tracks the ratio of total ejecta mass to initial presupernova mass, which is also $\sim 50\%$. Thus, we expect the majority of these elements to come from stellar layers ejected without much reprocessing. In contrast, the mass in ^4He is $\sim 140\%$ of the helium mass in the initial progenitor, thus collapsars are net producers of this element.

Similarly, while initial ^{56}Ni masses are negligible in the presupernova stars ($\sim 10^{-12} M_\odot$), our models produce $\sim 0.3 - 2.0 M_\odot$. Previous steady-state work on ^{56}Ni production in collapsar disk winds finds a dependence on the entropy and expansion time of the outflow Surman et al. (2011). The ^{56}Ni masses we see are consistent with the lower expansion velocity models of Surman et al. (2011), given our accretion rates ($\sim 0.2 - 0.5 M_\odot \text{ s}^{-1}$) and the mass weighted entropy per baryon of our outflows (Table 3.7). For models with the same progenitor star, we find some correlation between the ejected ^{56}Ni mass (Table 3.6) and the average asymptotic velocity of the outflow (Table 3.7), but not with the average entropy.

Figure 3.6 shows the angle-averaged mass fraction of selected isotopes within unbound material, as a function of enclosed mass, for models 16TI_SFHo and 350C_SFHo. The ejecta is well-mixed in Lagrangian mass coordinate, with most isotopes having

a gradual stratification in radius. It is notable that ^{56}Ni is present in most of the ejecta, with even an enhanced mass fraction in the outermost mass shells in model 16TI_SFHo. The angle-averaged velocity profile is consistent with Fig. 3.5, with most of the ejecta mass having velocity $\sim 0.03c \simeq 10,000 \text{ km s}^{-1}$. Previous work investigating mixing in collapsar disk winds finds higher mixing efficiency with longer wind duration Barnes & Duffell (2023), our models support this conclusion.

Figure 3.7 shows histograms of the mass in individual isotopes as a function of asymptotic velocity v_∞ , for models 16TI_SFHo and model 350C_SFHo. Again, we see that the ejecta is well mixed, with light (e.g., ^{12}C) and heavy (e.g., ^{56}Ni) elements spanning the entire range of expansion velocities. There is a slight preference for heavier isotopes being ejected with faster velocities and lighter isotopes with slower velocities (Tables 3.3 to 3.6). The width of the asymptotic velocity distribution is broader for the 16TI_SFHo model, with more mass ejected at higher velocities, while 350C_SFHo tends to have a narrower distribution with less material ejected at the highest speeds. The mass weighted averages $\langle v_\infty \rangle$ for each model are $\sim 2 - 3$ times smaller than those implied by the width of spectral features seen in type Ic-bl spectra Modjaz et al. (2016), however we see that some fraction of the ejected isotopes reach asymptotic velocities in excess of $20,000 \text{ km s}^{-1}$.

Figure 3.8 shows the spatial distribution of ^{16}O , ^{44}Ti , and ^{56}Ni in the ejecta from model 16TI_SFHo at the end of the simulation. Both ^{44}Ti and ^{56}Ni are largely co-spatial, produced in the expanding turbulent post-shock region, with ^{44}Ti found somewhat deeper into the ejecta than ^{56}Ni . ^{16}O makes up the largest fraction of the ejecta, and is distributed mostly uniformly. The fact that ^{44}Ti has a long radioactive decay timescale and is spatially stratified offers favorable prospects to observationally probe a galactic collapsar remnant with hard X-rays, as done with the CCSN remnant Cas A (e.g., Grefenstette et al. (2014)), in addition to more traditional gamma-ray spectroscopy diagnostics (e.g., Prantzos (2004); Thielemann et al. (2018)).

Figure 3.9 shows the evolution of the unbound ^{44}Ti and ^{56}Ni masses, as well as their

ratio, in each model. The ^{44}Ti masses are clustered by progenitor, with models based on 350C producing $\sim 3 \times 10^{-2} M_{\odot}$ within ~ 80 s post bounce, while models based on 16TI are clustered around $5 \times 10^{-3} - 10^{-2} M_{\odot}$, with a non-uniform production timescale. The production of ^{56}Ni is much more sensitive to model variations. In all of our models we see a super-solar $^{44}\text{Ti}/^{56}\text{Ni}$ mass ratio, spanning the range $4 \times 10^{-3} - 2.6 \times 10^{-2}$, which is 4 to 26 times higher than the solar mass ratio⁴ of $^{44}\text{Ca}/^{56}\text{Fe}$ ($\simeq 1.1 \times 10^{-3}$). This is an expected outcome of high explosion energies, which result in nuclear burning at lower densities than in normal CCSNe, enhancing α -rich freezeout products Nomoto (2017). In absolute terms, our models also overproduce ^{44}Ti relative to typical values obtained in CCSNe models (e.g., Sieverding et al. (2023); Wang & Burrows (2024)).

⁴We obtain the solar mass fraction of $^{44}\text{Ca}/^{56}\text{Fe}$ using solar elemental abundances from Scott et al. (2015b,a) and isotopic fractions from Meija et al. (2016).

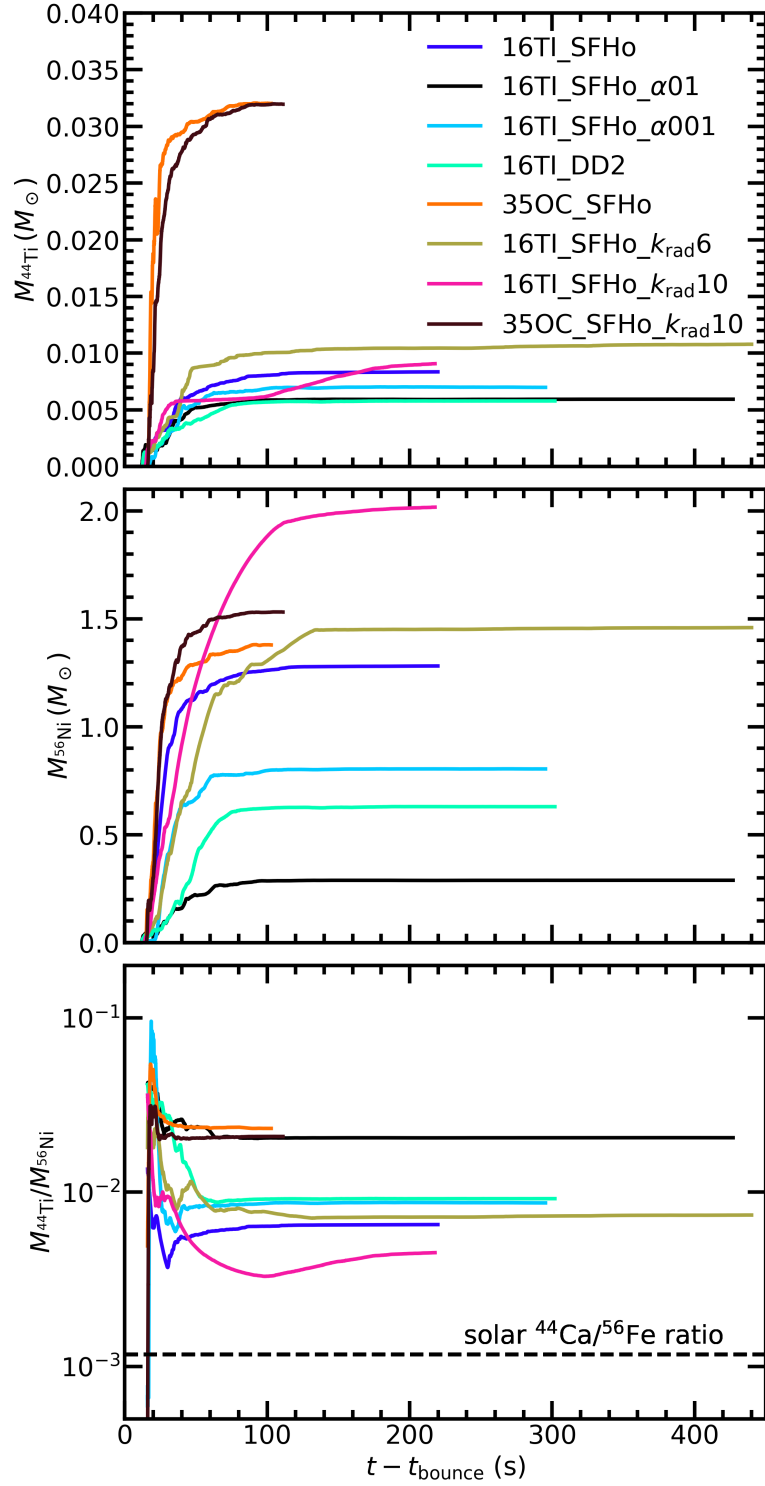


Figure 3.9: Evolution of the unbound mass in ^{44}Ti (top) and ^{56}Ni (middle), as well as their ratio $M_{^{44}\text{Ti}}/M_{^{56}\text{Ni}}$ (bottom), for all of our models. Also shown is the solar mass ratio of $^{44}\text{Ca}/^{56}\text{Fe}$ (dashed line), corresponding to the endpoints of the ^{44}Ti and ^{56}Ni decay chains, respectively, for reference. The bottom panel shows data for $t - t_{\text{bounce}} > 16$ s, to improve visibility.

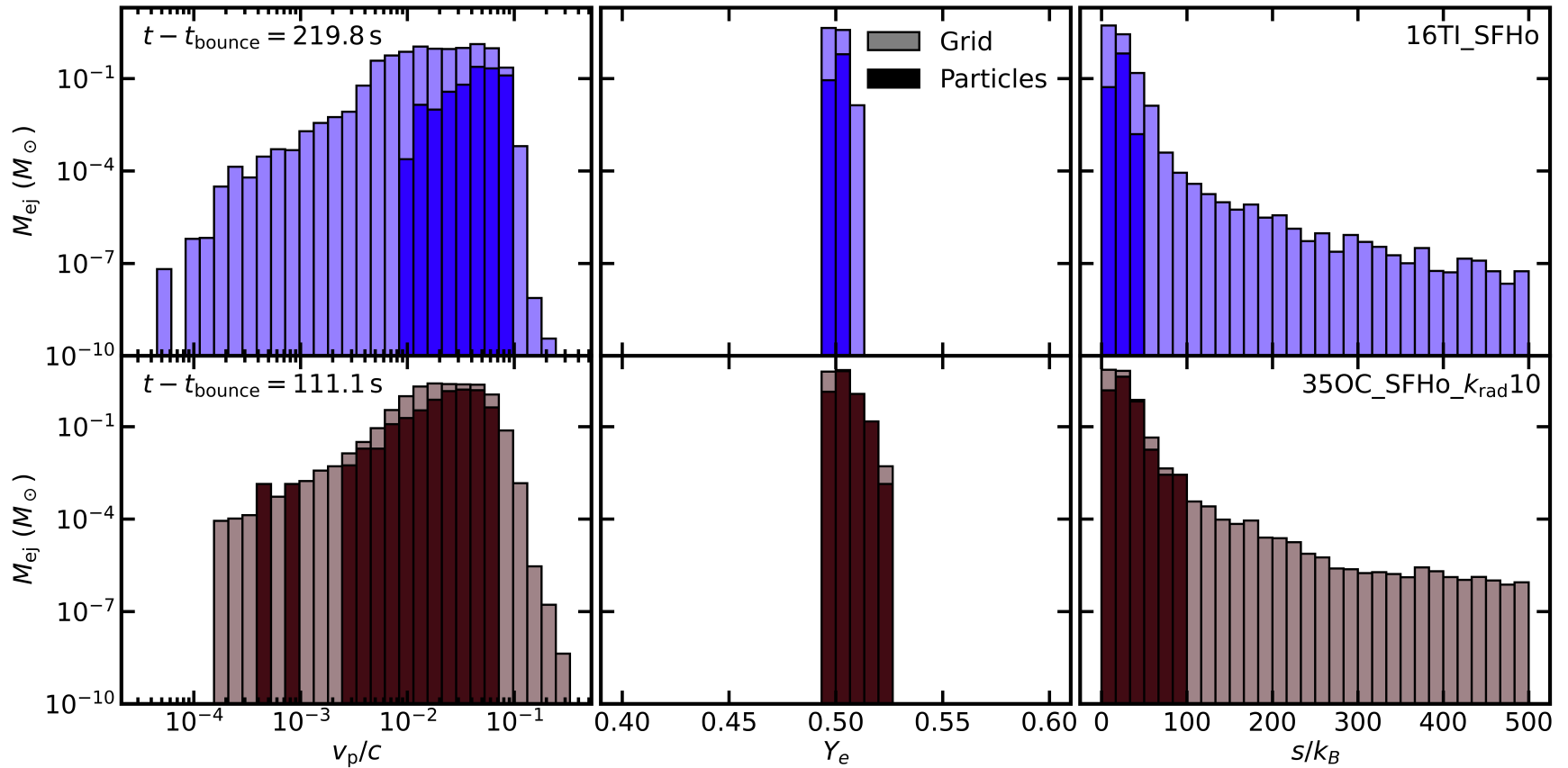


Figure 3.10: Unbound mass histograms binned by poloidal velocity (left), electron fraction (middle), and entropy per baryon (right), for selected models. Light colors show results calculated by integrating unbound matter over the grid at the end of the simulation, and dark colors show values obtained from unbound tracer particles which reach $T_{\text{max}} > 1$ GK, remaining in the domain at the end of the simulation, illustrating the level of sampling of the ejecta by the particles.

3.3.4 Nucleosynthesis in Post-Processing

The tracer particles swept up by the shock wave that remain in the outflow in the simulations presented here and in Paper I, sample the inner neutrino-reprocessed, turbulent region of the post shock region (Fig. 3.1, right panel). Figure 3.10 compares the unbound ejecta distribution obtained by volume-integrating across the grid, and by adding up the mass in tracer particles in selected models, illustrating the sampling of the total ejecta by particles. Sampling is incomplete, with particles accounting for a fraction $\sim 1 - 45\%$ of the total unbound ejecta mass, depending on the model. Tracer particles tend to sample the peak of the ejecta distribution in velocity, electron fraction, and entropy, resulting in mass-weighted average asymptotic velocities similar or larger than the value calculated from the grid, in all but the 16TI_DD2 model (Table 3.7). The average electron fraction obtained from the particles and from the grid are very similar, owing to the narrow electron fraction distribution, and the average entropies sampled by the particles are higher in all models relative to the values from the grid.

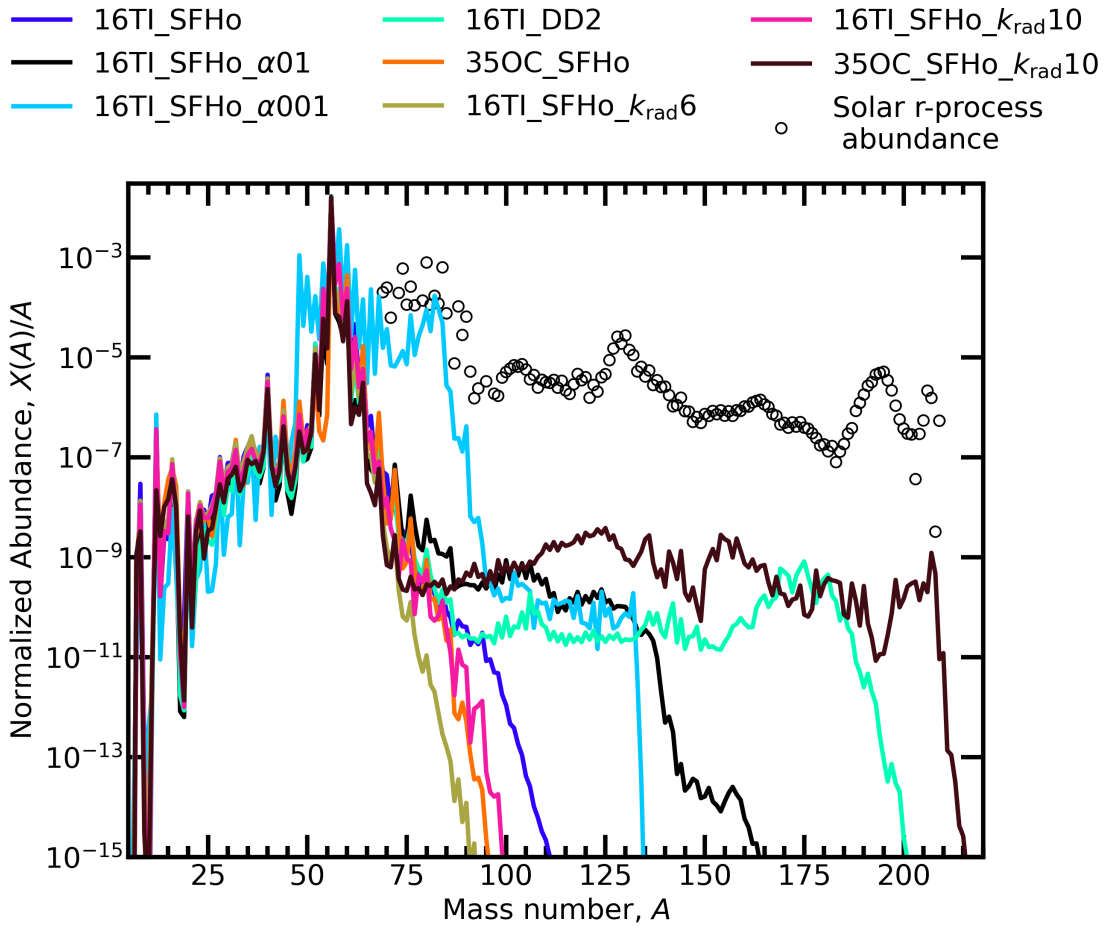


Figure 3.11: Isotopic abundances at 30 years from tracer particles evolved with SkyNet, for all models, as labelled. Abundances are obtained by dividing the isotopic mass fraction $X(A)$ by the mass number A , with the mass fractions adding up to unity. Open circles show the solar r -process abundance distribution from Goriely (1999), scaled to the first r -process peak ($A = 82$) from model 16TI_SFHo_alpha001, for reference.

Table 3.3: Ejecta masses and mass-weighted average asymptotic velocities of selected isotopes from the 19-isotope nuclear network, for all models. Ejecta masses are given in units of M_{\odot} , and asymptotic velocities in units of 10^3 km s^{-1} . ^1H ejecta mass and asymptotic velocity include a combination of p^+ and ^1H from the nuclear network.

Model	^1H		^4He		^{12}C		^{14}N	
	M_{ej}	$\langle v_{\infty} \rangle$	M_{ej}	$\langle v_{\infty} \rangle$	M_{ej}	$\langle v_{\infty} \rangle$	M_{ej}	$\langle v_{\infty} \rangle$
	(M_{\odot})	(km s^{-1})	(M_{\odot})	(km s^{-1})	(M_{\odot})	(km s^{-1})	(M_{\odot})	(km s^{-1})
16TI_SFHo	5.3×10^{-3}	1.7×10^4	4.6×10^{-1}	9.4×10^3	1.2	6.2×10^3	1.3×10^{-3}	7.4×10^3
16TI_SFHo_α01	5.3×10^{-4}	5.4×10^3	3.9×10^{-1}	5.8×10^3	1.4	5.3×10^3	1.5×10^{-3}	4.6×10^3
16TI_SFHo_α001	1.5×10^{-3}	1.1×10^4	4.3×10^{-1}	6.2×10^3	1.3	5.0×10^3	1.1×10^{-3}	5.9×10^3
16TI_DD2	2.0×10^{-3}	6.2×10^3	4.3×10^{-1}	6.7×10^3	1.5	6.1×10^3	1.2×10^{-3}	4.7×10^3
350C_SFHo	3.3×10^{-2}	9.6×10^3	5.0×10^{-1}	9.3×10^3	1.7	8.4×10^3	3.4×10^{-3}	7.0×10^3
16TI_SFHo_k_rad6	1.5×10^{-2}	1.8×10^4	6.0×10^{-1}	1.3×10^4	1.1	8.8×10^3	4.8×10^{-4}	1.4×10^4
16TI_SFHo_k_rad10	7.5×10^{-3}	1.5×10^4	6.1×10^{-1}	1.3×10^4	1.1	9.6×10^3	4.7×10^{-4}	1.1×10^4
350C_SFHo_k_rad10	4.5×10^{-2}	1.3×10^4	5.3×10^{-1}	1.1×10^4	1.6	8.4×10^3	3.2×10^{-3}	8.6×10^3

Table 3.4: Continuation of Table 3.3.

Model	¹⁶ O		²⁰ Ne		²⁴ Mg		²⁸ Si	
	M_{ej}	$\langle v_{\infty} \rangle$	M_{ej}	$\langle v_{\infty} \rangle$	M_{ej}	$\langle v_{\infty} \rangle$	M_{ej}	$\langle v_{\infty} \rangle$
	(M_{\odot})	(km s^{-1})	(M_{\odot})	(km s^{-1})	(M_{\odot})	(km s^{-1})	(M_{\odot})	(km s^{-1})
16TI_SFHo	4.0	6.9×10^3	6.3×10^{-1}	7.5×10^3	1.2×10^{-1}	8.5×10^3	2.2×10^{-1}	1.1×10^4
16TI_SFHo_α01	5.5	4.7×10^3	1.1	4.3×10^3	1.7×10^{-1}	4.3×10^3	7.4×10^{-2}	4.9×10^3
16TI_SFHo_α001	4.1	5.2×10^3	6.9×10^{-1}	5.7×10^3	1.1×10^{-1}	6.0×10^3	1.3×10^{-1}	8.0×10^3
16TI_DD2	5.3	5.3×10^3	9.6×10^{-1}	4.7×10^3	1.4×10^{-1}	4.6×10^3	1.3×10^{-1}	6.6×10^3
350C_SFHo	8.4	7.3×10^3	2.1	7.3×10^3	4.0×10^{-1}	7.8×10^3	1.8×10^{-1}	9.2×10^3
16TI_SFHo_k_rad6	3.1	1.0×10^4	4.3×10^{-1}	1.2×10^4	8.9×10^{-2}	1.3×10^4	1.1×10^{-1}	1.6×10^4
16TI_SFHo_k_rad10	3.3	9.7×10^3	5.3×10^{-1}	1.0×10^4	1.0×10^{-1}	1.1×10^4	1.1×10^{-1}	1.4×10^4
350C_SFHo_k_rad10	7.7	7.9×10^3	1.9	7.8×10^3	4.1×10^{-1}	8.7×10^3	2.5×10^{-1}	1.2×10^4

Table 3.5: Continuation of Table 3.3-3.4

Model	^{32}S		^{36}Ar		^{40}Ca		^{44}Ti	
	M_{ej}	$\langle v_{\infty} \rangle$						
	(M_{\odot})	(km s^{-1})	(M_{\odot})	(km s^{-1})	(M_{\odot})	(km s^{-1})	(M_{\odot})	(km s^{-1})
16TI_SFHo	1.2×10^{-1}	1.2×10^4	3.5×10^{-2}	1.2×10^4	4.5×10^{-2}	1.2×10^4	8.4×10^{-3}	1.3×10^4
16TI_SFHo_α01	3.2×10^{-2}	4.8×10^3	1.4×10^{-2}	4.9×10^3	2.1×10^{-2}	5.0×10^3	5.9×10^{-3}	5.1×10^3
16TI_SFHo_α001	7.8×10^{-2}	8.3×10^3	2.6×10^{-2}	8.4×10^3	3.4×10^{-2}	8.2×10^3	7.0×10^{-3}	8.2×10^3
16TI_DD2	7.7×10^{-2}	7.1×10^3	2.4×10^{-2}	6.8×10^3	3.1×10^{-2}	6.5×10^3	5.8×10^{-3}	5.3×10^3
350C_SFHo	8.9×10^{-2}	9.4×10^3	5.1×10^{-2}	9.4×10^3	8.0×10^{-2}	9.4×10^3	3.2×10^{-2}	9.6×10^3
16TI_SFHo_k_rad6	5.1×10^{-2}	1.7×10^4	2.0×10^{-2}	1.6×10^4	3.4×10^{-2}	1.6×10^4	1.1×10^{-2}	1.6×10^4
16TI_SFHo_k_rad10	5.1×10^{-2}	1.4×10^4	2.0×10^{-2}	1.4×10^4	3.2×10^{-2}	1.4×10^4	9.1×10^{-3}	1.4×10^4
350C_SFHo_k_rad10	1.1×10^{-1}	1.2×10^4	4.7×10^{-2}	1.2×10^4	8.2×10^{-2}	1.2×10^4	3.2×10^{-2}	1.2×10^4

Table 3.6: Continuation of Table 3.3-3.5

Model	⁴⁸ Cr		⁵² Fe		⁵⁴ Fe		⁵⁶ Ni	
	M_{ej}	$\langle v_{\infty} \rangle$						
	(M_{\odot})	(km s^{-1})	(M_{\odot})	(km s^{-1})	(M_{\odot})	(km s^{-1})	(M_{\odot})	(km s^{-1})
16TI_SFHo	4.7×10^{-3}	1.3×10^4	4.9×10^{-3}	1.4×10^4	2.6×10^{-2}	1.6×10^4	1.3	1.6×10^4
16TI_SFHo_α01	3.2×10^{-3}	5.1×10^3	2.5×10^{-3}	5.0×10^3	2.7×10^{-4}	4.4×10^3	2.9×10^{-1}	5.0×10^3
16TI_SFHo_α001	3.7×10^{-3}	8.3×10^3	2.7×10^{-3}	9.6×10^3	2.0×10^{-1}	8.1×10^3	8.1×10^{-1}	1.0×10^4
16TI_DD2	3.1×10^{-3}	5.4×10^3	3.8×10^{-3}	6.9×10^3	7.5×10^{-4}	5.6×10^3	6.3×10^{-1}	7.0×10^3
350C_SFHo	1.5×10^{-2}	9.6×10^3	8.0×10^{-3}	9.5×10^3	9.5×10^{-4}	7.8×10^3	1.4	9.4×10^3
16TI_SFHo_k_rad6	6.1×10^{-3}	1.6×10^4	5.7×10^{-3}	1.7×10^4	4.5×10^{-2}	1.9×10^4	1.5	1.8×10^4
16TI_SFHo_k_rad10	4.9×10^{-3}	1.4×10^4	5.5×10^{-3}	1.4×10^4	9.2×10^{-3}	1.4×10^4	2.0	1.7×10^4
350C_SFHo_k_rad10	1.8×10^{-2}	1.2×10^4	1.4×10^{-2}	1.2×10^4	8.7×10^{-4}	8.0×10^3	1.5	1.3×10^4

Table 3.7: Summary of tracer particle sampling of the ejecta. Columns from left to right show the number of unbound particles at the end of the simulation with $T_{\max} > 1$ GK (all models are initialized with 10^4 particles), total mass in unbound particles at the end of the simulation, total ejecta mass integrated from the grid, ratio of the mass in unbound particles to total ejecta mass (sampling percentage), mass-weighted average asymptotic velocity obtained from the particles and from the grid, mass-weighted average electron fraction from the particles and from the grid, and mass-weighted average entropy per baryon from the particles and grid, respectively.

Model	$N_{\text{part,ej}}$	$M_{\text{ej,part}}$ (M_{\odot})	M_{ej} (M_{\odot})	Sampling (%)	$\langle v_{\infty} \rangle_{\text{part}}$ (10^3 km s^{-1})	$\langle v_{\infty} \rangle_{\text{grid}}$ (10^3 km s^{-1})	$\langle Y_e \rangle_{\text{part}}$	$\langle Y_e \rangle_{\text{grid}}$	$\langle s/k_B \rangle_{\text{part}}$	$\langle s/k_B \rangle_{\text{grid}}$
16TI_SFHo	5846	0.7	8.2	8.6	1.6	8.7	0.50	0.50	23.8	14.6
16TI_SFHo_α01	6349	0.8	9.0	8.7	5.3	4.8	0.50	0.50	15.5	10.7
16TI_SFHo_α001	2096	0.3	7.9	3.3	7.6	6.0	0.49	0.50	17.5	12.4
16TI_DD2	5160	0.7	9.2	7.3	4.3	5.6	0.50	0.50	15.6	11.0
350C_SFHo	716	0.2	15.1	1.2	9.5	7.7	0.51	0.50	25.1	14.8
16TI_SFHo_ $k_{\text{rad}}6$	2881	0.3	7.0	4.8	1.2	1.2	0.50	0.50	25.4	23.5
16TI_SFHo_ $k_{\text{rad}}10$	4595	0.5	7.9	6.9	1.2	1.2	0.50	0.50	24.6	19.9
350C_SFHo_ $k_{\text{rad}}10$	4636	6.4	14.3	44.8	8.6	8.7	0.50	0.50	22.9	17.8

Figure 3.11 shows isotopic abundances from tracer particles evolved with `SkyNet`. As expected from the electron fraction distribution of the unbound ejecta being narrowly peaked around $Y_e = 0.5$ (Fig. 3.5), abundances are dominated by the iron group ($A \sim 50 - 60$), with steeply decreasing abundances for lighter and heavier elements, in a similar way as abundances from successful CCSNe (e.g., Janka & Bauswein (2023)). The two base models `16TI_SFHo` and `350C_SFHo`, as well as the `16TI` models with modified rotation `16TI_SFHo_krad6` and `16TI_SFHo_krad10` do not produce any significant amount of elements beyond the iron group.

The low-viscosity model `16TI_SFHo_α001` (Paper 1) stands out as the only one that produces significant amounts of first r -process peak ejecta, with abundances decreasing sharply for heavier elements. This model produced the most neutron-rich ejecta of our entire simulation set. The dependence of the Y_e distribution on the strength of viscous angular momentum transport (also found by Just et al. (2022a)) implies that the production of (at least) light r -process elements will also be sensitive to the character of angular momentum transport in the disk. This indicates that nucleosynthesis results from 3D GRMHD simulations that include the relevant physics will likely differ in their exact abundance pattern relative to viscous hydrodynamic models like those presented here.

There is still some production of small amounts of heavy elements. Models `16TI-DD2` and `16TI_SFHo_α001`, produce elements beyond $A = 130$, and model `350C_SFHo_krad10` yields a small abundance of elements up to and beyond $A = 200$. None of the abundance patterns has an overall similarity to that of the r -process, although the undersampling of the ejecta by particles and the small amounts of elements heavier than the iron group do not allow us to make definitive statements about global abundance patterns from collapsar disk outflows.

While the ratio of r -process peak elements to the iron peak (e.g., Burbidge et al. (1957)) is underproduced by a factor $10^1 - 10^3$ in models that produce the heaviest elements, the ratio of first r -process peak to iron is higher by a factor 100 in the low-

viscosity model 16TI_SFHo_α001. This suggests that small variations in the evolution of collapsars can lead to an intrinsic scatter in the abundance pattern of ejected material, particularly for $A \sim 80$.

Our tracer particle abundances at 30yr show production of stable isotopes on both the proton-rich and neutron-rich sides of the valley of stability (Figure 3.12), suggesting the possibility of neutron- and proton captures occurring in some part of the outflow. Further investigation shows that heavy element production in models such as 16TI_DD2 and 350C_SFHo_ $k_{\text{rad}}10$ occurs via the rp -process Wallace & Woosley (1981), building up elements via proton capture in a small number of tracer particles that sample fluid with an excess of free protons. Figure 3.13 shows the rapid buildup of heavy elements in one of the tracer particles from model 16TI_DD2 that reaches $A \sim 200$, which evolves on the proton rich side of the valley of stability on a timescale of ~ 1 s. This evolution in the (N, Z) -plane corresponds to a spike in the electron fraction (reaching $Y_e \sim 0.9$) into the proton-rich side, and a spike in the entropy (reaching $s/k_B \sim 80$) (Figure 3.13).

Nucleosynthesis proceeds with alternating proton captures and β^+ decays up to $Z = 50$ near the $Z = N$ line. Ref. Schatz et al. (1997) showed that waiting points, corresponding to the nuclear magic numbers along the proton drip line, create the need for several successive β^+ -decays before further proton captures may be bridged by net proton capture, within a window of temperature $T \sim 1 - 2$ GK, for densities $\rho \sim 10^6 - 10^7 \text{ g cm}^{-3}$. However, these thermodynamic ranges strongly depend on the nuclear Q -values for certain proton capture reactions, which are not known experimentally. Nonetheless, this phenomenon may explain the ability of these few trajectories to exceed these waiting points. Thereafter, nucleosynthesis proceeds at a shallower angle across the (N, Z) -plane, towards- and eventually across the valley of stability, likely due to (α, p) reactions on rp -process nuclei, similar to those described in Wallace & Woosley (1981).

For completeness, we note that out of the particles producing heavy elements via

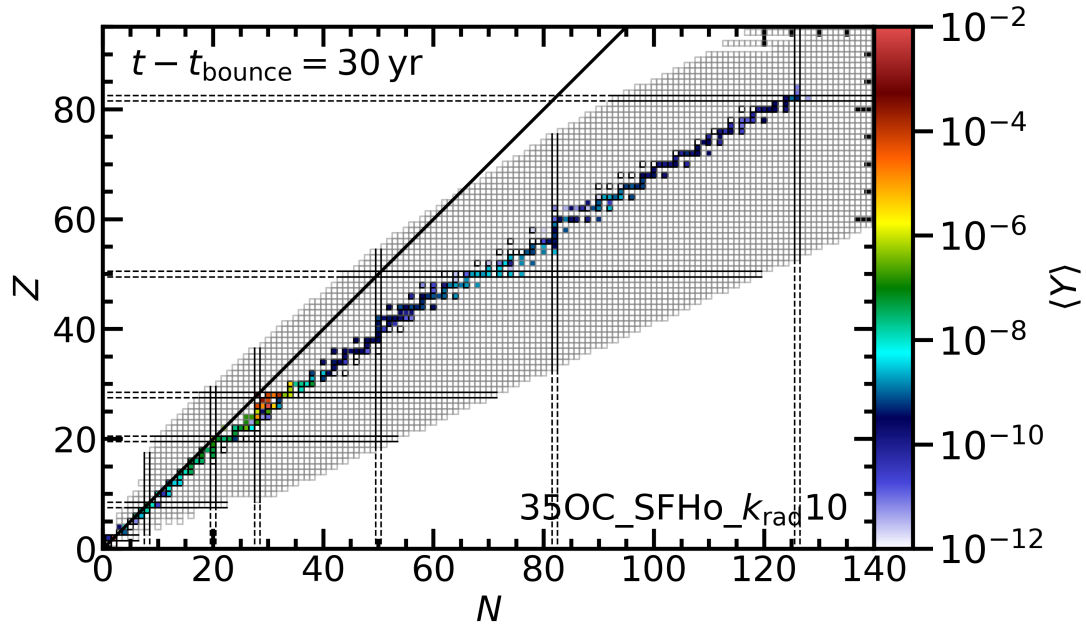


Figure 3.12: Average abundance $\langle Y \rangle$ of isotopes on the (N, Z) -plane, 30 years post-bounce, as evolved in SkyNet for model 350C_SFHo_ $k_{\text{rad}}10$. The final abundance of each simulation is an average over the particle abundances, weighted by the number of baryons. Isotopes evolved in SkyNet are marked with grey boxes, stable isotopes (IAE, 2023) are marked with black squares. Closed proton shells (corresponding to magic numbers 2, 8, 20, 28, 50, 82, and 126) are marked with horizontal black lines, and closed neutron shells are marked with vertical black lines. The diagonal black line marks equal number of protons and neutrons in an isotope.

the rp -process, only one does not exceed our fiducial NSE transition temperature of 5 GK during its evolution. Nevertheless, that particle starts its SkyNet evolution in NSE from its maximum temperature of 4.7 GK, very close to the fiducial NSE temperature for the vast majority of post-processed particles.

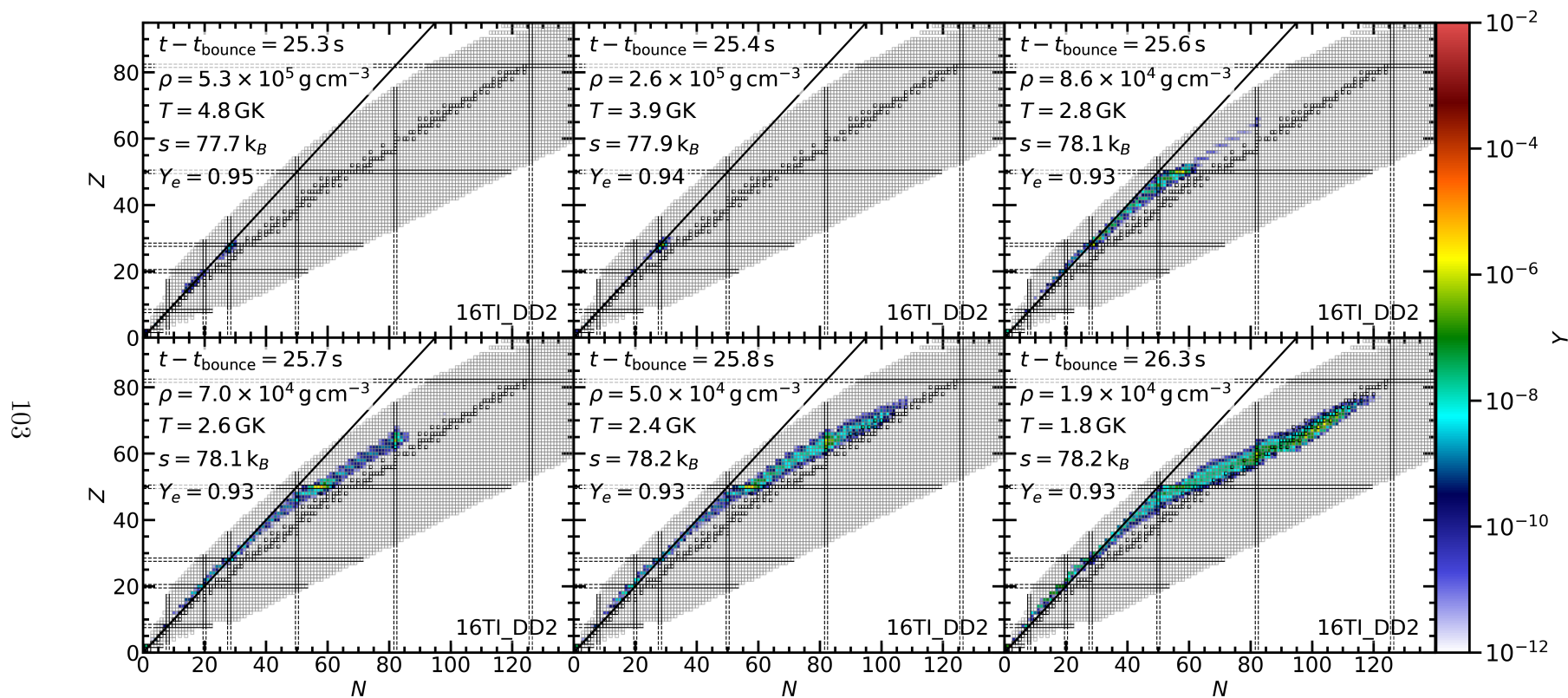


Figure 3.13: Time evolution of abundances on the (N, Z) -plane for the particle that produces the heaviest isotopes in model 16TI_DD2 (Fig. 3.11). The temperature, electron fraction (from SkyNet) and entropy per baryon of the tracer particle at each time are shown in each panel.

3.3.5 Optimal Initial Tracer Particle Placement

The undersampling of the ejecta by tracer particles given our procedure for initial placement motivates a brief discussion on how to improve this procedure in future collapsar simulations. As discussed in Section 3.2.2, particles are initialized in the domain pseudo-randomly between two radial bounds at the time of disk formation. Despite the formation of the shocked disk, accretion onto the BH continues predominantly through low density funnels near the poles during the first few seconds after disk formation. After the onset of shock expansion, significant accretion can continue through one hemisphere as the shock expands into the other. Of the initial 10^4 tracer particles placed in each of our simulations, 37 – 93% are lost to accretion onto the BH. Which pole the shock wave expands into is not known a priori, and is set by the instability to axisymmetric perturbations as discussed in Paper I. Figure 3.1 illustrates this point for model 16TI_SFHo, showing particles which are accreted onto the BH (white dots) and those that make their way into the outflow (black dots).

The radial range initially chosen is intended to maximize the presence of particles in the disk for the NDAF phase, during which the entirety of neutronization occurs (e.g., Paper I) and NSE is reached or closely approached, simplifying the handling of initial conditions for the post-processing nuclear reaction network. We choose the radial range for particle placement in our models by setting the free-fall timescale t_{ff} (as an estimate of the time it takes a particle to undergo infall and joining the disk) equal to the duration of the NDAF phase τ_{NDAF} , yielding a radius

$$\begin{aligned} R_{\text{ff}} &= [GM_{\text{BH}}(t_{\text{df}})\tau_{\text{NDAF}}^2]^{1/3} \\ &\simeq 10^9 \text{ cm} \left(\frac{M_{\text{BH}}(t_{\text{df}})}{3M_{\odot}} \right)^{1/3} \left(\frac{\tau_{\text{NDAF}}}{2 \text{ s}} \right)^{2/3}, \end{aligned} \quad (3.6)$$

where $M_{\text{BH}}(t_{\text{df}})$ is the lower limit to the BH mass when the disk is present. In most models, particles are initialized in the radial range $r = 1.5 \times 10^6 - 3 \times 10^9$ cm.

Since outflows with the best chance of producing the conditions for the r -process originate during the NDAF phase, a better sampling of this outflow component re-

quires more particles within $r \lesssim R_{\text{ff}}$, given that the vast majority of these particles are lost to accretion, leaving only a very small percentage of the particles in the outflow. Better sampling of the entirety of the ejecta, particularly during the ADAF phase, requires increasing the outer radial limit for particle initialization. This, however, can run into memory limitations if too many particles are required for reasonable resolution in mass, and also results in many particles never reaching NSE or even the explosive nucleosynthesis regime, introducing a dependence on the initial abundance of the stellar progenitor and on how many isotopes are tracked in the hydrodynamic evolution (in our analysis, we discard particles that never exceed 1 GK).

3.3.6 Comparison to previous work

Nucleosynthesis in collapsars has been explored previously along two major branches: nucleosynthesis in jets, and in disk winds. While the inner accretion disk is capable of reaching the densities and temperatures needed for significant neutronization ($Y_e < 0.25$) as needed for the production of heavy r -process elements, the question of whether that material makes its way into the outflow remains unsettled.

Ref. Pruet et al. (2003) examines neutronization of the accretion disk based on the steady state solutions of Popham et al. (1999), and argues, based on the expansion velocity of the jet, that r -process nucleosynthesis is possible. Varying the accretion rate and viscosity in the disk, they solve for the evolution of the electron fraction as governed by neutrino emission and absorption. In some models, disk material is significantly neutronized ($Y_e < 0.25$), with the jet seen as a promising site for the production of r -process elements due to the high expansion speeds, allowing for the low electron fraction to be frozen out when ejected. Additionally, the disk wind is seen as a potentially larger source of r -process elements than the jet, if the entropy is higher than that seen in the center of the disk. Nevertheless, this work suggests that neutronization of the disk occurs primarily in at the inner radial edge in the mid-plane, making it very difficult for highly neutronized material to make its way

into the outflow.

Nucleosynthesis in collapsar jets was studied by Fujimoto et al. (2007) using tracer particles on the simulations of Fujimoto et al. (2006). The latter are axisymmetric, rotating MHD simulations with Newtonian gravity, with approximate neutrino effects, and produce magnetically-driven jets. Some particles reach electron fractions of $Y_e < 0.25$, and produce isotopes up to and beyond the third r -process peak. Additionally, the production of light and heavy p -nuclei are found as well, suggesting some proton richness to the outflow. The pseudo-Newtonian character of our simulation cannot produce a relativistic jet, and hence there is no direct comparison possible.

Ref. Ono et al. (2012) performed nucleosynthetic calculations based on the axisymmetric Newtonian MHD simulations of Ono et al. (2009), featuring collapsar jets. While the simulation only includes neutrino cooling, they too see sufficient neutronization to form elements up to the third r -process peak, but these third-peak elements are not significantly present in the final abundances. Similarly, Nakamura et al. (2013) performs axisymmetric relativistic MHD simulations of collapsar jets using a simplified neutrino scheme that is evolved on a coarser timescale than the hydrodynamics equations themselves. They also find that material in the jet reaches significant neutronization ($Y_e < 0.25$), and the production of r -process elements beyond the third peak.

More recently, nucleosynthesis in collapsar disk winds based on time-dependent 3D GRMHD simulations on a fixed Kerr metric and with a neutrino leakage scheme has been explored by Siegel et al. (2019), starting from equilibrium tori. Based on the assumption that the disk wind overpowers the ram pressure from the infalling stellar mantle, the disk is embedded within a uniform low density medium. They find that the production of r -process elements is possible in the disk wind, and is highly accretion rate dependent.

Ref. Siegel et al. (2019) evolve their accretion disk in MHD, resolving the magneto-rotational instability directly, while we use the approximate alpha viscosity prescrip-

tion of Shakura & Sunyaev (1973). BH accretion disk winds driven by an alpha viscosity prescription have been compared (in the context of NS mergers) to MHD disk outflows by Fernández et al. (2018), with ISCO accretion rates, and viscous outflow rates reproducing the MHD outflow well in the ADAF phase ($t \gtrsim 100$ ms), with variations appearing on short timescales after the onset of the outflow due to transients associated to the chosen initial magnetic field geometry. Additionally, Siegel et al. (2019) evolves their disk in a uniform low density medium, while our disk is formed self-consistently within the star, with outflows making their way through the infalling stellar mantle. The main difference between our two approaches, in terms of the electron fraction distribution of the ejecta, stems from the mass accretion rate at the time of the ejection of matter from the disk. In our models, we see the degenerate conditions that lead to the neutronization of material predominantly in the midplane of the disk, also seen by Siegel et al. (2019). However, the onset of mass ejection in our models does not occur until the transition to an ADAF phase, which corresponds to the end of neutronization of the disk. As a result, our outflowing material has electron fractions of $Y_e \sim 0.5$. The presence of a large-scale poloidal magnetic field, as well as the assumption of a uniform low density ambient medium in Siegel et al. (2019) allows for mass to be ejected earlier and with less resistance, leading to the ejection of material with $Y_e < 0.25$.

Ref. Janiuk (2019) performs 2D GRMHD simulations of BH accretion disk outflows with nucleosynthesis analysis. Like Siegel et al. (2019), they embed an equilibrium torus in a low-density medium surrounding a central BH, but only accounting for neutrino cooling and evolving for ~ 0.3 s. They find that early outflows originating in the first ~ 0.1 s may be composed of neutronized material varying in electron fraction from $\sim 0.2 - 0.35$, and through subsequent nucleosynthesis calculations, find the production of third peak r -process elements. Like with the simulations of Siegel et al. (2019), the main distinction with our models stems from neglecting the surrounding infalling stellar mantle and the presence of large-scale poloidal magnetic fields.

Ref. Miller et al. (2020) performs a similar 3D GRMHD simulation to that of Siegel et al. (2019), but using Monte Carlo neutrino transport and evolving the torus for ~ 150 ms. They obtain accretion rates that match the $0.1 M_{\odot} \text{ s}^{-1}$ of Siegel et al. (2019), which allow for significant neutrino cooling and thus neutronization. They find that there is no unbound material with electron fraction below $Y_e \sim 0.3$, however, and are thus unable to produce 3rd r -process peak elements. Additionally, they note that the assumption of neglecting the ram pressure from the infalling stellar mantle, as well as feedback effects from the jet, may have a significant effect on whether neutronized material is able to escape the star at all. Our results from Paper I support this conjecture.

Ref. Zenati et al. (2020) performs long-term (~ 100 s), axisymmetric, viscous hydrodynamic simulations of collapsar disks including the same 19-isotope nuclear network we use. Equilibrium tori, embedded in low-density atmospheres, are constructed to match the post-circularization state of several progenitors, assuming an angular momentum profile that varies as a radial power-law in the core. The state of these disks is intended to match later times relative to disk formation and the NDAF phase that follows. This is reinforced by the peak densities in their disks being $\mathcal{O}(10^2)$ times smaller than those in the disks from our most comparable progenitor (350C). Thus, they see disk outflows driven in the ADAF regime, with contributions from viscous and nuclear heating. Overall, our models eject more mass, and have higher explosion energies by roughly an order of magnitude, owing to the continual feeding of the accretion disk by the stellar mantle, which is not present in the models from Zenati et al. (2020). The ^{56}Ni mass range that they obtain ($[0.6 - 7.0] \times 10^{-3} M_{\odot}$) is also smaller than what we find by a factor $\gtrsim 100$.

3.4 Summary and Discussion

We have studied nucleosynthesis in the disk outflows from rapidly-rotating Wolf-Rayet stars that undergo core-collapse and form a BH accretion disk. We evolve the stars

from core-collapse to BH formation using a spherically-symmetric general relativistic neutrino radiation hydrodynamics code with approximate rotation effects. We then map into an axisymmetric viscous hydrodynamic code that includes Newtonian self-gravity and a pseudo-Newtonian potential for the BH, neutrino heating and cooling via a lightbulb-type scheme, and the Helmholtz EOS.

Simulations also include a 19-isotope nuclear reaction network, supplemented by an NSE solver for high temperatures, providing full temporal and spatial composition information for alpha chain and related elements. Additionally, we use passive tracer particles to sample neutrino-reprocessed matter, and post-process these trajectories with a large nuclear reaction network.

Our models capture the self-consistent formation of a shocked, neutrino-cooled accretion disk that transitions into an advective disk, within a collapsing star, following shock expansion until it breaks out from the stellar surface. The outflow from this disk is sufficiently energetic to explode the star. In Paper I, we reported on a first set of 5 simulations that vary the progenitor star, nuclear EOS used prior to BH formation, and strength of viscous angular momentum transport. In this follow-up paper, we carry out detailed nucleosynthesis analysis of the initial simulation set, and present additional models that modify the rotation profile of progenitor stars, to maximize the exposure of circularized shells to significant neutrino reprocessing and thus to neutronization, as an optimistic upper limit to the dependence of neutron-rich matter generation on stellar rotation.

Our main results are the following:

1. – The ejecta from all of our simulations is dominated by ^{16}O , of which several M_{\odot} are consistently produced. This is followed by ^{12}C , ^{20}Ne , and ^{56}Ni at $\sim 1 M_{\odot}$ each. All other elements of the 19-isotope network are produced at a $< 1M_{\odot}$ level (Tables 3.3-3.6). The ^{56}Ni masses are consistent with the observed range from Ic-BL SNe, while average asymptotic velocities are lower by a factor ~ 2 . The ejecta is well

mixed in mass and in velocity (Figs. 3.6-3.7), although spatial stratification of heavy elements is apparent (Fig. 3.8). Production of ^{44}Ti is super-solar (Fig. 3.9).

2. – Only one of our models, with the lowest viscosity, yields an outflow with sufficient neutrons to reach the first r -process peak in significant amounts. All other models produce very small or negligible amounts of elements beyond the iron group (Fig. 3.11). While the minimum electron fraction in the accretion disk drops to $Y_e < 0.25$ during the NDAF phase in all models, most of this material is near the central plane of the accretion disk, and is accreted onto the central BH, as reported in Paper I. The rapid expansion of the shock wave follows a transition to an ADAF phase with no additional neutronization (Figs. 3.3-3.4). Nevertheless, the fact that first r -process peak elements were produced due to a (small) change in viscosity suggests that an intrinsic scatter in abundances around $A \sim 80$ is expected due to variations between individual collapsar explosions in nature.

3. – A subset of our models produce small quantities of heavy elements (up to $A \sim 200$) via the rp -process and (α, p) reactions, in particles that sample proton-rich, high entropy ($s/k_B \sim 80$) ejecta (Figs. 3.12-3.13). While our tracer particles do not fully sample the entirety of the ejecta (Table 3.7), they trace matter that accretes into the disk during the NDAF phase and is thus subject to significant neutrino re-processing. Our results suggest that collapsar disk winds may exhibit the conditions necessary for the rp -process to act.

In addition to providing trajectories for nucleosynthesis analysis, our tracer particles show that while the most significant neutronization occurs in the midplane of the accretion disk near the BH, the majority of the disk outflow originates from the outer edge of the disk. Due to the ever-present central BH acting as a sink of matter in the center of the domain (Fig. 3.1), this material is easily accreted, and almost none of

the neutronized material makes its way into the outflow. The large fraction of tracer particles accreted into the BH in our simulations provides guidance on where in the star these initial tracers must be located for optimal sampling (Sec. 3.3.5).

The entropy per baryon of the ejected material covers a broad range, with mass ejected exceeding several hundred k_B . As our tracer particles only sample the low entropy end of the distribution, it is possible that some r -process elements are produced in this regime that were not sampled here. However, if the r -process indeed occurs in the high-entropy tail, the amount of mass produced must be relatively small compared to the rest of the ejecta (Fig. 3.5).

The modification of the angular momentum profile in the new models presented here (Fig. 3.2) had at most a modest effect on the duration of the NDAF phase, delaying disk formation and the transition to the ADAF phase, while only extending the NDAF phase appreciably in one model (Fig. 3.3). This did not lead to a significant change in the minimum electron fraction in the outflow (Fig. 3.4), and yielded only trace amounts of elements beyond the iron group in another model (350C_SFHo_ $k_{\text{rad}}10$; Fig. 3.11). We conclude that modification of the rotation profile alone cannot lead to the production of significant amounts of r -process elements in the context of viscous hydrodynamic evolution.

The picture might change if MHD effects, beyond those modeled by viscous hydrodynamics, become important. Experience from BH accretion disks formed in NS mergers shows that significant ejection of matter during the NDAF phase is possible, but highly sensitive to the initial magnetic field geometry of the disk, requiring a large-scale poloidal component to generate magnetically-driven outflows in excess of those due to dissipation of magnetorotational turbulence Christie et al. (2019); Fahlman & Fernández (2022b); Hayashi et al. (2023). Likewise, magnetorotational CCSNe simulations require strong, large-scale initial dipolar fields to reach the third r -process peak Nishimura et al. (2015); Mösta et al. (2018); Reichert et al. (2024); Zha et al. (2024). Like in NS mergers, magnetic winds would not only carry away

neutron-rich material, but would also be faster than outflows obtained in viscous hydrodynamics Fernández et al. (2019b), possibly ameliorating the velocity deficit of our ejecta relative to that inferred from Ic SNe spectra. A relativistic jet, likely magnetically-driven, can also contribute to speed up the disk outflow through energy deposition. Ultimately, whether these rapid, magnetically-driven outflows take place in collapsars will depend on the magnetic field geometry and strength in the presupernova star (Gottlieb et al., 2024).

Chapter 4

Additional Code development

This chapter contains calculations and code developed that were not described in detail in Chapter 2 or Chapter 3 (published as journal articles), but which took a non-trivial amount of time and are worth documenting.

4.1 Dynamic Computational Domain Boundaries

The collapsar setup has a logarithmically spaced radial grid extending from an inner bound r_{in} , which is placed between the horizon and the ISCO of the central BH at the beginning of the simulation, to an outer bound placed at ~ 2 times the radius of the progenitor star. In some models, the accretion onto the BH over the timescale of the simulation is sufficient for the BH horizon radius, which is proportional to the BH mass, to reach the fixed inner radial bound at some point in the simulation (this is a practical problem because the pseudo-Newtonian potential diverges at the horizon radius). For this reason, I needed to modify the computational domain at several points in the simulation. In order to do this, I developed a framework to modify the FLASH checkpoint files to have FLASH restart from a checkpoint file with a modified computational grid in order to move the inner radial bound, to keep it between the BH horizon and ISCO. To prevent numerical problems, we perform a domain shift when the inner radial bound falls below 130% of the event horizon radius. To reduce the number of restarts needed across the simulation time, we find the nearest cell

edge to a radius:

$$r_{\text{in,new}} \simeq 0.75(r_{\text{isco}} - r_{\text{h}}) + r_{\text{h}}, \quad (4.1)$$

which will become the new inner radial bound. To simplify the problem, and remove the need for interpolation, we excise an integer number of cells from the inner radial grid, and we keep constant the total number of radial cells, so we add an equal integer number of cells to the outer radial domain. All mass and angular momentum within the excised radial cells is considered to be instantaneously accreted onto the black hole, simply being integrated and added to the pseudo-Newtonian (Artemova) potential parameters. All hydrodynamic parameters, isotopic mass fractions, etc. are then shifted by an integer number of radial cell positions onto the new grid. The new radial cells added to the outside of the radial grid are filled with power-law decaying density and pressure, with slope consistent with the variable floors. An initial guess for the temperature of these cells is given by the assumption that the pressure in these cells is dominated by radiation pressure:

$$T_{\text{rad}} = \left(\frac{3P_{\text{rad}}}{a} \right)^{1/4} \quad (4.2)$$

where a is the radiation density constant (the actual temperature is then set by the EOS). The added fluid is assumed to be non-rotating ($j = 0 \text{ cm}^2 \text{ s}^{-1}$), composition is assumed to be consistent with the previous outer radial cells, and the added fluid is marked as atmospheric $X_{\text{atm}} = 1$ to prevent any fluid added from being included in outflow calculations. The remaining hydrodynamic variables are filled in by the first call to the equation of state upon restart of the simulation. Any tracer particles that are moved out of the computational domain by the radial domain shift are removed from the list of evolved particles in the same way as if they had crossed a grid boundary during regular evolution. An example domain shift is shown in Figure 4.1 illustrating differences in the grid structure at the inner and outer radial domain before and after a domain shift restart.

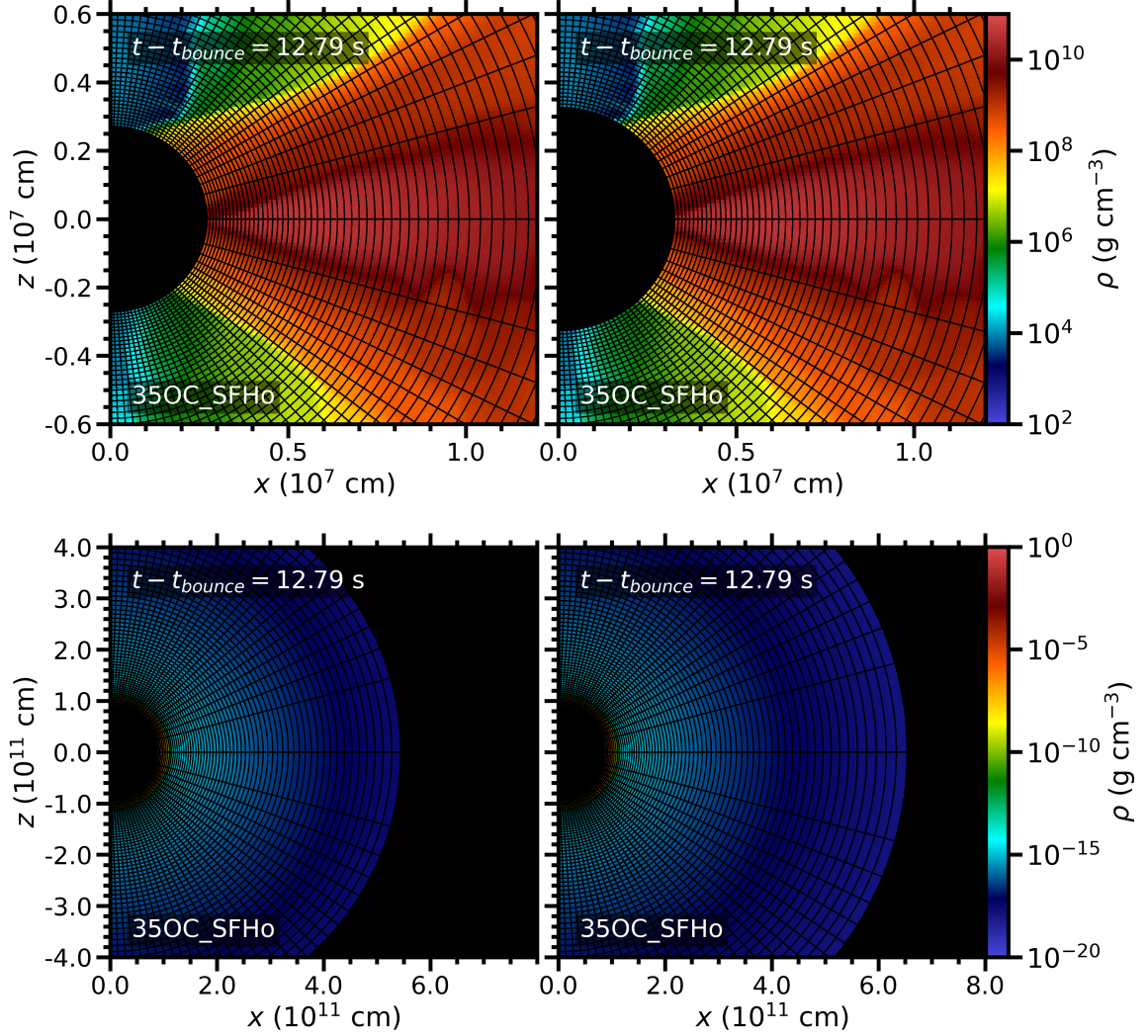


Figure 4.1: Snapshots of the density at the inner radial boundary (top row) and outer radial boundary (bottom row) before a domain shift (left column) and after the domain restart (right column) for the 350C_SFHo model. Every second radial and angular bin edge is marked with a black line to facilitate visibility near the inner radial edge. Twelve radial cells are removed from the inner edge by this domain restart, adding twelve radial cells to the outside domain thus keeping the total number of radial cells constant.

4.2 Numerical Stability of Neutrino Opacities

The neutrino opacities used in the leakage scheme are local quantities dependent on the temperature, density, mass fractions of neutrons and protons, and the electron degeneracy. Solving for the opacities depends on several ratios of the Fermi integrals for relativistic particles (Ruffert et al., 1996):

$$\mathcal{F}_k(\eta) = \int_0^\infty \frac{x'^k}{e^{x'-\eta} + 1} dx' \quad (4.3)$$

where \mathcal{F}_k is the k th Fermi integral, η is the degeneracy parameter $\mu_e/(k_B T)$, with μ_e the electron chemical potential, and x' is our integration variable. Due to numerical issues, the Fermi integral solver had been modified previously by Steven Fahlman to use an approximate form from Takahashi et al. (1978) (valid for $\eta \leq 10^{-3}$):

$$\begin{aligned} \mathcal{F}_1(\eta) &= e^\eta / [1 + 0.2159 \cdot \exp(0.8857\eta)] \\ \mathcal{F}_2(\eta) &= 2 \cdot e^\eta / [1 + 0.1092 \cdot \exp(0.8908\eta)] \\ \mathcal{F}_3(\eta) &= 6 \cdot e^\eta / [1 + 0.0559 \cdot \exp(0.9069\eta)] \\ \mathcal{F}_4(\eta) &= 24 \cdot e^\eta / [1 + 0.0287 \cdot \exp(0.9257\eta)] \\ \mathcal{F}_5(\eta) &= 120 \cdot e^\eta / [1 + 0.0147 \cdot \exp(0.9431\eta)] \\ &\vdots \\ \mathcal{F}_k(\eta) &= k! e^\eta / \left[1 + \left(\frac{k!}{\mathcal{F}_k(0)} - 1 \right) \cdot \exp(A) \right], \end{aligned} \quad (4.4)$$

where A is a constant. The solver switched to these approximate forms for $\eta < -500$.

In addition to these approximations, I had to introduce a transition to approximate forms of the Fermi integrals for high values of η . Also from Takahashi et al. (1978),

approximate forms of the Fermi integrals valid for $\eta > 10^{-3}$ are:

$$\begin{aligned}
\mathcal{F}_1(\eta) &= \frac{[\eta^2/2+1.6449]}{[1+\exp(-1.6855\eta)]} \\
\mathcal{F}_2(\eta) &= \frac{[\eta^3/3+3.2899\eta]}{[1-\exp(-1.8246\eta)]} \\
\mathcal{F}_3(\eta) &= \frac{[\eta^4/4+4.9348\eta^2+11.3644]}{[1+\exp(-1.9039\eta)]} \\
\mathcal{F}_4(\eta) &= \frac{[\eta^5/5+6.5797\eta^3+45.4576\eta]}{[1-\exp(-1.9484\eta)]} \\
\mathcal{F}_5(\eta) &= \frac{[\eta^6/6+8.2247\eta^4+113.6439\eta^2+236.5323]}{[1+\exp(-1.9727\eta)]} \\
&\vdots \\
\mathcal{F}_k(\eta) &= \frac{[\eta^{k+1}/(k+1)+\sum_{r=1}^{\lfloor(k+1)/2\rfloor} {}_2{}_k C_{2r-1} \eta^{k+1-2r} \mathcal{F}_{2r-1}(0)]}{[1-(-1)^k \exp(-2k\eta \mathcal{F}_{k-1}(0)/\mathcal{F}_k(0))]}
\end{aligned} \tag{4.5}$$

where

$${}_k C_{2r-1} = k! / [(2r-1)!(k-2r+1)!] \tag{4.6}$$

and

$$[(k+1)/2] = \begin{cases} (k+1)/2 & \text{for odd- } k \\ k/2 & \text{for even- } k \end{cases} . \tag{4.7}$$

The solver had numerical issues for large values of η ($\eta > 20$). For example, for $k = 2$, we have $e^{-k\eta} \lesssim 4 \times 10^{-18}$. Thus we can simplify:

$$1 + e^{-k\eta} \rightarrow 1. \tag{4.8}$$

Which simplifies the integrals to:

$$\begin{aligned}
\mathcal{F}_1(\eta) &\simeq \eta^2/2 + 1.6449 \\
\mathcal{F}_2(\eta) &\simeq \eta^3/3 + 3.2899\eta \\
\mathcal{F}_3(\eta) &\simeq \eta^4/4 + 4.9348\eta^2 + 11.3644 \\
\mathcal{F}_4(\eta) &\simeq \eta^5/5 + 6.5797\eta^3 + 45.4576\eta \\
\mathcal{F}_5(\eta) &\simeq \eta^6/6 + 8.2247\eta^4 + 113.6439\eta^2 + 236.5323
\end{aligned} \tag{4.9}$$

Finally, in each of the integral approximations, the first term is dominant, with the second order terms being smaller by a factor $\eta^2/(Ck)$, where C is a constant in the range $0.1 \lesssim C \lesssim 0.6$. So for large values of η , we can further approximate the integrals

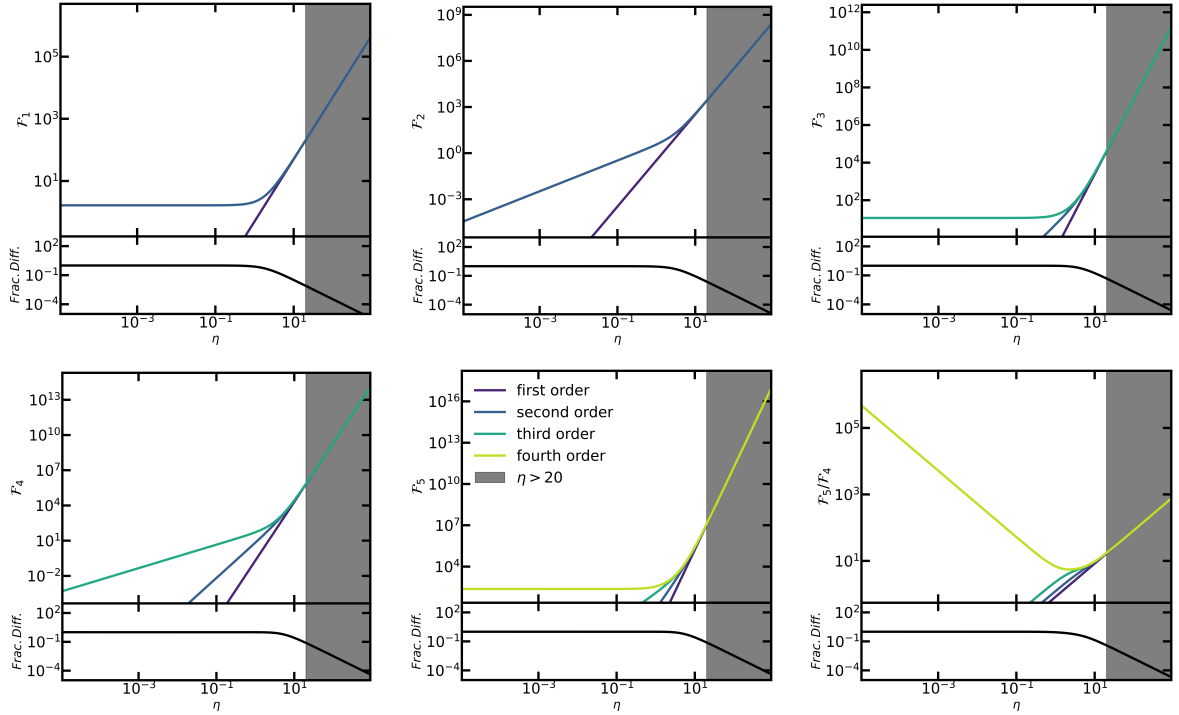


Figure 4.2: Fermi integral approximations for \mathcal{F}_1 , \mathcal{F}_2 , \mathcal{F}_3 , \mathcal{F}_4 , \mathcal{F}_5 , and $\mathcal{F}_5/\mathcal{F}_4$ as labelled. Curves are included showing inclusion of up to the first term, second term, third term, and fourth term in the approximation from equation 4.9, and fractional difference between the full approximation and inclusion of only the leading order term. The grey shaded region shows the limit where this approximation is used.

as:

$$\begin{aligned}
\mathcal{F}_1(\eta) &\simeq \eta^2/2 \\
\mathcal{F}_2(\eta) &\simeq \eta^3/3 \\
\mathcal{F}_3(\eta) &\simeq \eta^4/4 \\
\mathcal{F}_4(\eta) &\simeq \eta^5/5 \\
\mathcal{F}_5(\eta) &\simeq \eta^6/6.
\end{aligned}
\tag{4.10}$$

Figure 4.2 demonstrates truncation of the Fermi integral approximations (equation 4.9) at each order. The range of η for which this approximation is used is shaded grey, and the fractional difference between the non-truncated approximation and the leading order term is also shown. Additionally $\mathcal{F}_5/\mathcal{F}_4$ is included, as this is a ratio that is used directly in the neutrino opacity solver.

4.3 Robustness of Non-linear Root Finding For NSE Solver

In order to track dynamically important changes in nuclear energy content and the production of isotopes up to ^{56}Ni in real time during the collapsar simulation, we make use of the 19-isotope nuclear network of Weaver et al. (1978). The collapsar disk reaches temperatures $T > 10^{10}$ K, which exceeds the nuclear statistical equilibrium (NSE) temperature $T_{\text{NSE}} = 5 \times 10^9$ K. In NSE, nuclear reactions are much faster than the dynamical time of the system, thus abundances reach an equilibrium that is a function of temperature, density, and electron fraction, analogous to ionization equilibrium for collisional ideal gases. While one could simply continue to use the nuclear reaction network in this regime, the nuclear timestep limiter for an explicit hydrodynamic code is:

$$\Delta t = C_{\text{nuc}} \frac{\epsilon}{q_{\text{nuc}}}
\tag{4.11}$$

where C_{nuc} is a constant in the range $(0, 1]$, set by numerical stability, ϵ is the specific internal energy, and q_{nuc} is the specific nuclear heating rate. In the NSE regime nuclear heating becomes very large, limiting the nuclear timestep and thus the simu-

lation timestep. Thus it makes sense to use an NSE solver in this regime, rather than the nuclear network, to avoid this limitation on the timestep. Rodrigo Fernández implemented the NSE solver reported in Seitenzahl et al. (2008) into **FLASH** as described in Section 2.5.2 (Corresponding to Appendix A.2 in Paper I).

This method however introduced numerical issues for cells with temperatures close to the NSE transition. By default, **FLASH** uses a Newton-Raphson (NR) solver to find the temperature consistent with an updated internal energy value, obtained after a conservative hydrodynamic update and/or source term application. The equation of state would often fail to converge when the updated internal energy corresponded to a temperature very close to T_{NSE} in a small number of cells.

To solve this issue, I implemented a modified bisection routine into the EOS solver as a backup for the default NR solver. When solving non-linear root finding problems, bisection routines are less efficient than NR routines, requiring on average more iterations to converge to a result, but they typically are more robust in their convergence. For this reason, I implemented this method, which iterates the specific internal energy using either the NSE solver, or interpolates in the Helmholtz EOS table depending on the temperature. To maintain the efficiency of the solver, the bisection routine only runs in the case that the NR solver initially fails to converge, as this problem only affected a small number of cells at several points in the simulation.

Additionally, in another attempt to make sure bisection is only used when needed, an additional check was added to the NR solver. As shown in Figure 4.3, if the initial temperature guess is in NSE ($T_i > T_{\text{NSE}}$), the first time the temperature iteration falls out of NSE ($T_{i+1} < T_{\text{NSE}}$), the temperature guess is reset to the NSE temperature to determine definitively whether the solution temperature is above or below the NSE limit. If a subsequent iteration of the NR solver finds a value $T_{i+2} < T_{\text{NSE}}$ we set a logical flag to identify that the solution $T_{\text{solution}} < T_{\text{NSE}}$, and the NR solver is restarted with an initial temperature guess of $T_0 = 0.5T_{\text{NSE}}$. Alternatively, if, when the temperature guess is reset to T_{NSE} , the subsequent iteration of NR solver returns

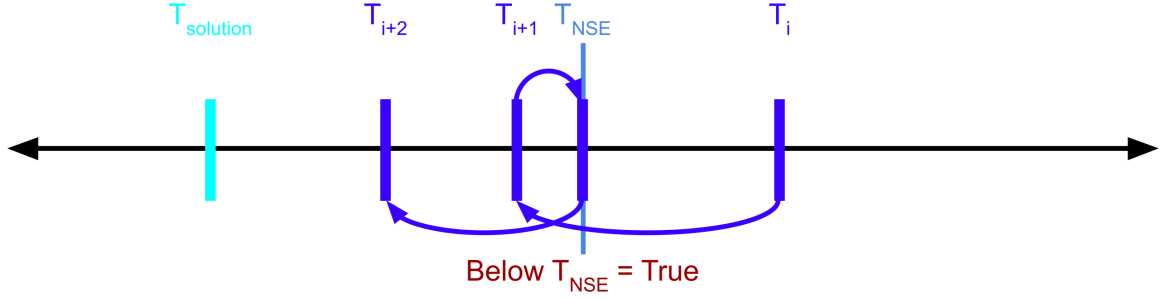


Figure 4.3: Schematic view of the NSE test performed in the NR solver in the case that the initial temperature guess $T_i > T_{NSE}$, but the solution $T_{\text{solution}} < T_{NSE}$

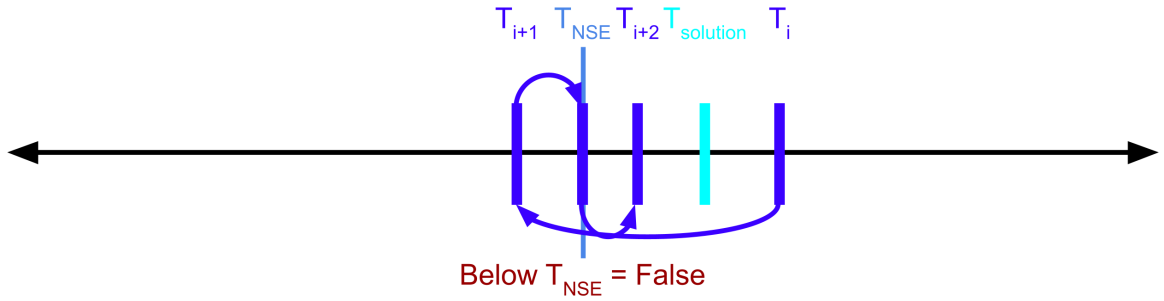


Figure 4.4: Schematic view of the NSE test performed in the NR solver in the case that the initial temperature guess $T_i > T_{NSE}$, and at some point the NR solver overshoots to a value $T_{i+1} < T_{NSE}$ despite the solution $T_{\text{solution}} > T_{NSE}$

$T_{i+2} > T_{NSE}$, a floor is placed on the temperature guess:

$$T_{\text{guess}} = \max(T_{NSE} + \delta T, T_{\text{guess}}) \quad (4.12)$$

where δT is a small temperature increment (to avoid temperature transition issues).

This case is illustrated in Figure 4.4.

4.4 Spatially-varying floors of thermodynamic quantities

This section will discuss in detail the process of deciding on a functional form for variable floors of thermodynamic quantities, which are required in finite volume hydrodynamic methods, such as that used by FLASH, to prevent positive-definite quantities from reaching zero or negative values. This is summarized briefly in Section

2.6, corresponding to Appendix B in Paper I. In the original setup developed by Rodrigo Fernández, a spatially-variable floor was implemented as a two piece piece-wise power-law in radius. This floor had a unique normalization for each variable, and was implemented for density, pressure and internal energy. Additionally, a flat temperature floor of $T = 10^4$ K was used, consistent with an ideal gas law extension to low densities added to the Helmholtz EOS solver by Rodrigo Fernández.

Upon evolution of collapsar models for ~ 50 s after black hole formation, some problems with the variable floor became apparent. Figures 4.5 and 4.8 show the evolution of radial profiles of density, temperature, pressure and specific internal energy for a single polar angle ray along the equator, and the average of the $+\hat{z}$ and $-\hat{z}$ polar rays, respectively. First, with time the peak value of each variable decreases, and given the initial normalization, it was apparent that accretion onto the BH was sufficient to have some variables hit the original floor during the desired evolution time. Additionally, the constraint of a two-piece power-law resulted in the floor function being too low (from two to ten orders of magnitude) relative to the actual thermodynamic variables, which then resulted in code crashes or severe time step limitations whenever cells at shock interfaces reached floor values. For this reason, I decided to implement a new floor that through additional parameters, remained within an approximately constant factor below the hydrodynamic variables by reflecting the radial profile of the star. This also allowed for a lower floor in the inner region.

4.4.1 Density, Pressure, and Specific Internal Energy Floors

As described in Section 2.6 (corresponding to Appendix B in Paper I), I decided on a five piece power-law floor to describe the radial variation of the stellar profile, following the functional form:

$$f_r(r) = \begin{cases} 1 & r < R_1 \\ \left(\frac{R_1}{r}\right)^{s_1} & R_1 < r < R_2 \\ \left(\frac{R_1}{R_2}\right)^{s_1} \left(\frac{R_2}{r}\right)^{s_2} & R_2 < r < R_3 \\ \left(\frac{R_1}{R_2}\right)^{s_1} \left(\frac{R_2}{R_3}\right)^{s_2} \left(\frac{R_3}{r}\right)^{s_3} & R_3 < r < R_4 \\ \left(\frac{R_1}{R_2}\right)^{s_1} \left(\frac{R_2}{R_3}\right)^{s_2} \left(\frac{R_3}{R_4}\right)^{s_3} \left(\frac{R_4}{r}\right)^{s_4} & r > R_4 \end{cases} \quad (4.13)$$

where f_r is a radial factor that varies from 1 at the inner edge of the domain and decreases towards 0 when moving out radially. R_i are transition radii, s_i are power-law slopes. Each of these parameters were set iteratively, informed by the shape of the radial profiles and an early test run of the fiducial model `16TI_SFHo` evolved for ~ 30 s post bounce. The original, and final radial piece-wise power-law floor functions are shown relative to the actual hydrodynamic variables in Figure 4.5.

Additional problems appeared early in the simulation evolution due to low-density polar funnels, which arise due to the polar angle dependence of the angular momentum within the stellar progenitor. Figure 4.6 shows snapshots of the specific internal energy near the inner radial boundary of the grid, which emphasizes the low internal energy in the polar funnel as well as in a series of cells in the middle panel, below the midpoint, with low internal energy between two regions of high internal energy. On several occasions, problematic cells at the interface between the disk and the polar funnel region would drop to the internal energy floor and cause the hydrodynamic solver to crash. This was a persistent problem which motivated the need to include some polar angle dependence to the floor. The variable floors for density, internal energy, and pressure needed to be higher in the polar region, to prevent cells such as these from dropping to values too inconsistent with their neighbours, while being lower in the equatorial region, to ensure the floor did not influence the evolution of the disk, which drives the outflow. For this reason I implemented an angular floor factor that varied smoothly with polar angle, and was highest at the poles and lowest at the equator:

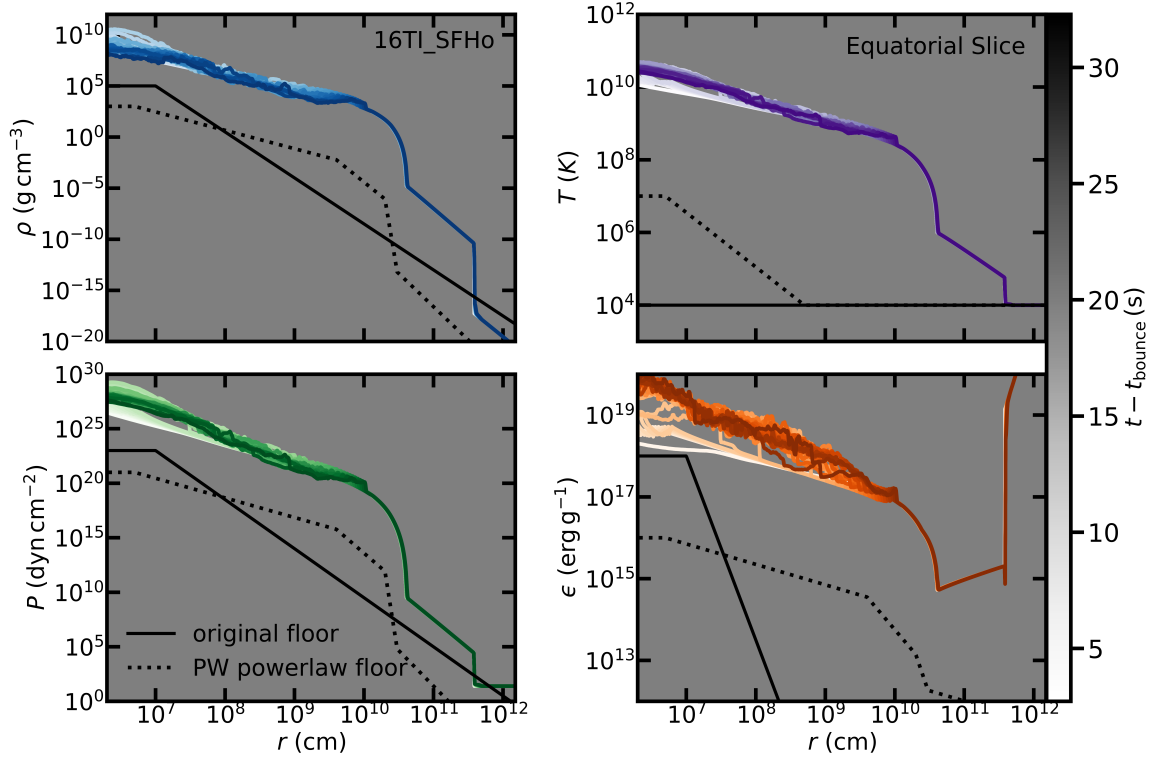


Figure 4.5: Evolution of radial rays along the equator of density (top left), temperature (top right), pressure (bottom left), and specific internal energy (bottom right) over the first ~ 30 s post bounce from model 16TI_SFHo. Time evolution is marked by evolution from white to full color (blue for density, purple for temperature, green for pressure, and orange for internal energy), with the shading indicated by the colour bar. The original two piece piece-wise power-law floor (density, pressure, and internal energy) is marked with a solid black line (flat floor at 10^4 K for temperature). The final five piece piece-wise power-law floor (density, pressure, and internal energy) is marked with a dotted black line (two piece power-law to flat floor for temperature).

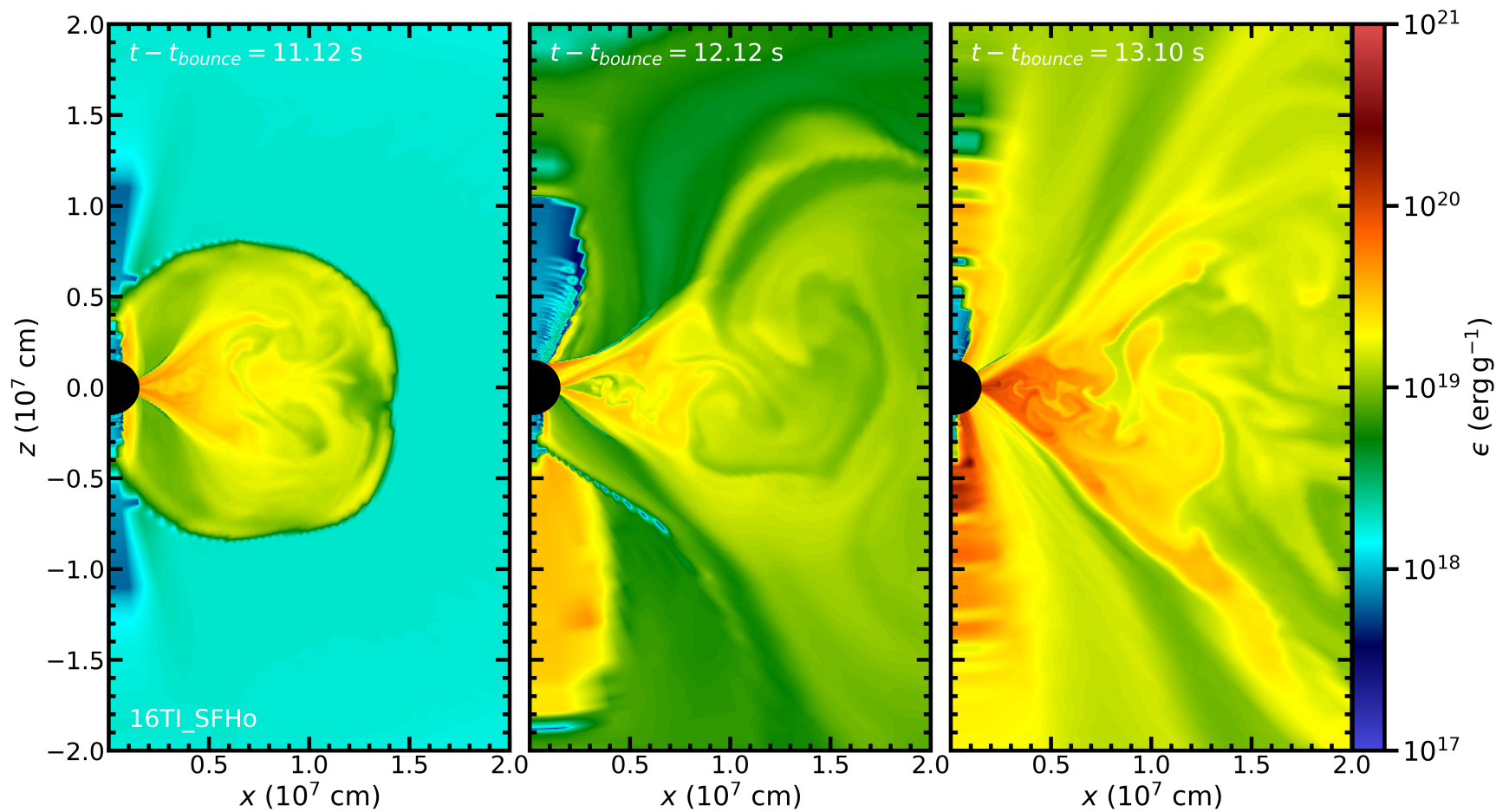


Figure 4.6: Snapshot of the specific internal energy at three points in time shortly after disk formation as labelled in the fiducial model 16TI_SFHo. Limits are selected to highlight specific internal energy differences between the low density polar funnels, and the accretion flow at the inner edge of the disk.

$$f_\theta(\theta) = (1 - \tilde{\theta}_{\text{eq}}) \cos(\theta)^{2\tilde{\theta}_w} + \tilde{\theta}_{\text{eq}}, \quad (4.14)$$

where f_θ is the angular floor factor, and $\tilde{\theta}_{\text{eq}}$ is a parameter that sets the value at the equator relative to the poles. For example, $\tilde{\theta}_{\text{eq}} = 0.1$ sets the equatorial value to 1/10th the value at the poles. $\tilde{\theta}_w$ is a width parameter which sets how quickly the floor drops off from the poles towards the equator. The factor of 2 in the power of $\cos(\theta)$ ensures that the function remains positive for all $\theta \in [0, \pi]$. Figure 4.7 demonstrates how the angular dependence of the floor varies with various values of $\tilde{\theta}_w$ as labelled.

Accounting for the radial and polar angle variation, the total floor is given by:

$$W_{\text{floor}}(r, \theta) = W_0 \cdot f_{\text{floor}}(r, \theta) \quad (4.15)$$

where $W_{\text{floor}}(r, \theta)$ is the floor function, and W_0 is a normalization constant which is model and variable dependent and f_{floor} is given by:

$$f_{\text{floor}}(r, \theta) = f_r(r) \cdot f_\theta(\theta). \quad (4.16)$$

Figure 4.8 displays the floor functions relative the hydrodynamic variable profiles in the polar region (average of the $+\hat{z}$ and $-\hat{z}$ slices). Note that the scaling of the piece-wise power-law floor is different from that of Figure 4.5 due to the polar angle dependence described in equation 4.14.

4.4.2 Temperature Floor

As described in Section 2.6 (corresponding to Appendix B in Paper I), further issues caused by problematic cells at the interface of the low density funnel and accretion disk led to the modification of the temperature floor. This is the same problem that motivated the addition of a polar angle dependent floor, however this issue re-emerged at slightly later simulation time. The problematic cells were sufficiently far away from the poles that the polar angle dependence of the floor could not simply be adjusted

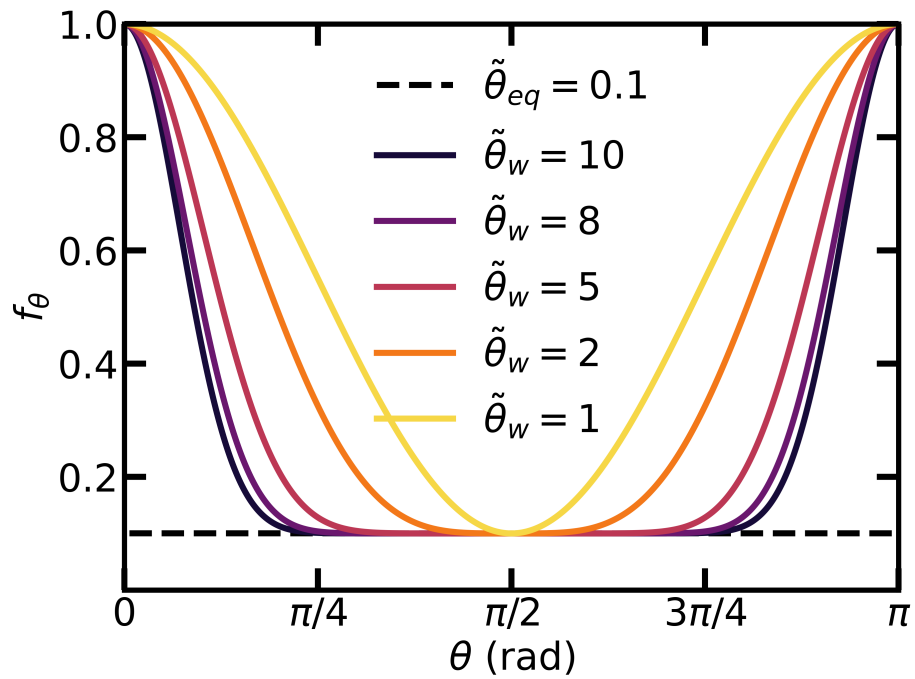


Figure 4.7: Variation of the theta factor f_θ across all polar angles. f_θ varies from 1 at the poles to a value $\tilde{\theta}_{eq}$ at the equator. The drop off rate is controlled by $\tilde{\theta}_w$, with higher values dropping off more quickly as the polar angle moves away from either pole, with five examples plotted as labelled.

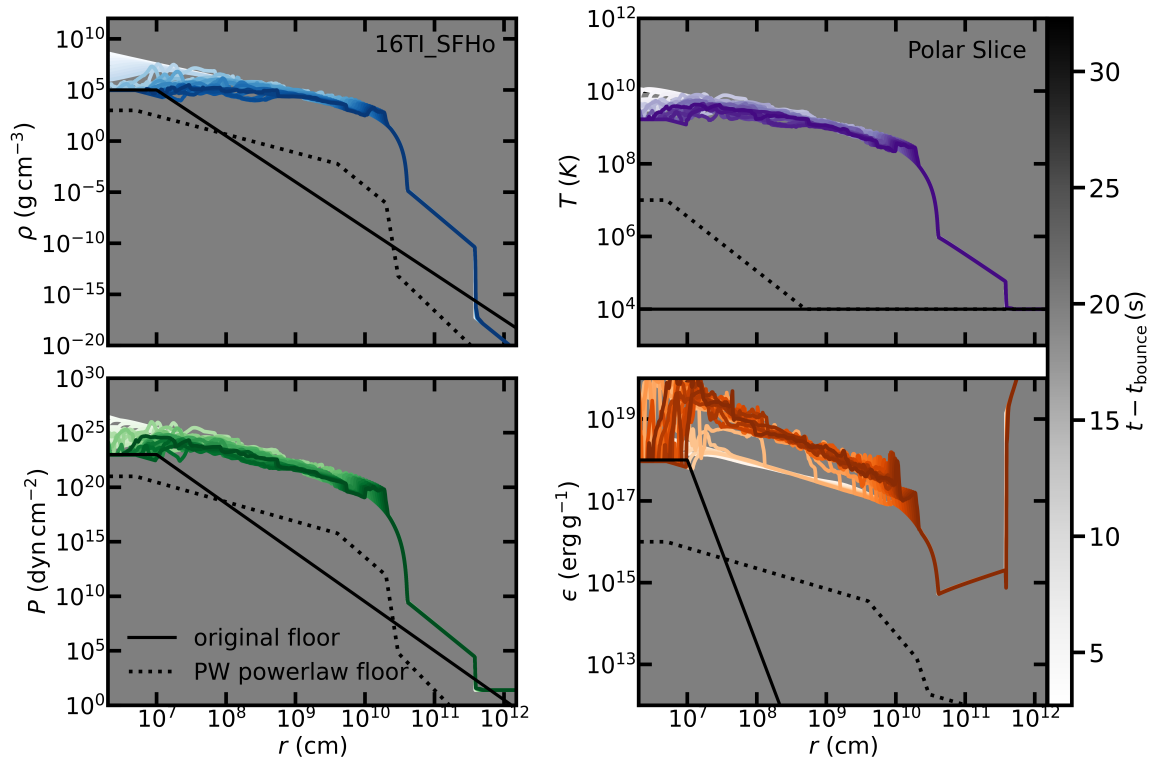


Figure 4.8: Same as Figure 4.5, except variables represent an average of the $+\hat{z}$ and $-\hat{z}$ polar slices. Note that floors have a different scale factor here due to the theta factor f_θ described in section 4.4.

to solve this problem, without causing unintended effects in the disk. Investigating these cells with low specific internal energy, similar to those in the middle panel of Figure 4.6, the temperature of these cells sat on the initially flat temperature floor at 10^4 K. To solve this issue I implemented a smoothly varying temperature floor that raised the minimum value near the inner radial boundary, while quickly dropping off to the flat floor at 10^4 K:

$$T_{\text{floor}}(r) = \max \left[10^7 \text{ K} \cdot \left(\frac{50 \text{ km}}{r} \right)^2, 10^4 \text{ K} \right]. \quad (4.17)$$

The final temperature floor is displayed in the top right panels of Figures 4.5 and 4.8. Note that this floor is essentially flat at 10^7 K out to 50 km or 5×10^6 cm, then decays as a power-law outward radially, with a minimum value of 10^4 K. This temperature floor essentially acts as an specific internal energy floor, and the parameters were tuned such that these problematic polar cells were affected, without influencing the surrounding material by evolving the model for several seconds, testing various power-law slopes and transition radii.

4.5 Shock Tracking

To analyze the energetics of the post shock region, and to analyze early oscillations of the shock wave as discussed in Section 2.2.4, it was necessary to develop a shock tracking algorithm. To track the shock-wave driven by the viscous disk wind as it travelled through the collapsing star, I adapted a shock tracking algorithm previously developed by Rodrigo Fernández for CCSNe. The existing shock tracking method performed a search radially inward from the a specified radius using a dimensionless form of the pressure gradient H_P to mark the edge of the shock:

$$H_P = \frac{r}{P} \frac{\partial P}{\partial r}. \quad (4.18)$$

This shock tracking technique was however insufficient to track the shock as it propagated all the way to the stellar surface. Figure 4.9 shows the dimensionless pressure gradient and dimensionless poloidal velocity gradient

$$H_{|\mathbf{v}_p|} = \frac{r}{|\mathbf{v}_p|} \frac{\partial |\mathbf{v}_p|}{\partial r} \quad (4.19)$$

across a radial slice through the equator of the `16TI_SFHo` progenitor at the start of the `FLASH` simulation (prior to shock formation). It is notable that pressure gradient becomes very large at $\sim 4 \times 10^{10}$ cm, before dropping to a flat value prior to a final spike at $\sim 4 \times 10^{11}$ cm. The increase in pressure gradient occurs at the edge of the `kepler` stellar progenitor from Woosley & Heger (2006). The outermost cell in the stellar progenitor has a very large relative radial extent, with the second last cell located at $\sim 4 \times 10^{10}$ cm and the final cell located at $\sim 7 \times 10^{11}$ cm. These large cells and an interpolation method used for the outer half of the last `kepler` cell create these discontinuities in the pressure gradient. These features are present, but less noticeable if we instead use a dimensionless poloidal velocity gradient. However, this curve shows an additional spike at the interface between where the `GR1D` grid ends, and where we interpolate from the `kepler` profile for the remainder of the star. While these are small changes in the pressure and poloidal velocity, they are accentuated in the gradients, which emphasize changes in the radial slope of these variables.

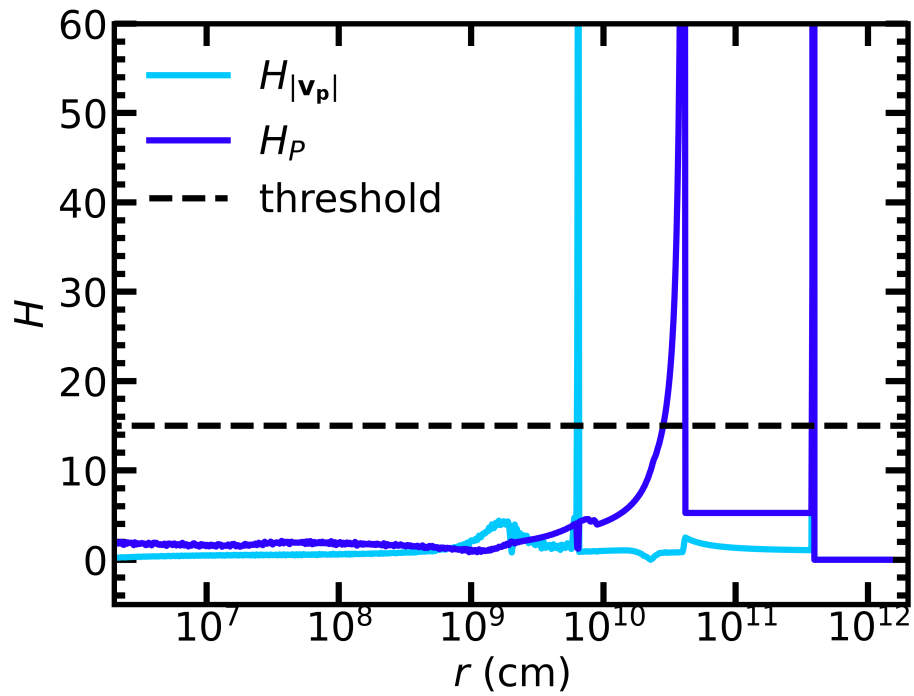


Figure 4.9: Dimensionless pressure gradient and poloidal velocity gradient along the equator of the 16TI.SFHo model at the start of the FLASH simulation. At this point, the shock has not yet formed, so the scale heights are representative of the progenitor profile alone. The threshold values used to mark the shock front is marked with a dashed black line.

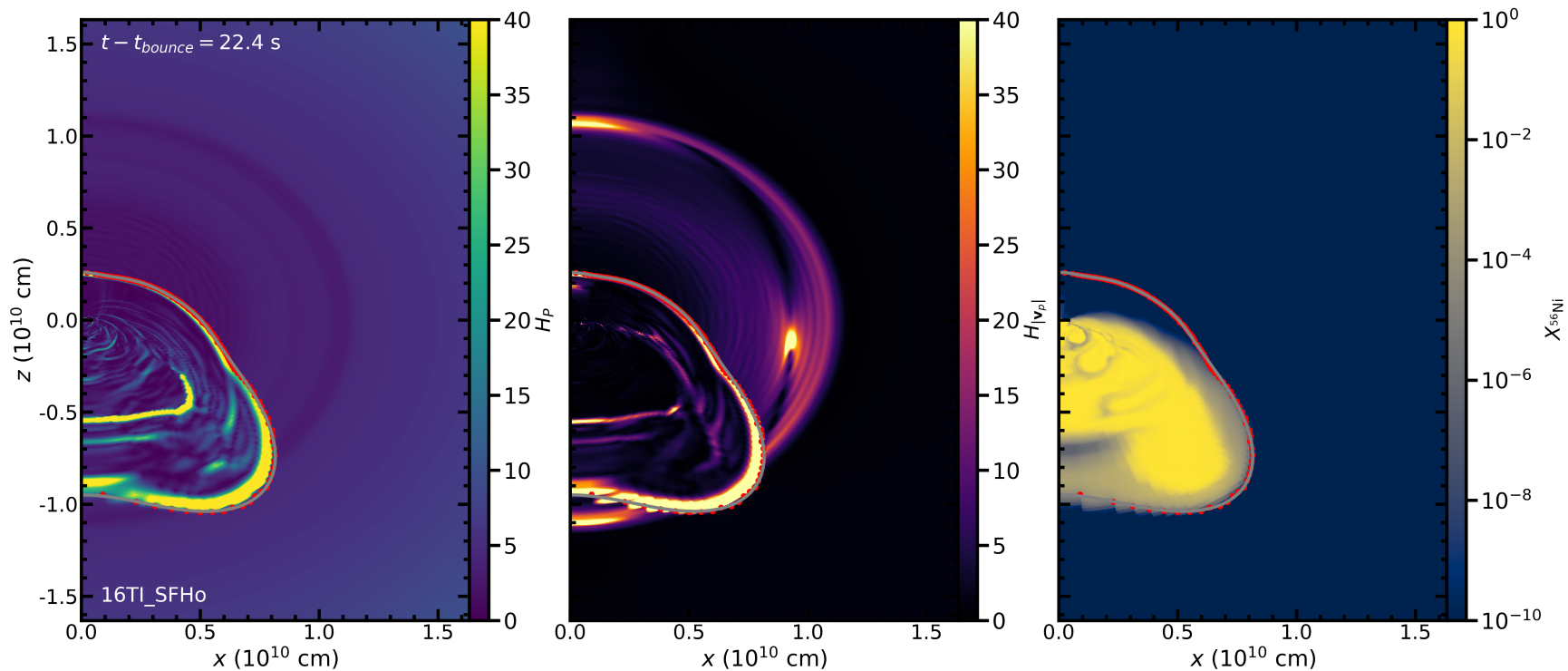


Figure 4.10: Snapshot of the three shock tracking variables (dimensionless pressure gradient, dimensionless poloidal velocity gradient, and ^{56}Ni mass fraction) from model 16TI_SFHo. Radial shock positions $r_s(\theta)$ found by the shock tracking algorithm are marked with red dots. The shock front is fit by a 10th order Legendre polynomial which is marked by the grey line.

With this in mind, I used a combination of these two gradients as well as a condition on the mass fraction of ^{56}Ni ($X_{^{56}\text{Ni}} > 10^{-8}$) to track the shock geometry throughout the star. Figure 4.10 shows the dimensionless pressure gradient, poloidal velocity gradient, and ^{56}Ni mass fraction snapshots of the 16TI_SFHo model. Notice the presence of stellar profile features not connected to the shock-front with high values of the poloidal velocity gradient ($H_{|v_p|} \gtrsim 15$). These features are present in the pressure gradient but are much weaker ($H_P \lesssim 5$), and not present at all in the ^{56}Ni mass fraction at all. Also notice that the gradient or mass fraction behind the shock front exceeds the threshold value for detection in many locations, hence the need for an inward radial search marking the first time the condition is triggered. While no single one of these variables was sufficient to track through the entire star on its own, a combination of the three was sufficient. The tracking condition used is the following:

$$\text{condition} = \begin{cases} H_P > 15 & r \leq R_1 \\ H_{|v_p|} > 15 & R_1 < r \leq R_2 \\ \begin{cases} X_{^{56}\text{Ni}} > 10^{-8} & \text{well mixed ejecta} \\ H_P > 15 & \text{poorly mixed ejecta} \end{cases} & r > R_2, \end{cases} \quad (4.20)$$

where R_1 and R_2 are transition radii that are set based on the radial positions of spikes present in Figure 4.9. Figure 4.11 is a schematic diagram that describes the shock tracking algorithm for a generic shock front shape. The shock tracking algorithm works as follows: Along each polar angle grid cell a inward radial search is performed starting at $r = R_1$, recording the radial position where Condition I (Equation 4.20 and Figure 4.11) is satisfied for the first time. This process is repeated every 10 ms of simulation time. When the radial position of the shock along some polar angle $r_s(\theta) \sim R_1$, the algorithm switches to condition II along that slice, and the initial radius for the search is reset to R_2 . Finally, when the shock radius along some polar angle $r_s(\theta) \sim R_2$, the tracking algorithm switches to condition III, and the radial search along that angular slice will now begin from the outer edge of the domain. In the case that the radial search fails to return a radial position, the value of $r_s(\theta)$

from the previous time is used. This shock tracking algorithm is used from the black hole formation time t_{bh} until the shock breakout time t_{sb} . Having returned the shock position across all polar angles and its evolution across simulation time $r_s(\theta, t)$, we can create a mask to separate the pre- and post-shock regions. These masks are used to track energetics of the post shock region, and Legendre coefficients a_i are used for early shock oscillation analysis performed in Chapter 2.

4.6 Post-shock Heating

To differentiate the NDAF and ADAF energetic regimes discussed in other similar collapsar papers such as Just et al. (2022a), Fujibayashi et al. (2023a), and Fujibayashi et al. (2023b), I developed a parallelized code that efficiently integrates heating rates over the post-shock region. With evolved models having simulation times up to $t_f \sim 400$ s, there was a need to perform up to $\sim 4 \times 10^4$ integration's for each heating rate ($q_{\text{visc}}, q_{\nu}, q_{\text{nuc}}$) to be analyzed. To calculate the relative heating in the post shock region, this code calculates:

$$Q(t) = \iiint \text{post_shock_mask} \cdot q(t, r, \theta, \phi) (1 - X_{\text{atm}}) dV, \quad (4.21)$$

where $Q(t)$ is one of the total viscous, neutrino, or nuclear heating rates in the post shock region, q is the corresponding specific heating rate defined across the computational grid, X_{atm} is the atmospheric mass fraction, which is a passive scalar variable used to differentiate atmospheric or material added when density hits the variable floor, and the `post_shock_mask` is a mask defined as:

$$\text{post_shock_mask} = \begin{cases} 0 & r(\theta) > r_s(\theta) \\ 1 & r(\theta) \leq r_s(\theta) \end{cases} \quad (4.22)$$

where $r_s(\theta)$ is the shock radius at a give polar angle θ described in Section 4.5.

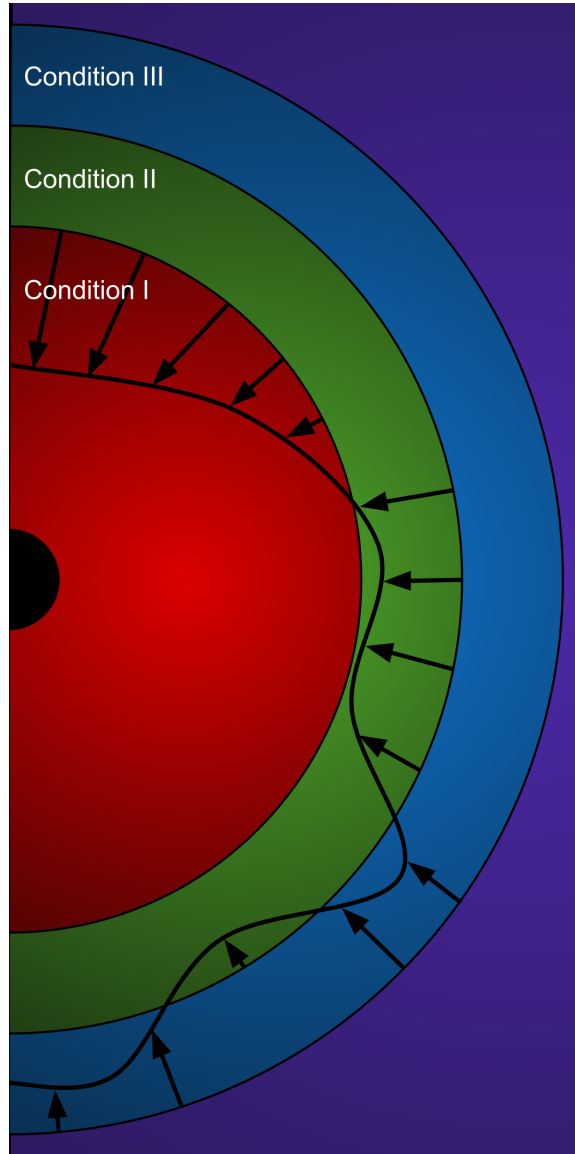


Figure 4.11: Schematic of the three condition shock tracking algorithm used within the collapsar for a generic shock geometry. The shock front is marked with a thick black line, arrows show the inward radial search performed by the shock tracking algorithm. The condition used to mark the shock front position is one of three conditions as labelled corresponding to Equation 4.20.

Chapter 5

Conclusions and Future Work

5.1 Conclusions

Motivated by the potential need for a galactic heavy element enrichment event that occurs on shorter timescales than BNS mergers occur after star formation, we investigate collapsars as one potential source that meets the timescale constraint. We develop and present results from global simulations of collapsar disk wind outflows originating from a disk that forms self consistently via centrifugal support around the central BH. We investigate heavy element nucleosynthesis in these outflows, and explore other observables associated with the collapsar explosion.

Collapsars are rapidly rotating Wolf-Rayet stars, that at the end of their lives undergo core-collapse and fail to explode via regular supernova channels like the delayed neutrino mechanism and form a BH. Due to the significant rotation of the progenitor star, as material from the stellar mantle collapses onto the central BH, the angular momentum of accreting fluid parcels increases radially outward. Eventually, the angular momentum in the accreting material is sufficient to circularize outside the innermost stable circular orbit of the BH. At this point an accretion disk forms close to the central black hole. Acting in the accretion disk, the magnetorotational instability transports angular momentum allowing for accretion from the inner edge, and drives turbulence and subsequently an outflow from the accretion disk. Additionally, magnetic winding can drive a relativistic jet outflow from the polar regions above and

below the BH-accretion disk system. One or a combination of these two outflows may be capable of driving a successful explosion of the star.

Collapsars have been suggested as a source of r -process enrichment based on the estimated densities and temperatures reached by the accretion disk near the black hole. The accretion disk is predicted to be hot (10^{10} K), as well as degenerate due to the extreme densities caused by surrounding accretion onto the BH. Due to the electron degeneracy of the material in the disk, charged-current reactions favour electrons being captured by protons producing an excess of neutrons. This neutronization of the disk material is the main motivation for collapsars being proposed as r -process enrichment sites, due to the need for a neutron-rich environment for the r -process to operate.

At the start of this project, the state of the art GRMHD simulations modelling the disk wind were optimistic of these collapsar disk wind outflows as r -process sites. However, these simulations were limited in several ways. They were short in comparison to the timescale needed for the shock wave to breakout from the stellar surface (~ 100 ms simulations, with shock breakout timescales being ~ 100 s). Also, crucially, the simulations started from an equilibrium accretion disk which was embedded in a uniform low density medium based on an argument that the infalling stellar mantle's ram pressure was insignificant in comparison to the disk wind. This motivated the need for long-term collapsar simulations where the accretion disk forms via centrifugal support, modeling the entirety of the star to get a better sense of whether r -process elements could be produced and if they could make it out of the star.

Some of the questions we wanted to answer were whether the disk wind alone could drive a successful explosion of the star, whether any neutronized material would be ejected from the accretion disk, and whether collapsar disk wind outflows had properties consistent with type Ic-BL SNe, the proposed SNe type associated with the collapsar progenitor. Also, are there any unique observables associated with a collapsar related to its neutrino signal, or via oscillations of the shock wave like those

seen in CCSNe? We also set out to perform detailed nucleosynthesis calculations in these sub-relativistic disk outflows to explore the production of any heavy elements, the relative abundance pattern, and the heavy element production processes that act in the outflow.

In order to explore and answer some of these questions, we developed a two part hydrodynamics framework that evolved a rapidly-rotating WR progenitor star from core collapse to black hole formation, then evolved the infalling stellar profile, self-consistently forming the centrifugally supported accretion disk, and subsequent disk wind driven shock wave as it expands beyond the surface of the stellar progenitor.

Progenitor WR stars were evolved in spherically-symmetric, neutrino radiation-hydrodynamics code from core collapse until BH formation. This code is general-relativistic, includes a three-flavour gray neutrino leakage scheme treating emission and absorption, and accounts for rotation approximately. These stellar profiles are then mapped into an axisymmetric viscous hydrodynamics simulation with Newtonian self-gravity, a pseudo-Newtonian potential to reproduce the plunge near the central black hole, a 19-isotope nuclear network, finding abundances assuming NSE above 5×10^9 K, including neutrino cooling and heating via a lightbulb style leakage scheme, and an α viscosity scheme. The evolution in this phase extends from BH formation through disk formation, and until after the disk wind powered shock wave expands beyond the stellar surface.

To facilitate detailed nucleosynthesis in these models, we make use of passive tracer particles, initialized at disk formation, and allowed to follow the outflow, sampling the hydrodynamic variables and heating rates experienced by that fluid parcel. These tracer particle trajectories were then used to perform detailed nucleosynthesis in a post-processing nuclear reaction network.

In Chapter 2, we describe the fiducial model, and present results from an initial suite of 5 models varying the WR progenitor star, EOS used during the initial evolution until BH formation, and the viscous α parameter. In each of our models, we find

that the disk wind powered shock wave is capable of breaking out from the stellar surface. In terms of consistency of our model with parameters inferred from observations of Type Ic-BL SNe, we find that our models produce sufficient ^{56}Ni to power the lightcurve, however the mass weighted average asymptotic velocity of our outflow is a factor of $\sim 2 - 3$ times too low to explain the spectral features seen in these SNe. The total kinetic energy of the outflow is in the correct range, but with a higher than expected mass, the velocity is too low.

In each of our simulations, we find that there is insufficient neutronization of the ejected material to produce heavy r -process elements. While the midplane of the disk does neutronize significantly, this occurs during an early phase where the disk wind is weak, and with outflows originating from the surface of the disk. This neutronized material is accreted onto the black hole, with only very weakly neutronized material making its way into the outflow.

We identify a potentially unique neutrino luminosity signature observable in collapsars, a drop of many orders of magnitude during black hole formation, followed by an increase to similar luminosities at disk formation, and a subsequent power-law decay. The duration of this drop in neutrino luminosity and the luminosity of the subsequent peak are properties that depend on the compactness and rotation profile of the stellar progenitor, and thus may be useful as an observable. Though this would likely require a galactic collapsar ($\sim 1\%$ of CCSNe) to measure enough neutrinos given current detector sensitivities. Finally, in some models we see oscillation of the shock wave during an early NDAF phase. The oscillation frequencies are consistent with characteristic frequencies of the cavity. After this early NDAF phase (~ 1 s) the shock begins to expand rapidly in the ADAF phase, and the shock geometry freezes remaining roughly the same as it expands out to the stellar surface. Generally, due to perturbations during the early oscillating phase, the shock wave expands towards one of the polar directions before breaking out from the stellar surface in each model.

While this initial study tempered expectations of significant heavy r -process ele-

ment production due to the minimal neutronization of the ejecta, the high entropy, and the partial protonization of ejecta motivated detailed nucleosynthesis calculations as a followup.

In Chapter 3, we presented three additional models where the angular momentum profile of the star was modified to test whether extending the NDAF phase, where the vast majority of neutronization occurs, could create more neutronized material, and if any of that material can make its way into the outflow (to provide upper limits on neutronized material in the outflow). Additionally, we perform detailed nucleosynthesis calculations based on all 8 models, and analyze the distribution of isotopes from the nuclear network within the outflow, which may be useful for future lightcurve predictions.

The ejecta from our simulation consists of several M_{\odot} of ^{16}O , $\sim 1M_{\odot}$ of ^{12}C , ^{20}Ne , and ^{56}Ni , with $< 1M_{\odot}$ of other elements from the 19-isotope nuclear network. The asymptotic velocity of ^{56}Ni is found to be consistent with expansion velocities of Type Ic-BL SNe, while the mass-weighted average asymptotic velocity of the entire ejecta is too slow by a factor of ~ 2 .

After detailed nucleosynthesis calculations, we find that only one of the eight models significantly produces first peak r -process elements, with the remaining models producing at most trace amounts of elements heavier than the iron group. A subset of the models produce small amounts of heavier elements up to $A \sim 200$ in a small number of tracer particles that sample high-entropy ($s \sim 80k_B$ per baryon), proton-rich ejecta via the rp -process. While the tracer particles do not fully sample the ejecta, they trace matter that accretes into the disk during the NDAF phase, and are subject to significant neutrino reprocessing. Our results suggest that the collapsar disk outflow may allow for the rp -process to act.

Modification of the angular momentum profile in our three additional models for the second paper only appreciably extended the NDAF phase in one of the three models, with only one of the other two models producing a trace amount of heavy

elements. This suggests that modification of the angular momentum profile alone cannot lead to the production of heavy r -process elements in the context of viscous HD simulations of the disk outflow. The partial sampling of the ejecta by the tracer particles tends to sample the low-entropy end of the distribution, suggesting that some heavy r -process element production may occur in the high-entropy regime that was not sampled, however this occurs in the high-entropy tail of the mass ejection distribution, and thus would be small in mass. While the majority of neutronization occurs in the midplane of the accretion disk near the inner radial edge, the disk outflow originates from the outer edge of the accretion disk. With accretion onto the central BH constantly occurring during the simulation, almost none of the neutronized material makes its way into the outflow, constraining heavy element nucleosynthesis.

While our results suggest that the production of large quantities of heavy elements via the r -process in sub-relativistic collapsar disk outflows are unlikely, the results may differ if MHD effects are included. In the context of NS merger disks, rapid ejection of material during the NDAF phase in MHD simulations is highly dependent on the initial field geometry and strength.

5.2 Future Work

Future work based on these simulations may include analysis of the early oscillations of the shock wave to decipher whether an observable gravitational wave signal is possible like those predicted in CCSNe, potential light curve predictions, or more in-depth frequency analysis of the shock oscillation to investigate whether these oscillations are reflected in the neutrino luminosities.

Bibliography

- 2023, Evaluated Nuclear Structure Data File (ENSDF), <https://www.nndc.bnl.gov/ensdfarchivals/>
- Abbott, B. P., et al. 2017, *PhRvL*, 119, 161101, doi: 10.1103/PhysRevLett.119.161101
- . 2019, *Physical Review X*, 9, 031040, doi: 10.1103/PhysRevX.9.031040
- Abbott, R., et al. 2021, *Physical Review X*, 11, 021053, doi: 10.1103/PhysRevX.11.021053
- Aloy, M. Á., & Obergaulinger, M. 2021, *MNRAS*, 500, 4365, doi: 10.1093/mnras/staa3273
- Antoni, A., & Quataert, E. 2023, *MNRAS*, 525, 1229, doi: 10.1093/mnras/stad2328
- Arnett, W. D. 1982, *ApJ*, 253, 785, doi: 10.1086/159681
- Artemova, I. V., Bjoernsson, G., & Novikov, I. D. 1996, *ApJ*, 461, 565, doi: 10.1086/177084
- Asplund, M., Grevesse, N., Sauval, A. J., & Scott, P. 2009, *ARA&A*, 47, 481, doi: 10.1146/annurev.astro.46.060407.145222
- Bardeen, J. M., Press, W. H., & Teukolsky, S. A. 1972, *ApJ*, 178, 347, doi: 10.1086/151796
- Barnes, J., & Duffell, P. C. 2023, *ApJ*, 952, 96, doi: 10.3847/1538-4357/acdb67

- Barnes, J., & Metzger, B. D. 2022, *ApJL*, 939, L29, doi: 10.3847/2041-8213/ac9b41
- Batta, A., & Lee, W. H. 2016, *MNRAS*, 459, 2140, doi: 10.1093/mnras/stw697
- Beloborodov, A. M. 2003, *ApJ*, 588, 931, doi: 10.1086/374217
- Beloborodov, A. M., & Illarionov, A. F. 2001, *MNRAS*, 323, 167, doi: 10.1046/j.1365-8711.2001.04133.x
- Benavides, S. J., & Alexakis, A. 2017, *Journal of Fluid Mechanics*, 822, 364, doi: 10.1017/jfm.2017.293
- Bethe, H. A., Applegate, J. H., & Brown, G. E. 1980, *ApJ*, 241, 343, doi: 10.1086/158346
- Bethe, H. A., & Wilson, J. R. 1985, *ApJ*, 295, 14, doi: 10.1086/163343
- Blandford, R. D., & Znajek, R. L. 1977, *MNRAS*, 179, 433, doi: 10.1093/mnras/179.3.433
- Blondin, J. M., Mezzacappa, A., & DeMarino, C. 2003, *ApJ*, 584, 971, doi: 10.1086/345812
- Bodenheimer, P., & Woosley, S. E. 1983, *ApJ*, 269, 281, doi: 10.1086/161040
- Boffetta, G., & Ecke, R. E. 2012, *Annual Review of Fluid Mechanics*, 44, 427, doi: 10.1146/annurev-fluid-120710-101240
- Bruenn, S. W. 1985, *ApJS*, 58, 771, doi: 10.1086/191056
- Burbidge, E. M., Burbidge, G. R., Fowler, W. A., & Hoyle, F. 1957, *Reviews of Modern Physics*, 29, 547, doi: 10.1103/RevModPhys.29.547
- Cameron, A. G. W. 1957, *PASP*, 69, 201, doi: 10.1086/127051

- Cavallo, L., Cescutti, G., & Matteucci, F. 2023, *A&A*, 674, A130, doi: 10.1051/0004-6361/202346412
- Chadwick, J. 1932, *Proceedings of the Royal Society of London Series A*, 136, 692, doi: 10.1098/rspa.1932.0112
- Chen, W.-X., & Beloborodov, A. M. 2007, *ApJ*, 657, 383, doi: 10.1086/508923
- Childs, H., et al. 2012, in *High Performance Visualization—Enabling Extreme-Scale Scientific Insight* (eScholarship, University of California), 357–372. <https://escholarship.org/uc/item/69r5m58v>
- Christie, I. M., Lalakos, A., Tchekhovskoy, A., et al. 2019, *MNRAS*, 490, 4811, doi: 10.1093/mnras/stz2552
- Colgate, S. A. 1971, *ApJ*, 163, 221, doi: 10.1086/150760
- Combi, L., & Siegel, D. M. 2023, *PhRvL*, 131, 231402, doi: 10.1103/PhysRevLett.131.231402
- Côté, B., Belczynski, K., Fryer, C. L., et al. 2017, *ApJ*, 836, 230, doi: 10.3847/1538-4357/aa5c8d
- Cowan, J. J., Sneden, C., Lawler, J. E., et al. 2021, *Reviews of Modern Physics*, 93, 015002, doi: 10.1103/RevModPhys.93.015002
- Crosato Menegazzi, L., Fujibayashi, S., Takahashi, K., & Ishii, A. 2023, arXiv e-prints, arXiv:2311.04297, doi: 10.48550/arXiv.2311.04297
- Crowther, P. A. 2007, *ARA&A*, 45, 177, doi: 10.1146/annurev.astro.45.051806.110615
- Curtis, S., Bosch, P., Mösta, P., et al. 2023a, arXiv e-prints, arXiv:2305.07738, doi: 10.48550/arXiv.2305.07738

- Curtis, S., Miller, J. M., Fröhlich, C., et al. 2023b, *ApJL*, 945, L13, doi: 10.3847/2041-8213/acba16
- Cyburt, R. H., Amthor, A. M., Ferguson, R., et al. 2010, *ApJS*, 189, 240, doi: 10.1088/0067-0049/189/1/240
- Dainotti, M. G., Simone, B. D., Islam, K. M., et al. 2022, *The Astrophysical Journal*, 938, 41, doi: 10.3847/1538-4357/ac8b77
- De, S., & Siegel, D. M. 2021, *ApJ*, 921, 94, doi: 10.3847/1538-4357/ac110b
- Dean, C., & Fernández, R. 2024, *PhRvD*, 109, 083010, doi: 10.1103/PhysRevD.109.083010
- Dubey, A., Antypas, K., Ganapathy, M. K., et al. 2009, *J. Par. Comp.*, 35, 512 , doi: DOI:10.1016/j.parco.2009.08.001
- Fahlman, S., & Fernández, R. 2018, *ApJL*, 869, L3, doi: 10.3847/2041-8213/aaf1ab
- . 2022a, *MNRAS*, 513, 2689, doi: 10.1093/mnras/stac948
- . 2022b, *MNRAS*, 513, 2689, doi: 10.1093/mnras/stac948
- Fahlman, S., Fernández, R., & Morsink, S. 2023, *MNRAS*, 526, 952, doi: 10.1093/mnras/stad2653
- Fernández, R. 2015, *MNRAS*, 452, 2071, doi: 10.1093/mnras/stv1463
- Fernández, R., Foucart, F., & Lippuner, J. 2020, *MNRAS*, 497, 3221, doi: 10.1093/mnras/staa2209
- Fernández, R., Just, O., Xiong, Z., & Martínez-Pinedo, G. 2023a, preprint, arXiv:2307.02554, doi: 10.48550/arXiv.2307.02554
- . 2023b, arXiv e-prints, arXiv:2307.02554, doi: 10.48550/arXiv.2307.02554

- Fernández, R., Kasen, D., Metzger, B. D., & Quataert, E. 2015, *MNRAS*, 446, 750, doi: 10.1093/mnras/stu2112
- Fernández, R., Margalit, B., & Metzger, B. D. 2019a, *MNRAS*, 488, 259, doi: 10.1093/mnras/stz1701
- Fernández, R., & Metzger, B. D. 2013, *MNRAS*, 435, 502, doi: 10.1093/mnras/stt1312
- Fernández, R., Quataert, E., Kashiyama, K., & Coughlin, E. R. 2018, *Monthly Notices of the Royal Astronomical Society*, 476, 2366, doi: 10.1093/mnras/sty306
- Fernández, R., Quataert, E., Kashiyama, K., & Coughlin, E. R. 2018, *MNRAS*, 476, 2366, doi: 10.1093/mnras/sty306
- Fernández, R., Richers, S., Mulyk, N., & Fahlman, S. 2022, *PhRvD*, 106, 103003, doi: 10.1103/PhysRevD.106.103003
- Fernández, R., Tchekhovskoy, A., Quataert, E., Foucart, F., & Kasen, D. 2019b, *MNRAS*, 482, 3373, doi: 10.1093/mnras/sty2932
- . 2019c, *MNRAS*, 482, 3373, doi: 10.1093/mnras/sty2932
- Fewell, M. P. 1995, *American Journal of Physics*, 63, 653, doi: 10.1119/1.17828
- Filippenko, A. V. 1997, *ARA&A*, 35, 309, doi: 10.1146/annurev.astro.35.1.309
- Foglizzo, T., Galletti, P., Scheck, L., & Janka, H. T. 2007, *ApJ*, 654, 1006, doi: 10.1086/509612
- Frankel, S., & Metropolis, N. 1947, *Physical Review*, 72, 914, doi: 10.1103/PhysRev.72.914
- Fröhlich, C., Martínez-Pinedo, G., Liebendörfer, M., et al. 2006, *PhRvL*, 96, 142502, doi: 10.1103/PhysRevLett.96.142502
- Fryer, C. L., Woosley, S. E., & Heger, A. 2001, *ApJ*, 550, 372, doi: 10.1086/319719

- Fryxell, B., Olson, K., Ricker, P., et al. 2000, *ApJS*, 131, 273, doi: 10.1086/317361
- Fujibayashi, S., Sekiguchi, Y., Shibata, M., & Wanajo, S. 2023a, *ApJ*, 956, 100, doi: 10.3847/1538-4357/acf5e5
- Fujibayashi, S., Tsz-Lok Lam, A., Shibata, M., & Sekiguchi, Y. 2023b, arXiv e-prints, arXiv:2309.02161, doi: 10.48550/arXiv.2309.02161
- Fujimoto, S.-i., Hashimoto, M.-a., Arai, K., & Matsuba, R. 2004, *ApJ*, 614, 847, doi: 10.1086/423778
- Fujimoto, S.-i., Hashimoto, M.-a., Kotake, K., & Yamada, S. 2007, *ApJ*, 656, 382, doi: 10.1086/509908
- Fujimoto, S.-i., Kotake, K., Yamada, S., Hashimoto, M.-a., & Sato, K. 2006, *ApJ*, 644, 1040, doi: 10.1086/503624
- Fuller, G. M., Fowler, W. A., & Newman, M. J. 1982, *ApJS*, 48, 279, doi: 10.1086/190779
- Goldberg, L., Muller, E. A., & Aller, L. H. 1960, *ApJS*, 5, 1, doi: 10.1086/190053
- Goriely, S. 1999, *A&A*, 342, 881
- Gottlieb, O., Lalakos, A., Bromberg, O., Liska, M., & Tchekhovskoy, A. 2022, *MNRAS*, 510, 4962, doi: 10.1093/mnras/stab3784
- Gottlieb, O., Renzo, M., Metzger, B. D., Goldberg, J. A., & Cantiello, M. 2024, arXiv e-prints, arXiv:2407.16745, doi: 10.48550/arXiv.2407.16745
- Graham, M. J., et al. 2019, *PASP*, 131, 078001, doi: 10.1088/1538-3873/ab006c
- Graur, O., Bianco, F. B., Modjaz, M., et al. 2017, *ApJ*, 837, 121, doi: 10.3847/1538-4357/aa5eb7

- Grefenstette, B. W., Harrison, F. A., Boggs, S. E., et al. 2014, *Nature*, 506, 339, doi: 10.1038/nature12997
- Gu, W.-M., & Foglizzo, T. 2003, *A&A*, 409, 1, doi: 10.1051/0004-6361:20031080
- Gu, W.-M., & Lu, J.-F. 2006, *MNRAS*, 365, 647, doi: 10.1111/j.1365-2966.2005.09750.x
- Harikae, S., Kotake, K., Takiwaki, T., & Sekiguchi, Y.-i. 2010, *ApJ*, 720, 614, doi: 10.1088/0004-637X/720/1/614
- Harikae, S., Takiwaki, T., & Kotake, K. 2009, *ApJ*, 704, 354, doi: 10.1088/0004-637X/704/1/354
- Hayashi, K., Fujibayashi, S., Kiuchi, K., et al. 2022, *PhRvD*, 106, 023008, doi: 10.1103/PhysRevD.106.023008
- Hayashi, K., Kiuchi, K., Kyutoku, K., Sekiguchi, Y., & Shibata, M. 2023, *PhRvD*, 107, 123001, doi: 10.1103/PhysRevD.107.123001
- Hempel, M., Fischer, T., Schaffner-Bielich, J., & Liebendörfer, M. 2012, *ApJ*, 748, 70, doi: 10.1088/0004-637X/748/1/70
- Hotokezaka, K., Kiuchi, K., Shibata, M., Nakar, E., & Piran, T. 2018, *ApJ*, 867, 95, doi: 10.3847/1538-4357/aadf92
- Howard, W. M., Meyer, B. S., & Woosley, S. E. 1991, *ApJL*, 373, L5, doi: 10.1086/186038
- Hoyle, F. 1946, *MNRAS*, 106, 343, doi: 10.1093/mnras/106.5.343
- . 1954, *ApJS*, 1, 121, doi: 10.1086/190005
- Hoyle, F., & Fowler, W. A. 1960, *ApJ*, 132, 565, doi: 10.1086/146963

- Hunter, J. D. 2007, *Computing In Science & Engineering*, 9, 90, doi: 10.1109/MCSE.2007.55
- Ishimaru, Y., Wanajo, S., & Prantzos, N. 2015, *ApJL*, 804, L35, doi: 10.1088/2041-8205/804/2/L35
- Itoh, N., Hayashi, H., Nishikawa, A., & Kohyama, Y. 1996, *ApJS*, 102, 411
- Ivanov, M., & Fernández, R. 2021, preprint, arXiv:2101.02712. <https://arxiv.org/abs/2101.02712>
- Iwamoto, K., Mazzali, P. A., Nomoto, K., et al. 1998, *Nature*, 395, 672, doi: 10.1038/27155
- Janiuk, A. 2019, *ApJ*, 882, 163, doi: 10.3847/1538-4357/ab3349
- Janiuk, A., Shahamat Dehsorkh, N., & Król, D. L. 2023, *A&A*, 677, A19, doi: 10.1051/0004-6361/202245610
- Janka, H. T., & Bauswein, A. 2022, arXiv e-prints, arXiv:2212.07498, doi: 10.48550/arXiv.2212.07498
- Janka, H.-T., & Bauswein, A. 2023, *Dynamics and Equation of State Dependencies of Relevance for Nucleosynthesis in Supernovae and Neutron Star Mergers*, ed. I. Tanihata, H. Toki, & T. Kajino (Singapore: Springer Nature Singapore), 4005–4102, doi: 10.1007/978-981-19-6345-2_93
- Ji, A. P., Frebel, A., Chiti, A., & Simon, J. D. 2016, *Nature*, 531, 610, doi: 10.1038/nature17425
- Johnson, J. A. 2019, *Science*, 363, 474, doi: 10.1126/science.aau9540
- Just, O., Aloy, M. A., Obergaulinger, M., & Nagataki, S. 2022a, *ApJ*, 934, L30, doi: 10.3847/2041-8213/ac83a1

- Just, O., Goriely, S., Janka, H. T., Nagataki, S., & Bauswein, A. 2022b, *MNRAS*, 509, 1377, doi: 10.1093/mnras/stab2861
- Kittel, C., & Kroemer, H. 1980, *Thermal Physics*, 2nd edn. (New York: W.H. Freeman & Co.)
- Kiuchi, K., Fujibayashi, S., Hayashi, K., et al. 2023, *PhRvL*, 131, 011401, doi: 10.1103/PhysRevLett.131.011401
- Kobayashi, C., Mandel, I., Belczynski, K., et al. 2023, *ApJL*, 943, L12, doi: 10.3847/2041-8213/acad82
- Kohri, K., Narayan, R., & Piran, T. 2005, *ApJ*, 629, 341, doi: 10.1086/431354
- Kolb, E. W., & Turner, M. S. 1990, *The early universe*, Vol. 69
- Kotake, K., Iwakami, W., Ohnishi, N., & Yamada, S. 2009, *ApJL*, 697, L133, doi: 10.1088/0004-637X/697/2/L133
- Langanke, K., & Martínez-Pinedo, G. 2000, *Nuclear Physics A*, 673, 481, doi: 10.1016/S0375-9474(00)00131-7
- Lattimer, J. M., & Schramm, D. N. 1974, *ApJL*, 192, L145, doi: 10.1086/181612
- Lee, W. H., & Ramirez-Ruiz, E. 2006, *ApJ*, 641, 961, doi: 10.1086/500533
- Leung, S.-C., & Nomoto, K. 2023, arXiv e-prints, arXiv:2312.17226, doi: 10.48550/arXiv.2312.17226
- Lindner, C. C., Milosavljević, M., Couch, S. M., & Kumar, P. 2010, *ApJ*, 713, 800, doi: 10.1088/0004-637X/713/2/800
- Lippuner, J., Fernández, R., Roberts, L. F., et al. 2017a, *MNRAS*, 472, 904, doi: 10.1093/mnras/stx1987
- . 2017b, *MNRAS*, 472, 904, doi: 10.1093/mnras/stx1987

- Lippuner, J., & Roberts, L. F. 2015, *ApJ*, 815, 82, doi: 10.1088/0004-637X/815/2/82
- Lippuner, J., & Roberts, L. F. 2017, *The Astrophysical Journal Supplement Series*, 233, 18, doi: 10.3847/1538-4365/aa94cb
- Liu, Z.-W., Röpke, F. K., & Han, Z. 2023, *Research in Astronomy and Astrophysics*, 23, 082001, doi: 10.1088/1674-4527/acd89e
- Loken, C., Gruner, D., Groer, L., et al. 2010, *Journal of Physics: Conference Series*, 256, 012026, doi: 10.1088/1742-6596/256/1/012026
- Lopez-Camara, D., Lee, W. H., & Ramirez-Ruiz, E. 2009, *ApJ*, 692, 804, doi: 10.1088/0004-637X/692/1/804
- López-Cámara, D., Lee, W. H., & Ramirez-Ruiz, E. 2010, *ApJ*, 716, 1308, doi: 10.1088/0004-637X/716/2/1308
- Lund, T., Marek, A., Lunardini, C., Janka, H.-T., & Raffelt, G. 2010, *PhRvD*, 82, 063007, doi: 10.1103/PhysRevD.82.063007
- Lyman, J. D., Bersier, D., James, P. A., et al. 2016, *MNRAS*, 457, 328, doi: 10.1093/mnras/stv2983
- MacFadyen, A. I. 2003, in *From Twilight to Highlight: The Physics of Supernovae*, ed. W. Hillebrandt & B. Leibundgut, 97, doi: 10.1007/10828549_14
- MacFadyen, A. I., & Woosley, S. E. 1999, *ApJ*, 524, 262, doi: 10.1086/307790
- MacFadyen, A. I., Woosley, S. E., & Heger, A. 2001, *ApJ*, 550, 410, doi: 10.1086/319698
- Mamdouh, A., Pearson, J. M., Rayet, M., & Tondeur, F. 2001, *Nuclear Physics A*, 679, 337, doi: 10.1016/S0375-9474(00)00358-4
- Mathews, G. J., & Cowan, J. J. 1990, *Nature*, 345, 491, doi: 10.1038/345491a0

- McWilliam, A., Preston, G. W., Sneden, C., & Searle, L. 1995, *AJ*, 109, 2757, doi: 10.1086/117486
- Meija, J., Coplen, T. B., Berglund, M., et al. 2016, *Pure and Applied Chemistry*, 88, 293, doi: doi:10.1515/pac-2015-0503
- Merrill, P. W. 1952, *ApJ*, 116, 21, doi: 10.1086/145589
- Metzger, B. D., & Fernández, R. 2014, *MNRAS*, 441, 3444, doi: 10.1093/mnras/stu802
- Milisavljevic, D., & Margutti, R. 2018, *SSRv*, 214, 68, doi: 10.1007/s11214-018-0500-y
- Miller, J. M., Sprouse, T. M., Fryer, C. L., et al. 2020, *ApJ*, 902, 66, doi: 10.3847/1538-4357/abb4e3
- Mizuno, Y., Yamada, S., Koide, S., & Shibata, K. 2004a, *ApJ*, 606, 395, doi: 10.1086/382945
- . 2004b, *ApJ*, 615, 389, doi: 10.1086/423949
- Modjaz, M., Gutiérrez, C. P., & Arcavi, I. 2019, *Nature Astronomy*, 3, 717, doi: 10.1038/s41550-019-0856-2
- Modjaz, M., Liu, Y. Q., Bianco, F. B., & Graur, O. 2016, *ApJ*, 832, 108, doi: 10.3847/0004-637X/832/2/108
- Möller, P., Sierk, A. J., Ichikawa, T., & Sagawa, H. 2016, *Atomic Data and Nuclear Data Tables*, 109, 1, doi: 10.1016/j.adt.2015.10.002
- Molteni, D., Tóth, G., & Kuznetsov, O. A. 1999, *ApJ*, 516, 411, doi: 10.1086/307079
- Mösta, P., Roberts, L. F., Halevi, G., et al. 2018, *ApJ*, 864, 171, doi: 10.3847/1538-4357/aad6ec

- Müller, E., & Steinmetz, M. 1995, *Computer Physics Communications*, 89, 45, doi: 10.1016/0010-4655(94)00185-5
- Murphy, J. W., Ott, C. D., & Burrows, A. 2009, *ApJ*, 707, 1173, doi: 10.1088/0004-637X/707/2/1173
- Nadezhin, D. K. 1980, *Astrophysics & Space Science*, 69, 115, doi: 10.1007/BF00638971
- Nagakura, H., & Yamada, S. 2008, *ApJ*, 689, 391, doi: 10.1086/590325
- . 2009, *ApJ*, 696, 2026, doi: 10.1088/0004-637X/696/2/2026
- Nagataki, S. 2018, *Reports on Progress in Physics*, 81, 026901, doi: 10.1088/1361-6633/aa97a8
- Nagataki, S., Takahashi, R., Mizuta, A., & Takiwaki, T. 2007, *ApJ*, 659, 512, doi: 10.1086/512057
- Nakamura, K., Kajino, T., Mathews, G. J., Sato, S., & Harikae, S. 2013, *International Journal of Modern Physics E*, 22, 1330022, doi: 10.1142/S0218301313300221
- Narayan, R., & Yi, I. 1994, *ApJL*, 428, L13, doi: 10.1086/187381
- Nishimura, N., Takiwaki, T., & Thielemann, F.-K. 2015, *ApJ*, 810, 109, doi: 10.1088/0004-637X/810/2/109
- Nomoto, K. 2017, in *Handbook of Supernovae*, ed. A. W. Alsabti & P. Murdin (Springer, Cham), 1931, doi: 10.1007/978-3-319-21846-5_86
- Obergaulinger, M., & Aloy, M. Á. 2017, *MNRAS*, 469, L43, doi: 10.1093/mnrasl/slx046
- . 2022, *MNRAS*, 512, 2489, doi: 10.1093/mnras/stac613

- O'Connor, E., & Ott, C. D. 2010, *Classical and Quantum Gravity*, 27, 114103, doi: 10.1088/0264-9381/27/11/114103
- . 2011, *ApJ*, 730, 70, doi: 10.1088/0004-637X/730/2/70
- Oda, T., Hino, M., Muto, K., Takahara, M., & Sato, K. 1994, *Atomic Data and Nuclear Data Tables*, 56, 231, doi: 10.1006/adnd.1994.1007
- Ono, M., Hashimoto, M., Fujimoto, S., Kotake, K., & Yamada, S. 2009, *Progress of Theoretical Physics*, 122, 755, doi: 10.1143/PTP.122.755
- Ono, M., Hashimoto, M.-a., Fujimoto, S.-i., Kotake, K., & Yamada, S. 2012, *Progress of Theoretical Physics*, 128, 741, doi: 10.1143/PTP.128.741
- Ott, C. D., Reisswig, C., Schnetter, E., et al. 2011, *PRL*, 106, 161103, doi: 10.1103/PhysRevLett.106.161103
- Ouchi, R., Maeda, K., Anderson, J. P., & Sawada, R. 2021, *ApJ*, 922, 141, doi: 10.3847/1538-4357/ac2306
- Paczynski, B., & Wiita, P. J. 1980, *A&A*, 88, 23
- Panov, I. V., Korneev, I. Y., Rauscher, T., et al. 2010, *Astronomy & Astrophysics*, 513, A61, doi: 10.1051/0004-6361/200911967
- Peters, P. C., & Mathews, J. 1963, *Phys. Rev.*, 131, 435, doi: 10.1103/PhysRev.131.435
- Ponce, M., van Zon, R., Northrup, S., et al. 2019, in *Proceedings of the Practice and Experience in Advanced Research Computing on Rise of the Machines (Learning)*, PEARC '19 (New York, NY, USA: Association for Computing Machinery), doi: 10.1145/3332186.3332195
- Popham, R., Woosley, S. E., & Fryer, C. 1999, *ApJ*, 518, 356

- Prantzos, N. 2004, in ESA Special Publication, Vol. 552, 5th INTEGRAL Workshop on the INTEGRAL Universe, ed. V. Schoenfelder, G. Lichti, & C. Winkler, 15, doi: 10.48550/arXiv.astro-ph/0404501
- Proga, D., MacFadyen, A. I., Armitage, P. J., & Begelman, M. C. 2003, ApJ, 599, L5, doi: 10.1086/381158
- Pruet, J., Woosley, S. E., & Hoffman, R. D. 2003, ApJ, 586, 1254, doi: 10.1086/367957
- Rastinejad, J. C., Gompertz, B. P., Levan, A. J., et al. 2022, Nature, 612, 223, doi: 10.1038/s41586-022-05390-w
- Rastinejad, J. C., Fong, W., Levan, A. J., et al. 2023, arXiv e-prints, arXiv:2312.04630, doi: 10.48550/arXiv.2312.04630
- Reichert, M., Bugli, M., Guilet, J., et al. 2024, MNRAS, 529, 3197, doi: 10.1093/mnras/stae561
- Rosswog, S., Sollerman, J., Feindt, U., et al. 2018, A&A, 615, A132, doi: 10.1051/0004-6361/201732117
- Ruffert, M., Janka, H.-T., & Schaefer, G. 1996, A&A, 311, 532
- Russell, H. N. 1929, ApJ, 70, 11, doi: 10.1086/143197
- Schatz, H., Aprahamian, A., Brown, B., et al. 1997, Nuclear Physics A, 621, 417, doi: [https://doi.org/10.1016/S0375-9474\(97\)00283-2](https://doi.org/10.1016/S0375-9474(97)00283-2)
- Scott, P., Asplund, M., Grevesse, N., Bergemann, M., & Sauval, A. J. 2015a, A&A, 573, A26, doi: 10.1051/0004-6361/201424110
- Scott, P., Grevesse, N., Asplund, M., et al. 2015b, A&A, 573, A25, doi: 10.1051/0004-6361/201424109

- Seitenzahl, I. R., Timmes, F. X., Marin-Lafèche, A., et al. 2008, *ApJL*, 685, L129, doi: 10.1086/592501
- Sekiguchi, Y., Kiuchi, K., Kyutoku, K., & Shibata, M. 2011, *PRL*, 107, 051102, doi: 10.1103/PhysRevLett.107.051102
- Sekiguchi, Y., & Shibata, M. 2007, *Progress of Theoretical Physics*, 117, 1029, doi: 10.1143/PTP.117.1029
- Shakura, N. I., & Sunyaev, R. A. 1973, *A&A*, 24, 337
- Shibata, M., Fujibayashi, S., Tsz-Lok Lam, A., Ioka, K., & Sekiguchi, Y. 2023, arXiv e-prints, arXiv:2309.12086, doi: 10.48550/arXiv.2309.12086
- Siegel, D. M., Barnes, J., & Metzger, B. D. 2019, *Nature*, 569, 241, doi: 10.1038/s41586-019-1136-0
- Siegel, D. M., & Metzger, B. D. 2018, *ApJ*, 858, 52, doi: 10.3847/1538-4357/aabaec
- Sieverding, A., Kresse, D., & Janka, H.-T. 2023, *ApJL*, 957, L25, doi: 10.3847/2041-8213/ad045b
- Spergel, D. N., Verde, L., Peiris, H. V., et al. 2003, *ApJS*, 148, 175, doi: 10.1086/377226
- Steiner, A. W., Hempel, M., & Fischer, T. 2013, *ApJ*, 774, 17, doi: 10.1088/0004-637X/774/1/17
- Stone, J. M., Pringle, J. E., & Begelman, M. C. 1999, *MNRAS*, 310, 1002
- Strang, G. 1968, *SIAM Journal on Numerical Analysis*, 5, 506, doi: 10.1137/0705041
- Suess, H. E., & Urey, H. C. 1956, *Reviews of Modern Physics*, 28, 53, doi: 10.1103/RevModPhys.28.53

- Surman, R., McLaughlin, G. C., & Hix, W. R. 2006, *ApJ*, 643, 1057, doi: 10.1086/501116
- Surman, R., McLaughlin, G. C., & Sabbatino, N. 2011, *ApJ*, 743, 155, doi: 10.1088/0004-637X/743/2/155
- Takahashi, K., El Eid, M. F., & Hillebrandt, W. 1978, *A&A*, 67, 185
- Tamborra, I., Hanke, F., Müller, B., Janka, H.-T., & Raffelt, G. 2013, *PhRvL*, 111, 121104, doi: 10.1103/PhysRevLett.111.121104
- The LIGO Scientific Collaboration, the Virgo Collaboration, the KAGRA Collaboration, et al. 2021a, arXiv e-prints, arXiv:2111.03606. <https://arxiv.org/abs/2111.03606>
- The LIGO Scientific Collaboration, the Virgo Collaboration, et al. 2021b, arXiv e-prints, arXiv:2108.01045. <https://arxiv.org/abs/2108.01045>
- Thielemann, F.-K., Isern, J., Perego, A., & von Ballmoos, P. 2018, *SSRv*, 214, 62, doi: 10.1007/s11214-018-0494-5
- Timmes, F. X. 1999, *ApJS*, 124, 241, doi: 10.1086/313257
- Timmes, F. X., Hoffman, R. D., & Woosley, S. E. 2000, *ApJS*, 129, 377, doi: 10.1086/313407
- Timmes, F. X., & Swesty, F. D. 2000, *ApJS*, 126, 501, doi: 10.1086/313304
- Tinsley, B. M. 1980, *FCPh*, 5, 287, doi: 10.48550/arXiv.2203.02041
- Tsuruta, S., & Cameron, A. G. W. 1965, *Canadian Journal of Physics*, 43, 2056, doi: 10.1139/p65-199
- Villar, V. A., Guillochon, J., Berger, E., et al. 2017, *ApJL*, 851, L21, doi: 10.3847/2041-8213/aa9c84

- Wahl, A. C. 2002, Technical Report LA-13928. Systematics of fission-product yields (Los Alamos, NM: Los Alamos National Laboratory)
- Wallace, R. K., & Woosley, S. E. 1981, *ApJS*, 45, 389, doi: 10.1086/190717
- Wanajo, S., Müller, B., Janka, H.-T., & Heger, A. 2018, *ApJ*, 852, 40, doi: 10.3847/1538-4357/aa9d97
- Wang, T., & Burrows, A. 2023, *ApJ*, 954, 114, doi: 10.3847/1538-4357/ace7b2
- . 2024, arXiv e-prints, arXiv:2406.13746, doi: 10.48550/arXiv.2406.13746
- Weaver, T. A., Zimmerman, G. B., & Woosley, S. E. 1978, *ApJ*, 225, 1021, doi: 10.1086/156569
- Weisberg, J. M., & Huang, Y. 2016, *ApJ*, 829, 55, doi: 10.3847/0004-637X/829/1/55
- Wilson, J. R. 1985, in *Numerical Astrophysics*, 422
- Witt, M., Psaltis, A., Yasin, H., et al. 2021, *ApJ*, 921, 19, doi: 10.3847/1538-4357/ac1a6d
- Woosley, S. E. 1993, *ApJ*, 405, 273, doi: 10.1086/172359
- Woosley, S. E., Eastman, R. G., & Schmidt, B. P. 1999, *ApJ*, 516, 788, doi: 10.1086/307131
- Woosley, S. E., & Heger, A. 2006, *ApJ*, 637, 914, doi: 10.1086/498500
- Woosley, S. E., Heger, A., & Weaver, T. A. 2002, *Rev. Mod. Phys.*, 74, 1015, doi: 10.1103/RevModPhys.74.1015
- Woosley, S. E., & Howard, W. M. 1978, *ApJS*, 36, 285, doi: 10.1086/190501
- Zenati, Y., Siegel, D. M., Metzger, B. D., & Perets, H. B. 2020, *MNRAS*, 499, 4097, doi: 10.1093/mnras/staa3002

Zevin, M., Kremer, K., Siegel, D. M., et al. 2019, ApJ, 886, 4, doi: 10.3847/1538-4357/ab498b

Zha, S., Müller, B., & Powell, J. 2024, ApJ, 969, 141, doi: 10.3847/1538-4357/ad4ae7

Zhu, Y., Wollaeger, R. T., Vassh, N., et al. 2018, ApJL, 863, L23, doi: 10.3847/2041-8213/aad5de